ISSN: 2376-2136 (Print)
ISSN: 2376-2144 (Online)

Trends in Renewable Energy

Volume 3, Issue 2, December 2017

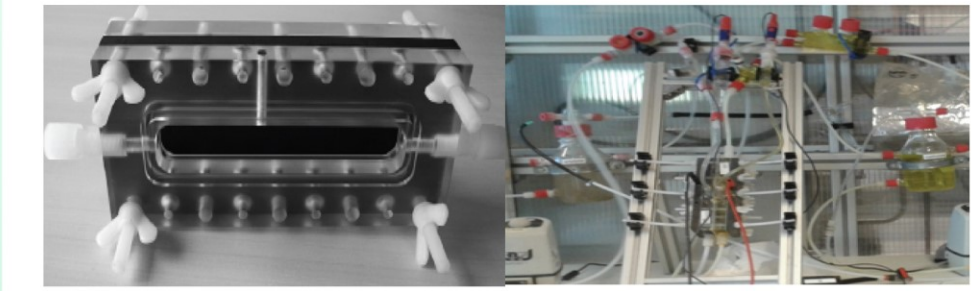

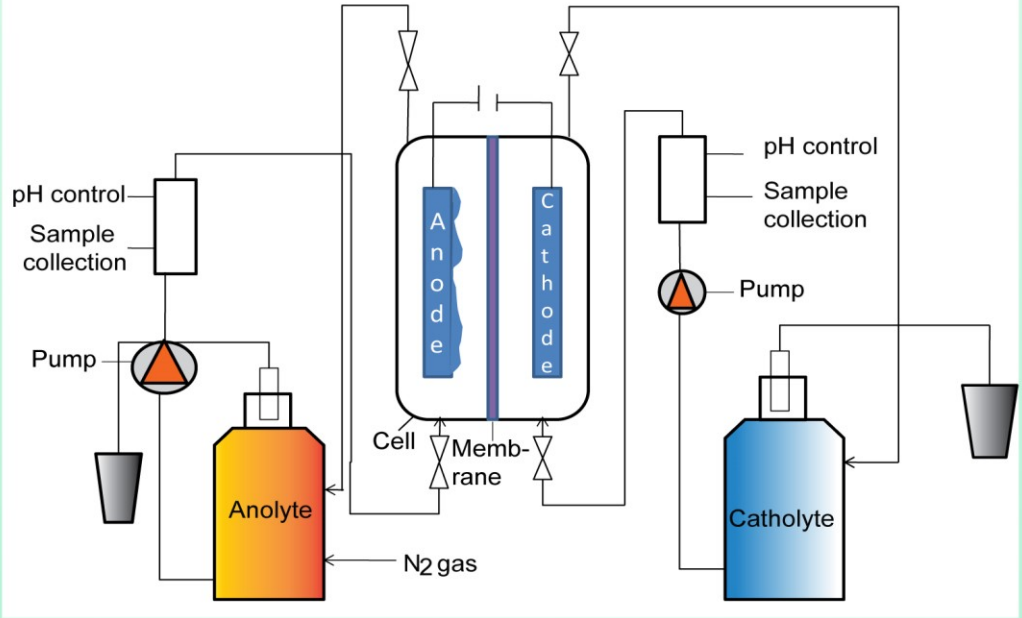

Cover image: a microbial fuel cell design, see article by Pramanik and Rana in this issue.

ISSN 2376-2136 08
9 772376 213001

futureenergysp.com
thefutureenergy.org

Trends in Renewable Energy

ISSN: 2376-2136 (Print) ISSN: 2376-2144 (Online)

http://futureenergysp.com/

Trends in Renewable Energy is an open accessed, peer-reviewed semi-annual journal publishing reviews and research papers in the field of renewable energy technology and science.

The aim of this journal is to provide a communication platform that is run exclusively by scientists working in the renewable energy field. Scope of the journal covers: Bioenergy, Biofuel, Biomass, Bioprocessing, Biorefinery, Biological waste treatment, Catalysis for energy generation, Energy conservation, Energy delivery, Energy resources, Energy storage, Energy transformation, Environmental impact, Feedstock utilization, Future energy development, Green chemistry, Green energy, Microbial products, Physico-chemical process for Biomass, Policy, Pollution, Renewable energy, Smart grid, Thermo-chemical processes for biomass, etc.

The Trends in Renewable Energy publishes the following article types: peer-reviewed reviews, mini-reviews, technical notes, short-form research papers, and original research papers.

The article processing charge (APC), also known as a publication fee, is fully waived for the Trends in Renewable Energy.

Editorial Team of Trends in Renewable Energy

EDITORIAL BOARD

Table of Contents

Volume 3, Issue No. 2, December 2017

Articles

Reviews

Trends in Renewable Energy
OPEN ACCESS ISSN:2376-2144
Peer-Reviewed Article futureenergysp.com/index.php/tre

Improvement of Power Systems Stability by Applying Topology Identification Methodology (TIM) and Fault and Instability Identification Methodology (FIIM) – Study of the Overhead Medium-Voltage Broadband over Power Lines (OV MV BPL) Networks Case

Athanasios G. Lazaropoulos[1]

1: School of Electrical and Computer Engineering / National Technical University of Athens / 9 IroonPolytechniou Street / Zografou, GR 15780

Received January 30, 2017; Accepted March 28, 2017; Published April 27, 2017

The performance of two useful piecewise monotonic data approximation (PMA) applications that are Topology Identification Methodology (TIM) and Fault and Instability Identification Methodology (FIIM) is investigated in this paper for the overhead medium-voltage broadband over power lines (OV MV BPL) networks. TIM and FIIM are applied to OV MV BPL networks when measurement differences, faults and instabilities occur. By exploiting the L1PMA optimal number of monotonic sections, advanced TIM and FIIM are also proposed and applied to OV MV BPL networks. The results of the four PMA applications are compared and it is found that advanced TIM and FIIM achieve higher computational speeds and almost equivalent identification performance in comparison with the respective original TIM and FIIM. Exploiting the better performance metrics of advanced TIM and FIIM, PMA applications provide a stable step towards the real time surveillance and monitoring of transmission and distribution power grid.

Keywords: Smart Grid; Intelligent Energy Systems; Broadband over Power Lines (BPL) Networks; Power Line Communications (PLC); Faults; Fault Analysis; Fault Identification and Prediction; Distribution Power Grids

1. Introduction

The power stability of transmission and distribution power grids relies on the increasing aging electrical grid systems worldwide, some of which originated from the earlies of 20th century. Nowadays, the power stability can be enhanced through the deployment of the broadband over powerlines (BPL) networks across this vintage power grid infrastructure. In fact, BPL technology can transform the traditional transmission and power grids into an integrated intelligent IP-based communications network with a myriad of smart grid applications [1]-[4].

In order to be able to deliver high-bandwidth applications (*e.g.*, HD video streaming and VoIP) with data rates that exceed 1Gbps, various inherent deficiencies of the BPL networks, such as the high and frequency-selective channel attenuation and noise, should be overcome now so that BPL networks can become both a

*Corresponding author: AGLazaropoulos@gmail.com

Tr Ren Energy, 2017, Vol.3, No.2, 102-128. doi:10.17737/tre.2017.3.2.0034

useful power grid complement and a strong telecommunications competitor to the other wireless networking solution [5]-[13].

As the determination of the transfer functions of overhead medium-voltage (OV MV) BPL networks is concerned in this paper, the well-established hybrid method, which is employed to examine the behavior of various multiconductor transmission line (MTL) structures, is also adopted in this paper [5]-[9], [14]-[25]. Given as the inputs the OV MV BPL network topology, OV MV MTL configuration and the applied coupling scheme, the hybrid method gives as the output the corresponding transfer function.

Because of a number of practical reasons and "real-life" conditions, measurement differences between the experimental and theoretical results occur during the transfer function determination of OV MV BPL network topologies [2], [24]-[27]. To mitigate the aforementioned measurement differences and restore the theoretical BPL transfer function, piecewise monotonic data approximations (PMAs) have been successfully applied either in transmission or in distribution BPL networks [2], [24]-[27]. Among the available PMAs, L1PMA with optimal number of monotonic sections, which has been thoroughly analyzed and assessed in [2], [27], is proven to best approximate the theoretical OV MV BPL transfer functions regardless of the examined OV MV BPL network topology and the applied coupling scheme even if measurement differences ranging from 1 to 10dB are imposed.

On the basis of the aforementioned PMA benchmark results, two of the most useful PMA applications that are Topology Identification Methodology (TIM) of [24] and Fault and Instability Identification Methodology (FIIM) of [25] can be further upgraded. At first sight, TIM achieves to reveal the exact topological characteristics (*i.e.*, number of branches, length of branches, length of main lines and branch terminations) of a BPL topology by appropriately approximating the measured transfer function data, which are contaminated by measurement differences. TIM is based on the application of L1PMA. Through a similar L1PMA approximation of the measured transfer function data, FIIM achieves to identify faults and instabilities that occur in BPL topologies and can affect the power system stability. Although the performance of TIM and FIIM has been investigated in transmission BPL networks, these two PMA applications are first applied in distribution BPL networks, say OV MV BPL networks. Exploiting the optimal number of monotonic sections of [27], which offers better performance concerning the approximation efficiency of L1PMA, both TIM and FIIM can become more accurate and faster.

The rest of this paper is organized as follows: In Sec. II, the OV MV MTL configuration, the indicative OV MV BPL topologies and the basics of BPL signal transmission are presented. In Sec. III, a brief presentation of the L1PMA, TIM and FIIM is given as well as suitable performance metrics. Sec. IV discusses the simulations of various OV MV BPL networks intending to mark out the efficiency of TIM and FIIM in these networks as well as their performance upgrade due to the optimal number of monotonic sections. Sec. V concludes this paper.

2. Configurations, Topologies and BPL Signal Transmission

2.1 OV MV MTL Configuration

The OV MV MTL configuration, which is examined in this paper, is presented in Fig. 1(a) of [2]. This MTL configuration comprises three phase lines of radius $r_{\mathrm{MV,p}}$ that are spaced by Δ_{MV} and hung at typical heights h_{MV} above ground. The ground with conductivity σ_{g} and relative permittivity $\varepsilon_{\mathrm{rg}}$ is considered as the reference conductor. The exact values concerning the related conductor dimensions, ground properties and configuration geometry are reported in [5], [6], [17], [19], [21], [28]-[30]. The applied exact values define a realistic scenario during the following analysis while the impact of imperfect ground on broadband signal propagation via OV MV power lines was analyzed in [5], [6], [17], [19], [21], [31]-[33].

2.2 Indicative OV MV BPL Topologies

In accordance with [26] and with reference to Fig. 1(a), average path lengths of the order of 1000m are considered in OV MV BPL topologies. Four indicative OV MV BPL topologies, concerning end-to-end connections of average path lengths, are examined, namely:

1. A typical urban topology (OV MV urban case) with N=3 branches (L_1=500m, L_2=200m, L_3=100m, L_4=200m, L_{b1}=8m, L_{b2}=13m, L_{b3}=10m).
2. A typical suburban topology (OV MV suburban case) with N=2 branches (L_1=500m, L_2=400m, L_3=100m, L_{b1}=50m, L_{b2}=10m).
3. A typical rural topology (OV MV rural case) with only N=1 branch (L_1=600m, L_2=400m, L_{b1}=300m).
4. The "LOS" transmission along the same end-to-end distance $L=L_1+\ldots+L_{N+1}$=1000m when no branches are encountered. This topology corresponds to Line of Sight transmission in wireless channels.

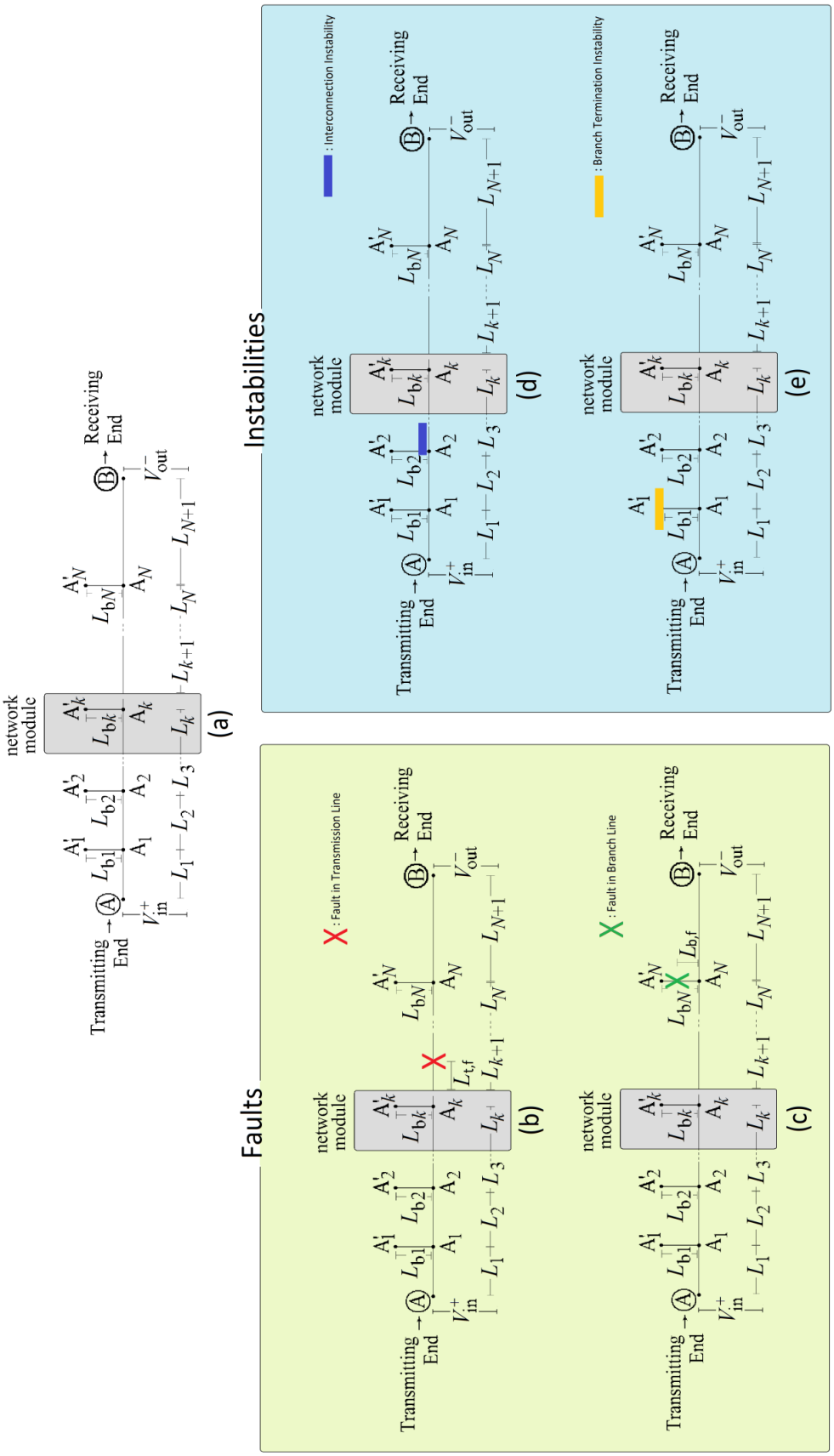

Figure 1. (a) General OV MV BPL topology [24]. (b, c) Faults in OV MV BPL topologies. (d, e) Instabilities in OV MV BPL topologies [25].

2.3 Hybrid Method, Coupling Schemes and Coupling Transfer Functions

Successfully tested in various transmission and distribution BPL networks [5]-[9], [14]-[23], [32]-[34], the well-established hybrid method consists of: (i) a bottom-up approach that is based on the MTL theory, eigenvalue decomposition (EVD) and singular value decomposition (SVD); and (ii) a top-down approach that is denoted as TM2 method and is based on the concatenation of multidimensional chain scattering matrices. Macroscopically, hybrid method gives as output the corresponding EVD modal and original transfer functions when the OV MV BPL network topology, OV MV MTL configuration and the applied coupling scheme are given as inputs.

Also, hybrid method may take as an input the way that the signals are injected into OV MV lines. In fact, two categories of coupling schemes are mainly supported by the OV MV BPL networks, namely [2], [16], [18], [24], [25], [35]-[37]: (i) Wire-to-Ground (WtG) coupling schemes; and (ii) Wire-to-Wire (WtW) coupling schemes. In the case of WtG coupling schemes, which is examined in this paper, the coupling WtG channel transfer function $H^{\mathrm{WtG^s}}\{\cdot\}$ is given from

$$H^{\mathrm{WtG^s}}\{\cdot\} = \left[\mathbf{C}^{\mathrm{WtG}}\right]^{\mathrm{T}} \cdot \mathbf{T}_V \cdot \mathbf{H}^{m}\{\cdot\} \cdot \mathbf{T}_V^{-1} \cdot \mathbf{C}^{\mathrm{WtG}} \quad (1)$$

where $\mathbf{C}^{\mathrm{WtG}}$ is an 3×1 coupling column vector with zero elements except in row *s* where the value is equal to 1, $\mathbf{T}_V$ is a $n^{\mathrm{OVMV}} \times n^{\mathrm{OVMV}}$ matrix that depends on the frequency, the OV MV MTL configuration and the physical properties of the cables and $\mathbf{H}^{\mathrm{m}}\{\cdot\}$ is the $n^{\mathrm{OVMV}} \times n^{\mathrm{OVMV}}$ EVD modal transfer function matrix that is given as an output by the hybrid method [5]-[9], [14]-[18], [21], [28], [38].

To give the coupling WtG channel transfer function of eq. (1), certain assumptions for the circuital parameters of OV MV BPL topologies need to be taken into account. In accordance with [2], these assumptions are: (i) The branch lines are assumed identical to the transmission ones; (ii) The interconnections between the transmission and branch conductors of the lines are fully activated; (iii) The transmitting and the receiving ends are assumed matched to the characteristic impedance of the modal channels; and (iv) The branch terminations are assumed open circuits.

3. L1PMA, TIM, FIIM and Performance Metrics

3.1 L1PMA

Various PMA methods have been proposed by Demetriou, such as L1PMA, L2WPMA and L2CXCV, that have been applied in transmission and distribution BPL networks so that the measurement differences can be mitigated and the theoretical OV MV BPL coupling transfer functions can be revealed [2], [24]-[27], [39]-[44]. Based on the comparative benchmark of the aforementioned PMA methods [26], [27], L1PMA has presented the higher and more stable overall mitigation performance against measurement differences and, for that reason, only L1PMA is applied in this paper.

In fact, L1PMA exploits the piecewise monotonicity property that always occurs in OV MV BPL coupling transfer functions. Analytically, L1PMA decomposes the coupling transfer functions into separate monotonous sections among their adjacent turning points (primary extrema) [41], [42]. Since the separate monotonous sections are identified, L1PMA separately handles them. As already been determined, the number of

monotonic sections can be equal either to the optimal number of monotonic sections, detailed in [2], [26], or to the adaptive number of monotonic sections, reported in [27]. According to [27], the adaptive number of monotonic sections helps towards the enhancement of the L1PMA mitigation performance against measurement differences; the concept of the adaptive number of monotonic sections is based on the need for more general approximations as the maximum differences increase and the examined OV MV BPL topologies increase in topological complexity.

On the basis of L1PMA and the adaptive number of monotonic sections, two of the most useful PMA applications that are TIM of [24] and FIIM of [25] can be further refined. Note that TIM and FIIM have been developed on the basis of L1PMA software, which receives as inputs the measured OV MV BPL coupling transfer function, the measurement frequencies and the number of monotonic sections and gives as output the best fit of the measured OV MV BPL coupling transfer function.

3.2 TIM, Advanced TIM and Curve Similarity Performance Metric (CSPM)

TIM is a PMA application that achieves to identify the real OV MV BPL topology by approximating and comparing the corresponding measured OV MV BPL coupling transfer function with a database of theoretical OV MV BPL coupling transfer functions. TIM consists of: (i) the hybrid method; (ii) L1PMA software; (iii) the OV MV BPL topology database; and (iv) CSPM that serves as the assessment metric of the TIM accuracy [24]. In accordance with [24], TIM CSPM achieves to reveal a set of candidate OV MV BPL topologies with the real topology lying inside it even though measurement differences of various distributions and magnitudes can occur.

More analytically, L1PMA gives the approximated OV MV coupling transfer function column vector $\overline{\overline{\mathbf{H}}}_{\text{meas}}^{\text{WtG}}(\mathbf{f},k_{\text{sect}})$ when measured OV MV one $\overline{\mathbf{H}}^{\text{WtG}}(\mathbf{f})$ and a number of monotonic sections k_{sect} are considered where $\mathbf{f}=\begin{bmatrix}f_1 & \cdots & f_i & \cdots & f_u\end{bmatrix}^{\text{T}}$ is the $u\times 1$ measurement frequency column vector. CSPM acts as the performance metric of the curve similarity between the measurement L1PMA approximation $\overline{\overline{\mathbf{H}}}_{\text{meas}}^{\text{WtG}}(\mathbf{f},k_{\text{sect}})$ and theory L1PMA approximation $\overline{\overline{\mathbf{H}}}_{\text{theor}}^{\text{WtG}}(\mathbf{f},k_{\text{sect}})$ and is determined by

$$CSPM_{k_{\text{sec}t}}\equiv CSPM_{k_{\text{sec}t}}\left(\overline{\mathbf{H}}^{\text{WtG}},k_{\text{sect}}\right)=\sum_{i=1}^{u}\left|\overline{\overline{\mathbf{H}}}_{\text{meas}}^{\text{WtG}}(f_i,k_{\text{sect}})-\overline{\overline{\mathbf{H}}}_{\text{theor}}^{\text{WtG}}(f_i,k_{\text{sect}})\right| \quad (2)$$

TIM is based on the CSPM and the OV MV BPL topology database in order to identify the OV MV BPL topology when a set of coupling transfer function measurements is available. TIM comprises three steps so that the OV MV BPL topology is revealed, say:

1. Given the measured OV MV BPL coupling transfer function column vector $\overline{\mathbf{H}}^{\text{WtG}}(\mathbf{f})$, the approximated OV MV BPL coupling transfer function column vector $\overline{\overline{\mathbf{H}}}_{\text{meas}}^{\text{WtG}}(\mathbf{f},k_{\text{sect}})$ is evaluated for monotonic sections that range from $k_{\text{sect,min}}$ to $k_{\text{sect,max}}$ where $k_{\text{sect,min}}$ and $k_{\text{sect,max}}$ is the minimum and maximum number of monotonic sections considered, respectively.

2. For each OV MV BPL topology and each monotonic section of the OV MV BPL topology database, the respective $CSPM_{k\text{sect}}$ of eq. (2) and the total $CSPM_{\text{tot}}$ are computed where

$$CSPM_{\text{tot}} \equiv \sum_{k_{\text{sect}}=k_{\text{sect,min}}}^{k_{\text{sect,max}}} CSPM_{k_{\text{sect}}} \tag{3}$$

3. TIM identifies OV MV BPL topologies with the lowest $CSPM_{\text{tot}}$ among all the available topologies of the database. These OV MV BPL topologies are members of the set of candidate OV MV BPL topologies. The number of candidate OV MV BPL topologies depends on the topological characteristics of the real topology (i.e., number of branches, branch length), the nature of measurement differences (i.e., measurement difference distributions, characteristics of distributions) and the number of monotonic sections.

In accordance with [24], TIM has been applied assuming that $k_{\text{sect,min}}$ and $k_{\text{sect,max}}$ are equal to 1 and 20, respectively, considering all the available L1PMA approximation cases. However, this assumption demands extremely high computational time, thus posing critical restrictions to the creation of the OV MV BPL topology database.

Taking into account the findings of [26], the adaptive number of monotonic sections can significantly reduce TIM computational load. Instead of considering the entire range of monotonic sections that ranges from 1 to 20, TIM analysis can only focus on a closed set of monotonic sections assuming that its set center $k_{\text{sect,AN}}$ is equal to the adaptive number of monotonic sections. Here, it should be noted that the adaptive number of monotonic section is unique given the examined OV MV BPL topology and an estimate of the magnitude of the occurred measurement differences. Numerically, $k_{\text{sect,min}}$ and $k_{\text{sect,max}}$ are assumed to be equal to

$$k_{\text{sect,min}} = \max\{1, k_{\text{sect,AN}} - 1\} \tag{4}$$

$$k_{\text{sect,max}} = \min\{20, k_{\text{sect,AN}} + 1\} \tag{5}$$

where $\max\{\cdot\}$ and $\min\{\cdot\}$ give the maximum and the minimum value among the examined values, respectively. Observing the bounds of the closed set of monotonic sections, this set consists of three or two values depending on the value of the set center $k_{\text{sect,AN}}$.

In average terms, the advanced TIM, which is based on eqs. (4) and (5), can achieve: (i) better accuracy performance during the identification of the real OV MV BPL topology since it considers only $CSPM_{k_{\text{sect}}}$ that can better approximate theoretical OV MV BPL coupling transfer functions; and (ii) reduction of the computational load that ranges from $100\% \cdot \frac{20-3}{20} = 85\%$ to $100\% \cdot \frac{20-2}{20} = 90\%$. The main disadvantage of the advanced TIM is that needs an estimate of the measurement difference condition in order to apply the suitable adaptive number of monotonic sections for given OV MV BPL topology.

3.3 FIIM, Advanced FIIM and Curve Similarity Performance percentage Metric (ΔCSPpM)

Apart from the aforementioned measurement differences during the determination of OV MV BPL coupling transfer functions, various serious problematic conditions can occur across the transmission and distribution power grids. FIIM identifies these problematic conditions that cause permanent damage to the power grid and their impact on the determination of OV MV BPL transfer functions totally change the form of the result.

In accordance with [25], FIIM repertory of faults and instabilities is presented in Figs. 1(b)-(e). In fact, the problematic conditions are divided into two categories with two subcategories each, namely:

- *Faults*: This category describes all the interruptions that can occur in the lines of a transmission power grid. There are two subcategories of line interruptions that are examined in this paper: (i) *Fault in transmission line* –see Fig. 1(b)–; and (ii) *Fault in branch line* –see Fig. 1(c)–.
- *Instabilities*: This category describes all the failures that can occur in the equipment across the transmission power grid. There are two subcategories of equipment failures that are examined in this paper: (i) *Instability in branch interconnections* –see Fig. 1(d)–; and (ii) *Instability in branch terminations* –see Fig. 1(e)–.

In total, FIIM can recognize either the fault or the instability condition and warn the responsible personnel.

As the implementation details of FIIM and its corresponding performance metrics are concerned, the proposed curve similarity performance percentage metric (ΔCSPpM), which acts as the accompanying performance metric of FIIM, is given by

$$\Delta CSPpM^{*} = CSPpM \ - CSPpM^{*} \tag{6}$$

where

$$CSPpM = 100\% \cdot \frac{\sum_{k_{\text{sect}}=k_{\text{sect,min}}}^{k_{\text{sect,max}}} \sum_{i=1}^{u} \frac{\left| \overline{\overline{\mathbf{H}_{\text{meas}}^{\text{WtG}}}}\left(f_i, k_{\text{sect}}\right) - \overline{\overline{\mathbf{H}_{\text{theor}}^{\text{WtG}}}}\left(f_i, k_{\text{sect}}\right) \right|}{\left| \overline{\overline{\mathbf{H}_{\text{theor}}^{\text{WtG}}}}\left(f_i, k_{\text{sect}}\right) \right|}}{\left(k_{\text{sect,max}} - k_{\text{sect,min}} + 1\right) \times u} \tag{7}$$

is retrieved during the normal operation of the OV MV BPL topology examined,

$$CSPpM^{*} = 100\% \cdot \frac{\sum_{k_{\text{sect}}=k_{\text{sect,min}}}^{k_{\text{sect,max}}} \sum_{i=1}^{u} \frac{\left| \overline{\overline{\mathbf{H}_{\text{meas}}^{\text{WtG*}}}}\left(f_i, k_{\text{sect}}\right) - \overline{\overline{\mathbf{H}_{\text{theor}}^{\text{WtG}}}}\left(f_i, k_{\text{sect}}\right) \right|}{\left| \overline{\overline{\mathbf{H}_{\text{theor}}^{\text{WtG}}}}\left(f_i, k_{\text{sect}}\right) \right|}}{\left(k_{\text{sect,max}} - k_{\text{sect,min}} + 1\right) \times u} \tag{8}$$

is retrieved during the problematic operation of the OV MV BPL topology when either fault or instability occurs and $\overline{\overline{\mathbf{H}_{\text{meas}}^{\text{WtG*}}}}\left(\mathbf{f}, k_{\text{sect}}\right)$ is the approximated measured OV MV BPL coupling transfer function column vector of the modified topology that comes from the application of L1PMA for different monotonic sections.

FIIM compares $\Delta CSPpM^*$ with a warning threshold $\Delta CSPpM_{\text{thr}}^*$ that is typically equal to zero. Details concerning the determination of the warning threshold $\Delta CSPpM_{\text{thr}}^*$ and the relative decisions are provided in [25].

Similarly to TIM, the adaptive number of monotonic sections can significantly enhance FIIM performance by taking into account the findings of [26]. Instead of considering the entire range of monotonic sections that ranges from 1 to 20, FIIM analysis can only focus on the closed set of monotonic sections defined in TIM case. By assuming set lower and upper bounds equal to $k_{\text{sect,min}}$ and $k_{\text{sect,max}}$, respectively. This advanced FIIM can achieve: (i) better accuracy performance during the identification of faults and instabilities since it considers only $CSPpM$ that can better approximate theoretical OV MV BPL coupling transfer functions; and (ii) reduction of the computational load that again ranges from 85% to 90%. The main disadvantage of the advanced FIIM is that needs an overall knowledge of the measurement difference environment in order to apply the suitable adaptive number of monotonic sections for given OV MV BPL topology.

4. Numerical Results and Discussion

4.1 Simulation Goals and Parameters

Various types of OV MV BPL topologies are simulated with the purpose of evaluating the proposed advanced TIM and FIIM against the original ones. In accordance with [24] and [25], the performance efficiency and the processing time of the advanced TIM and FIIM are assessed with regards to the indicative OV MV BPL topologies and the nature of the occurred measurement differences. Actually, measurement differences that occur in OV MV BPL networks are typically described by CUD with maximum CUD value that is equal to α_{CUD}.

As regards the hybrid method and L1PMA with adaptive number specifications, those are the same with [24]. More specifically, the BPL frequency range and the flat-fading subchannel frequency spacing are assumed equal to 1-30MHz and 1MHz, respectively. Therefore, the number of subchannels u in the examined frequency range is equal to 30. Arbitrarily, the WtG[1] coupling scheme is applied during the following simulations. Finally, the maximum number of monotonic sections $k_{\text{sect,max}}$ that is going to be used is assumed to be equal to 20 [2].

As the OV MV BPL topology database specifications are concerned, the maximum number of branches N, the length spacing L_{s} for both branch distance and branch length and the maximum branch length L_{b} are assumed equal to 2, 50m and 300m, respectively.

4.2 L1PMA with Adaptive Number of Monotonic Sections

The advanced TIM and FIIM are both based on the concept of the adaptive number of monotonic sections, which has been presented in [27]. To compute the adaptive number of monotonic sections, an estimation of the maximum CUD value, which occurs during the operation of OV MV BPL network, is required. In fact, the adaptive number of monotonic sections comes from the monotonic section

localization of the best measurement difference mitigation performance given the maximum CUD value, the examined OV MV BPL topology and the applied WtG coupling scheme. Already been reported in [27], the adaptive number of monotonic sections for the indicative OV MV BPL topologies of Sec.2.2 is presented in Table 1 when WtG[1] coupling scheme is applied and maximum CUD value range from 0 to 10dB. Also, the lower and upper bounds of the monotonic section set, which are reported in eqs. (4) and (5) and are going to be used in advanced TIM and FIIM of the following subsections, are presented in each of the cases examined.

From Table 1, it is evident that the adaptive number of monotonic sections decreases as the maximum CUD value increases for given OV MV BPL topology. This is a reasonable result since there is need for more general approximations as the measurement differences create significant differences between theoretical and measured OV MV BPL coupling transfer functions. Towards that direction, the lower and upper bounds of monotonic section sets follow this trend. Anyway, the narrow monotonic section sets allow to avoid large values of $CSPM_{ksect}$ that little contribute to the overall CSPM and CSPpM performance of TIM and FIIM, respectively.

Since OV MV BPL coupling transfer functions present close behavior for given number of branches [19], [20], [33], [38], the adaptive number of monotonic sections of urban, suburban, rural and "LOS" case, which is reported in Table 1, can characterize all the OV MV BPL topologies of 3, 2, 1 and 0 branches, respectively. This latter observation is used during the following analysis.

4.3 Performance of TIM and Advanced TIM

Prior to apply TIM and advanced TIM, a preliminary task is the preparation of the required OV MV BPL topology database in each case. The two OV MV BPL topology databases comprise all the possible topological configurations of OV MV BPL topologies concerning the number of branches, each branch distance from the transmitting end, each branch length and the required number of monotonic sections. Taking under consideration the topology database specifications of [24] and Table 1, the size requirements of the OV MV BPL topology databases are:

- ($k_{sect,max}$ - $k_{sect,min}$ + 1) approximated theoretical OV MV BPL coupling transfer function column vectors per each possible OV MV BPL topology of the database, which corresponds to the respective ($k_{sect,max}$ - $k_{sect,min}$ + 1) monotonic sections.
- 30 elements per each approximated theoretical OV MV BPL coupling transfer function column vector, which corresponds to the respective 30 measurement frequencies.
- When N branches are considered across the "LOS" transmission path, there are

$$\sum_{i_1=1}^{L/L_s+1}\left\{\sum_{i_2=1}^{i_1}\left\{\cdots\sum_{i_{N-1}=1}^{i_{N-2}}\left\{i_{N-1}\right\}\right\}\right\}\times\left(\frac{L_b}{L_s}+1\right)^N \tag{9}$$

possible OV MV BPL topologies that should be inserted in the OV MV BPL topology databases.

TABLE 1
Adaptive Number of Monotonic Sections of [27] and Monotonic Section Sets for the Indicative OV MV BPL Topologies when Different Maximum CUD Values Are Applied

Indicative OV MV BPL Topology	Maximum CUD Value	L1PMA		Advanced TIM and FIIM	
		Adaptive Number of Monotonic Sections	Cardinality of the Monotonic Section Set ($k_{\mathrm{sec}t,\max} - k_{\mathrm{sec}t,\min} + 1$)	Monotonic Section Set [$k_{\mathrm{sect,min}}$ $k_{\mathrm{sect,max}}$]	Cardinality of the Monotonic Section Set ($k_{\mathrm{sec}t,\max} - k_{\mathrm{sec}t,\min} + 1$)
Urban	0	12	20	[11 13]	3
	1	8	20	[7 9]	3
	2	10	20	[9 11]	3
	3	8	20	[7 9]	3
	4	10	20	[9 11]	3
	5	8	20	[7 9]	3
	6	8	20	[7 9]	3
	7	8	20	[7 9]	3
	8	8	20	[7 9]	3
	9	8	20	[7 9]	3
	10	4	20	[3 5]	3
Suburban	0	20	20	[19 20]	2
	1	16	20	[15 17]	3
	2	6	20	[5 7]	3
	3	18	20	[17 19]	3
	4	4	20	[3 5]	3
	5	10	20	[9 11]	3
	6	4	20	[3 5]	3
	7	4	20	[3 5]	3
	8	4	20	[3 5]	3
	9	4	20	[3 5]	3
	10	1	20	[1 2]	2
Rural	0	6	20	[5 7]	3
	1	6	20	[5 7]	3
	2	2	20	[1 3]	3
	3	2	20	[1 3]	3
	4	2	20	[1 3]	3
	5	1	20	[1 2]	2
	6	1	20	[1 2]	2
	7	2	20	[1 3]	3
	8	1	20	[1 2]	2
	9	1	20	[1 2]	2
	10	1	20	[1 2]	2
"LOS"	0	6	20	[5 7]	3
	1	6	20	[5 7]	3
	2	2	20	[1 3]	3
	3	2	20	[1 3]	3

	4	2	20	[1 3]	3
	5	2	20	[1 3]	3
	6	1	20	[1 2]	2
	7	2	20	[1 3]	3
	8	1	20	[1 2]	2
	9	1	20	[1 2]	2
	10	1	20	[1 2]	2

Taking under consideration the previous requirements, the OV MV BPL topology database specifications of Sec.4.1 and eq.(1) of [24], there are $\sum_{i_1=1}^{21}\left\{\sum_{i_2=1}^{i_1}\left\{\cdots\sum_{i_{N-1}=1}^{i_{N-2}}\{i_{N-1}\}\right\}\right\}\times 7^N\times \text{card}\left(k_{\text{sec}t,\max}-k_{\text{sec}t,\min}+1,0\right)\times 30$ elements required to be inserted in the database where $\text{card}\left(k_{\text{sec}t,\max}-k_{\text{sec}t,\min}+1,a_{CUD}\right)$ computes the cardinality of the monotonic section set when the maximum CUD value is equal to α_{CUD}. Recognizing the dependence of the number of elements on the term ($k_{\text{sect,max}}$ - $k_{\text{sect,min}}$ + 1), the size decrease of the advanced TIM database may reach up to 90%.

Numerically, the number of elements and the approximated time duration of inserting all the available OV MV BPL topologies for a specific number of branches is reported in Table 2 when the TIM and advanced TIM databases are created. Note that the system technical characteristics of [24] are assumed so that an approximation time duration can be delivered.

Already been reported in [24], it is also evident from Table 2 that the approximated time duration poses significant technical difficulties during the consideration of OV MV BPL topologies with high number of branches in the database regardless of the method applied, say either TIM or advanced TIM. However, the time reduction that is offered by the advanced TIM is significant even from the two-branch OV MV BPL topologies. Anyway, advanced TIM is the first step of the future research towards the need for the optimization of the insertion methodology in topology database is among the critical steps of the future research [24], [25]. Similarly to [24], only the cases of "LOS" case and topologies with one branch are considered during the comparison between TIM and advanced TIM for the sake of simplicity and speed (see Sec.VE).

Since the OV MV BPL topology databases are available, TIM and advanced TIM can now be applied if the three steps of Sec.3.2 are followed, namely:

1. The measured OV MV BPL coupling transfer function column vector $\overline{\mathbf{H}^{\text{WtG}}}(\mathbf{f})$ and the approximated OV MV BPL coupling transfer function column vector $\overline{\overline{\mathbf{H}_{\text{meas}}^{\text{WtG}}}}(\mathbf{f},k_{\text{sect}})$ are computed for different number of monotonic sections as reported in Table 1 for TIM and advanced TIM (see the column of the cardinality of the monotonic section set).

TABLE 2
Number of OV MV BPL Topologies, Elements and Approximated Time Duration of Topology Databases

Number of Branches	Number of Topologies	TIM		Advanced TIM		Time Reduction (%)
		Number of Elements	Approximated Time Duration (hours)	Number of Elements	Approximated Time Duration (hours)	
0	1	600	0.003	90	0.0005	83.33
1	147	92,610	0.50	13,230	0.07	85.71
2	11,319	7,130,970	38.43	679,140	3.66	90.48
3	607,453	382,695,390	2062	54,670,770	294.61	85.71

2. With reference to eq. (3), the OV MV BPL topology database and the approximated measured OV MV BPL coupling transfer functions, the $CSPM_{tot}$ of the indicative topologies is calculated with respect to the topologies of the database. In Fig. 2(a), the $CSPM_{tot}$ of the indicative rural OV MV BPL topology is plotted versus the maximum CUD value a_{CUD} for TIM and advanced TIM. In Fig. 2(b), the position among the 1 + 147 = 148 OV MV BPL topologies of the database in ascending $CSPM_{tot}$ order is plotted versus the maximum CUD value a_{CUD} for TIM and advanced TIM when the indicative rural case is examined. In Fig. 3(a) and 3(b), similar curves with Figs. 2(a) and 2(b) are presented, respectively, but for the indicative "LOS" topology.
3. A set of candidate OV MV BPL topologies with their respective $CSPM_{tot}$ is provided by the TIM and advanced TIM as it is shown in Figs. 2(b) and 3(b). All these topologies present the same $CSPM_{tot}$ and coincide at the first position in ascending $CSPM_{tot}$ order.

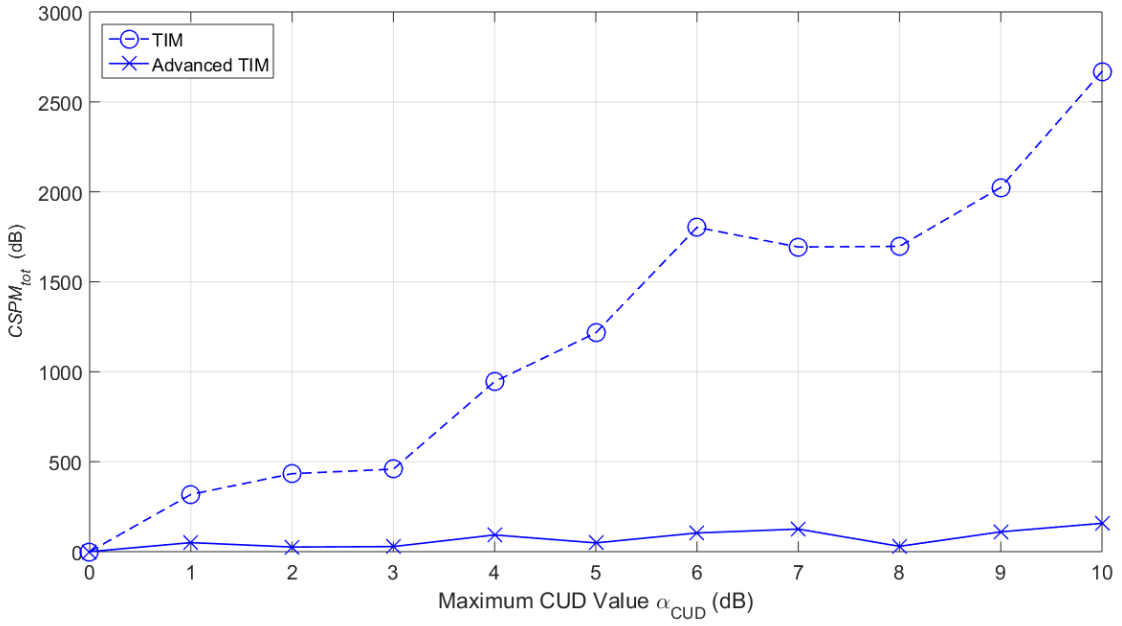

(a)

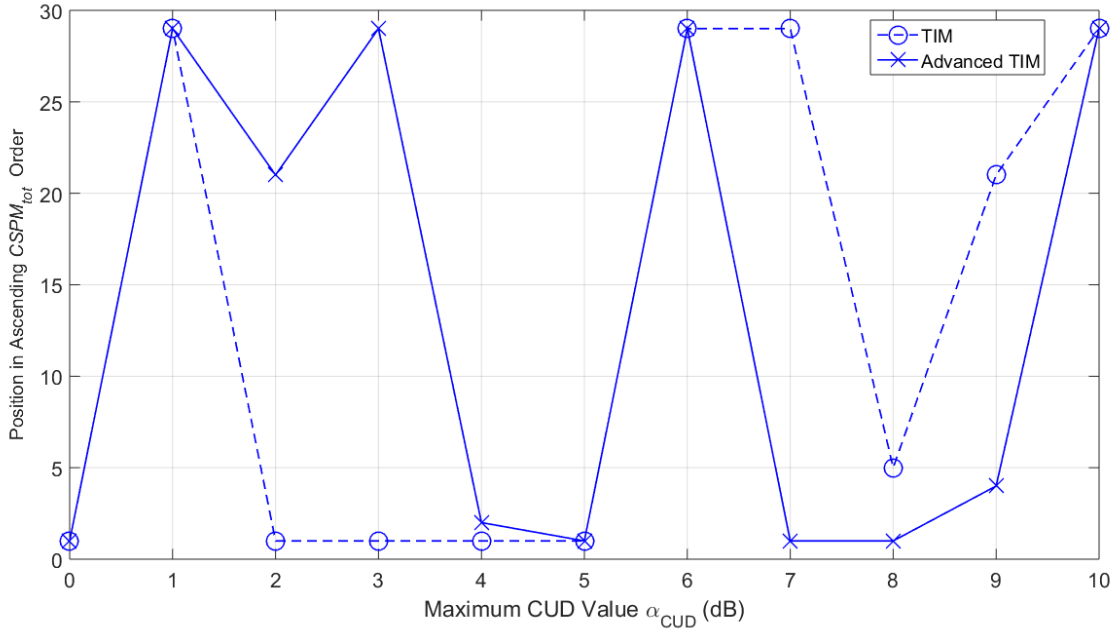

(b)

Figure 2. $CSPM_{tot}$ and position in ascending $CSPM_{tot}$ order versus maximum CUD value when TIM (⊖) and advanced TIM (✕) are applied in indicative rural case.

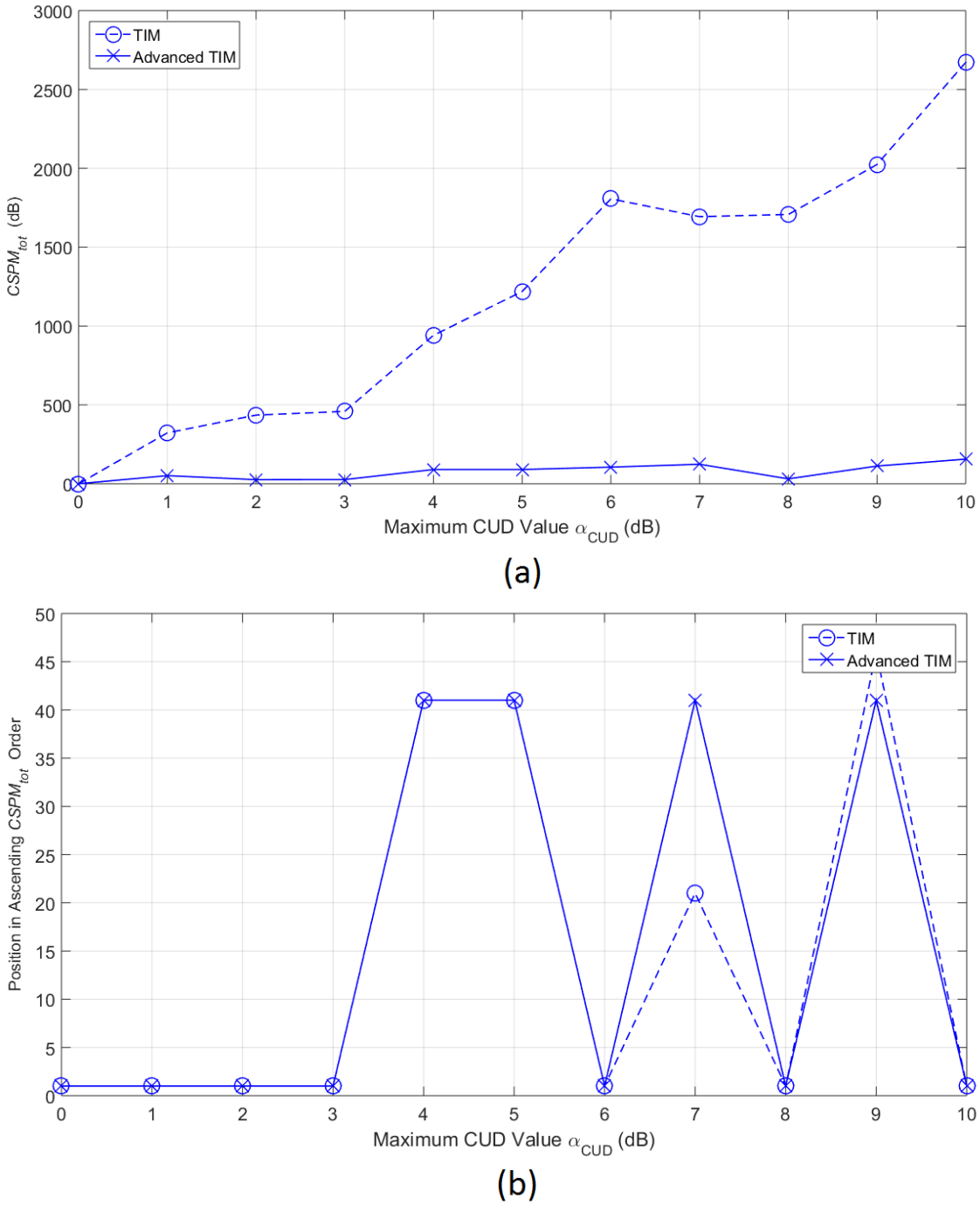

Figure 3. Same with Figure 2 but for the indicative "LOS" case.

From Figs. 2(a), 2(b), 3(a) and 3(b), several interesting observations concerning the performance of TIM and advanced TIM can be pointed out:

- Comparing the aforementioned figures with Figs. 5(a)-(d) of [24], it is shown that TIM efficiently copes with either OV HV BPL topologies or OV MV BPL ones. This is due to the fact that the poor multipath transmission environment of OV HV BPL networks has as a result the presence of coupling transfer functions that present great similarities each other, thus, creating a great set of candidate OV HV

BPL topologies. In contrast, the set of candidate OV MV BPL topologies comprises fewer elements and significant position fluctuations may occur.

- Both TIM and advanced TIM satisfactorily identify the real OV MV BPL topology even if maximum CUD values that reach up to 10dB are assumed. In accordance with [24], the identification performance of TIM and advanced TIM is significantly higher than the respective one of the traditional identification methods that focus on the comparison of the measured OV MV BPL coupling transfer function data with the theoretical ones. Anyway, TIM seems to better identify the real OV MV BPL topologies when low maximum CUD values occur whereas advanced TIM has better identification performance when high maximum CUD values occur.
- Similarly to [24], $CSPM_{tot}$ values of TIM define the accuracy of the topology identification. In fact, higher values of $CSPM_{tot}$ imply that topologies of either rich multipath environment or strongly contaminated by measurement differences are examined while $CSPM_{tot}$ difference between the candidate OV MV BPL topologies of the set and the first topology outside the set decreases. Here, a mask of secure topology identification can be defined that mainly depends on the examined OV MV BPL topology and maximum CUD value. Anyway, this mask is easily applicable to TIM because of its higher $CSPM_{tot}$ values.
- Since an OV MV BPL topology can be almost uniquely identified by the form of $CSPM_{tot}$ against various maximum CUD values, significant $CSPM_{tot}$ deviations that occur during the operation of an OV MV BPL topology imply that either a fault or instability may be arisen. This is the conceptual basis for FIIM of [25] so that faults or instabilities across an intelligent energy system can be identified.
- In order to further compare advanced TIM against TIM, the number of OV MV BPL topologies, elements and approximated time duration that are required to create the topology databases of advanced TIM and TIM are reported in Table 2. Although TIM and advanced TIM present approximately the same performance to identify an OV MV BPL topology from the respective database –see Figs. 2(a), 2(b), 3(a) and 3(b)–, the time reduction during the creation of the OV MV BPL topology database that is gained by the advanced TIM application is significant –see the respective columns of Approximated Time Duration in Table 2–.

4.4 Performance of FIIM and Advanced FIIM

As already been reported in Sec. 3.3, FIIM and advanced FIIM can identify four problematic conditions when these occur in OV MV BPL topologies, namely: (i) *Fault in main distribution lines*; (ii) *Fault in branch lines*; (iii) *Instability in branch interconnections* –see Fig. 1(d)–; and (iv) *Instability in branch terminations* –see Fig. 1(e)–. In total, FIIMs can recognize either the fault or the instability condition and warn the responsible personnel. OV MV BPL topologies that suffer from faults or instabilities are treated as modified OV MV BPL topologies and characterized by new respective OV MV BPL coupling transfer functions and measurement differences.

4.4.1 Fault in Main Distribution Line

As a fault in main distribution lines is assumed, an immediate communications failure in the OV MV BPL topology occurs. If transmitting and receiving ends operate in

stable conditions then a warning of fault in main distribution line is issued to the responsible personnel.

4.4.2 Fault in Branch Line

In accordance with [25], a fault in branch lines implies that a branch line is interrupted and an open circuit at the fault occurs. With reference to Fig. 1(c), let the first branch of each indicative OV MV BPL topology be broken at 2m from the branching interconnection A_1 with the main distribution line. The modified OV MV BPL topology is characterized by more frequent and deeper spectral notches due to the fact that a new shorter branch creates a richer multipath environment. In Fig. 4(a), FIIM CSPpM of the original urban OV MV BPL topology, FIIM CSPpM* of the modified urban OV MV BPL topology and their FIIM $\Delta CSPpM^*$ are plotted versus the maximum CUD value of the occurred measurement differences, which is assumed to be common for the two applied CUDs. Similar curves with Fig. 4(a) are given in Fig. 4(b) but for the application of the advanced FIIM. Similar curves with Figs. 4(a) and 4(b) are given in Figs. 4(c) and 4(d) for the suburban case and in Figs. 4(e) and 4(f) for the rural case.

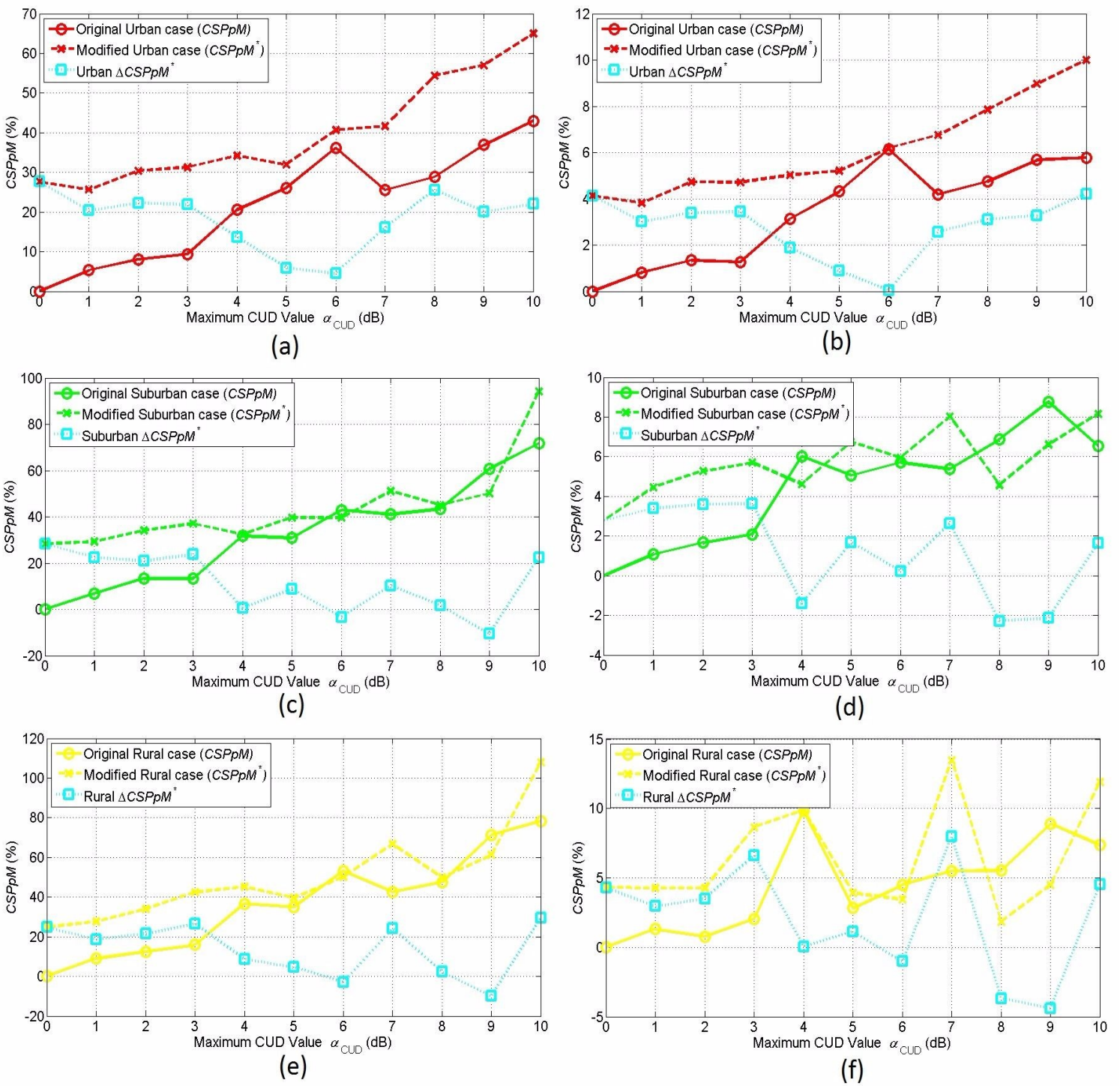

Figure 4. Fault in the first branch of the indicative OV MV BPL topologies and the behavior of CSPpMs and ΔCSPpM*. (a) FIIM / Urban case. (b) Advanced FIIM / Urban case. (c) FIIM / Suburban case. (d) Advanced FIIM / Suburban case. (e) FIIM / Rural case. (f) Advanced FIIM / Rural case.

From Figs. 4(a)-(f), it is evident that OV MV BPL topologies that suffer from a fault in their branch lines are characterized by modified OV MV BPL coupling transfer functions that differ from the original ones. These differences are reflected on CSPM*

and CSPM, respectively. Especially, the difference, which is expressed by the respective ΔCSPpM curves, is easily observable when measurement differences remain relatively low. As the measurement differences increase, measurement differences become important affecting the original form of the OV MV BPL coupling transfer functions and the identification potential of branch faults. Although the accuracy of FIIM and advanced FIIM to identify the faults in branch lines remains almost the same, advanced FIIM presents better computational speed in comparison with FIIM. However, both methods fail to identify faults of high maximum CUD value when these faults occur in OV MV BPL topologies of low branch complexity –e.g., see Figs. 4(e)-(f) when the maximum CUD value is equal to 8 or 9dB–.

4.4.3 Instability in Branch Interconnection

Branch interconnections connect main lines with branch ones and establish the stable power flow till the MV/LV transformers. In this section, the performance of FIIM and advanced FIIM to identify instabilities that occurs in a branch interconnection is investigated in this subsection. With reference to Fig. 1(d), the interruption of the last branch at the point A_N cancels the presence of this branch. The modified (N-1)-branch OV MV BPL topology comes from the original N-branch one.

Similarly to branch line faults, in Fig. 5(a), CSPpM of the original urban OV MV BPL topology, CSPpM* of the modified urban OV MV BPL topology and their $\Delta CSPpM^*$s are plotted versus the CUD maximum value of the occurred measurement differences when FIIM is applied. Similar curves with Fig. 5(a) are given in Fig. 5(b) but for the application of the advanced FIIM. Similar curves with Figs. 5(a) and 5(b) are given in Figs. 5(c) and 5(d) for the suburban case and in Figs. 5(e) and 5(f) for the rural case.

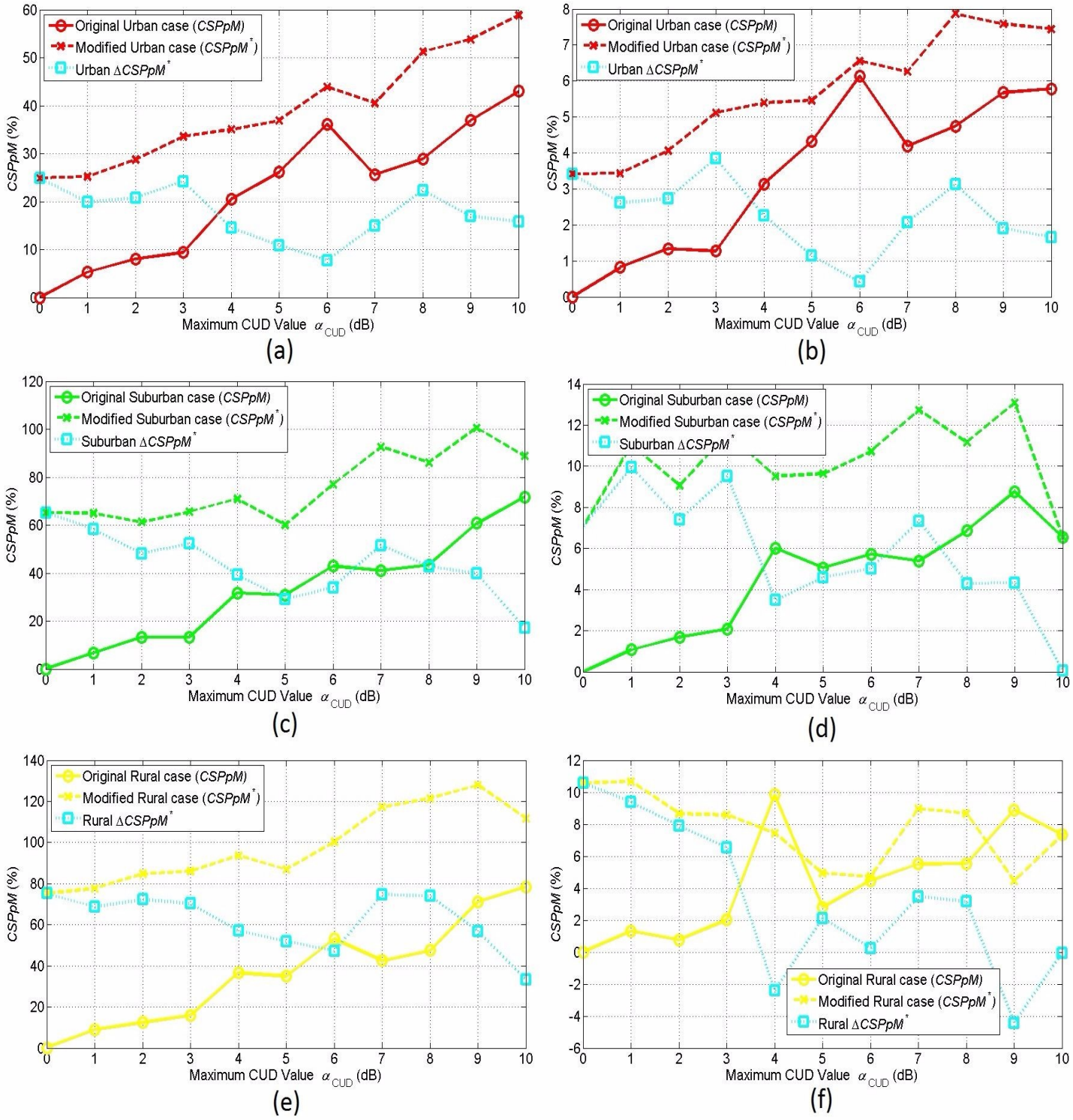

Figure 5. Instability in the branch interconnection of the last branch of the indicative OV MV BPL topologies and the behavior of CSPpMs and ΔCSPpM*. (a) FIIM / Urban case. (b) Advanced FIIM / Urban case. (c) FIIM / Suburban case. (d) Advanced FIIM / Suburban case. (e) FIIM / Rural case. (f) Advanced FIIM / Rural case.

From Figs. 5(a)-(f), $\Delta CSPpM^*$ of FIIM and advanced FIIM can identify the branch interconnection instability regardless of the considered OV MV BPL topology and the applied CUD magnitude. Although the identification of the branch interconnection instability becomes more challenging as the maximum CUD value increases, $\Delta CSPpM^*$ triggers the alarm in all the cases examined except for the application of FIIM in rural case when maximum CUD value exceeds 9dB. Therefore, FIIM and advanced FIIM present almost the same identification performance of a branch interconnection instability but advanced FIIM is characterized by better execution times.

4.4.4 Instability in Branch Terminations

This subsection examines the possibility of identifying an instability that occurs in a branch termination. With reference to Fig. 1(e), let the branch termination of the first branch of each indicative OV MV BPL topology act as short circuit termination. This short circuit at the first branch termination may come up from a short circuit inside a MV/LV transformer. FIIM and advanced FIIM can identify the instability in branch terminations by applying $\Delta CSPpM^*$. Similarly to branch line faults and branch interconnection instabilities, in Fig. 6(a), CSPpM of the original urban OV MV BPL topology, CSPpM* of the modified urban OV MV BPL topology and their $\Delta CSPpM^*$ are plotted versus the CUD maximum value of the occurred measurement differences when FIIM is applied. Similar curves with Fig. 6(a) are given in Fig. 6(b) but for the application of the advanced FIIM. Similar curves with Figs. 6(a) and 6(b) are given in Figs. 6(c) and 6(d) for the suburban case and in Figs. 5(e) and 5(f) for the rural case.

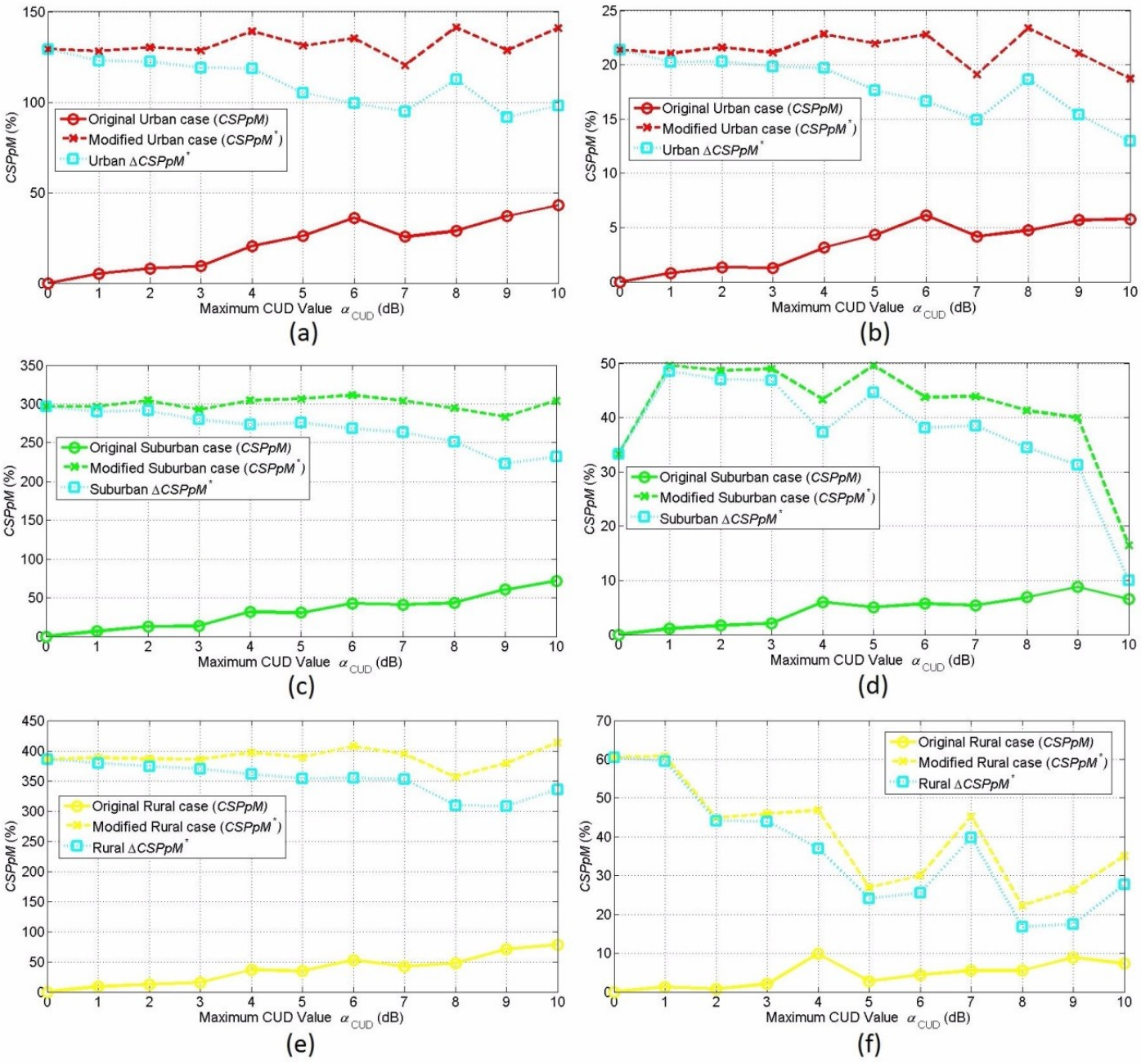

Figure 6. Instability in the branch termination (short circuit) of the first branch of the indicative OV MV BPL topologies and the behavior of CSPpMs and ΔCSPpM*. (a) FIIM / Urban case. (b) Advanced FIIM / Urban case. (c) FIIM / Suburban case. (d) Advanced FIIM / Suburban case. (e) FIIM / Rural case. (f) Advanced FIIM / Rural case.

From Figs. 6(a)-(f), both FIIM and advanced FIIM can easily identify any damage that may affect pieces of equipment across the distribution power grid. This is clear from the comparison among the previous figures where various faults and instabilities occur. In the case of the short circuit termination, there is not only one case where $\Delta CSPpM^*$ lies below 0dB. The identification of the instability remains easy even if high maximum CUD values are encountered that exceed 6-7dB. Again, FIIM and advanced FIIM present almost the same identification performance of a branch termination instability but advanced FIIM is characterized by better execution times.

4.5 General Remarks Regarding TIM, Advanced TIM, FIIM and Advanced FIIM

Already been mentioned in [24], [25], TIM, advanced TIM, FIIM and advanced FIIM can act as invaluable smart grid applications towards the power stability of the transmission and power grids.

Among the research goals that have been presented in [25], advanced TIM and advanced FIIM can successfully cope with the challenges of the BPL topology identification as well as the fault and instability identification. Actually, advanced TIM performance towards the identification of OV MV BPL topologies remains almost the same with TIM, as described in Figs. 2(a), 2(b), 3(a) and 3(b), but reducing significantly the approximated time duration as well as the complicacy of the examined OV MV BPL topologies. In accordance with Table 2, the key of advanced TIM that allows the reduction of the approximated time duration is the adoption of the concept of the adaptive number of monotonic sections presented in [27] when the required OV MV BPL topology database is prepared. Similarly to advanced TIM, advanced FIIM performance remains almost the same with FIIM when the problematic conditions of Secs. 4.4.1-4.4.4 occur. Again, advanced FIIM execution time is drastically reduced comparing with the respective time of FIIM.

5. Conclusions

In this paper, TIM and FIIM have first applied to distribution power grids while the respective advanced TIM and advanced FIIM have been proposed.

As the validation of the TIM and advanced TIM are concerned, a set of candidate OV MV BPL topologies has been revealed with the real original topology lying inside the set by using the TIM performance metric of $CSPM_{tot}$. Even though measurement differences of various maximum CUD values have been assumed, TIM and advanced TIM have satisfactorily achieved to identify the real original topology with almost the same accuracy. However, advanced TIM succeeds in identifying original OV MV BPL topologies with significant shorter execution times in comparison with TIM.

As regards the validation of the FIIM and advanced FIIM, four problematic conditions (i.e., faults in main distribution lines, faults in branch lines, instabilities in branch interconnections and instabilities in branch terminations) have been easily identified. Through FIIM performance metric of $\Delta CSPpM^*$, FIIM and advanced FIIM have successfully managed to identify the four problematic conditions. Again, advanced FIIM presents significantly shorter execution times when OV MV BPL topologies are examined in comparison with FIIM.

Exploiting the virtues of the emerging intelligent energy systems, advanced TIM and FIIM complete another step towards the real time surveillance and monitoring of transmission and distribution power grid.

References

[1] K. Ali, I. Pefkianakis, A. X. Liu, and K. H. Kim, "Boosting PLC Networks for High-Speed Ubiquitous Connectivity in Enterprises," arXiv preprint arXiv:1608.06574, 2016, [Online]. Available: http://arxiv.org/pdf/1608.06574v1.pdf

[2] A. G. Lazaropoulos, "Best L1 Piecewise Monotonic Data Approximation in Overhead and Underground Medium-Voltage and Low-Voltage Broadband over Power Lines Networks: Theoretical and Practical Transfer Function Determination," *Hindawi Journal of Computational Engineering*, vol. 2016, Article ID 6762390, 24 pages, 2016. DOI:10.1155/2016/6762390. [Online]. Available: https://www.hindawi.com/journals/jcengi/2016/6762390/cta/

[3] C. Cano, A.Pittolo, D. Malone, L. Lampe, A. M.Tonello, and A. Dabak, "State-of-the-art in Power Line Communications: From the Applications to the Medium," *IEEE J. Sel. Areas Commun.*,vol. 34, pp. 1935-1952, 2016.

[4] L. Lampe, A. M. Tonello, and T. G. Swart, *Power Line Communications: Principles, Standards and Applications from Multimedia to Smart Grid*. John Wiley & Sons, 2016.

[5] A. G. Lazaropoulos and P. G. Cottis, "Transmission characteristics of overhead medium voltage power line communication channels," *IEEE Trans. Power Del.*, vol. 24, no. 3, pp. 1164-1173, Jul. 2009.

[6] A. G. Lazaropoulos and P. G. Cottis, "Capacity of overhead medium voltage power line communication channels," *IEEE Trans. Power Del.*, vol. 25, no. 2, pp. 723-733, Apr. 2010.

[7] A. G. Lazaropoulos and P. G. Cottis, "Broadband transmission via underground medium-voltage power lines-Part I: transmission characteristics," *IEEE Trans. Power Del.*, vol. 25, no. 4, pp. 2414-2424, Oct. 2010.

[8] A. G. Lazaropoulos and P. G. Cottis, "Broadband transmission via underground medium-voltage power lines-Part II: capacity," *IEEE Trans. Power Del.*, vol. 25, no. 4, pp. 2425-2434, Oct. 2010.

[9] A. G. Lazaropoulos, "Broadband transmission characteristics of overhead high-voltage power line communication channels," *Progress in Electromagnetics Research B*, vol. 36, pp. 373-398, 2012. [Online]. Available: http://www.jpier.org/PIERB/pierb36/19.11091408.pdf

[10] A. G. Lazaropoulos, "Capacity Performance of Overhead Transmission Multiple-Input Multiple-Output Broadband over Power Lines Networks: The Insidious Effect of Noise and the Role of Noise Models," *Trends in Renewable Energy*, vol. 2, no. 2, pp. 61-82, Jan. 2016. DOI: 10.17737/tre.2016.2.2.0023

[11] Homeplug, Technology Gains Momentum, 2013, [Online]. Available: http://www.businesswire.com

[12] Homeplug, AVWhitepaper, 2007, [Online]. Available: http://www.homeplug.org/techresources/resources/

[13] Homeplug, AV2Whitepaper, 2011, [Online]. Available: http://www.homeplug.org/techresources/resources/

[14] A. G. Lazaropoulos, "Factors Influencing Broadband Transmission Characteristics of Underground Low-Voltage Distribution Networks," *IET Commun.*, vol. 6, no. 17, pp. 2886-2893, Nov. 2012.

[15] A. G. Lazaropoulos, "Towards broadband over power lines systems integration: Transmission characteristics of underground low-voltage distribution power lines," *Progress in Electromagnetics Research B*, 39, pp. 89-114, 2012. [Online]. Available: http://www.jpier.org/PIERB/pierb39/05.12012409.pdf

[16] A. G. Lazaropoulos, "Broadband transmission and statistical performance properties of overhead high-voltage transmission networks,"*Hindawi Journal of Computer Networks and Commun.*, 2012, article ID 875632, 2012. [Online]. Available: http://www.hindawi.com/journals/jcnc/aip/875632/

[17] A. G. Lazaropoulos, "Towards modal integration of overhead and underground low-voltage and medium-voltage power line communication channels in the smart grid landscape: model expansion, broadband signal transmission characteristics, and statistical performance metrics (Invited Paper)," *ISRN Signal Processing*, vol. 2012, Article ID 121628, 17 pages, 2012. [Online]. Available: http://www.isrn.com/journals/sp/aip/121628/

[18] A. G. Lazaropoulos, "Review and Progress towards the Common Broadband Management of High-Voltage Transmission Grids: Model Expansion and Comparative Modal Analysis," *ISRN Electronics*, vol. 2012, Article ID 935286, pp. 1-18, 2012. [Online]. Available: http://www.hindawi.com/isrn/electronics/2012/935286/

[19] A. G. Lazaropoulos, "Review and Progress towards the Capacity Boost of Overhead and Underground Medium-Voltage and Low-Voltage Broadband over Power Lines Networks: Cooperative Communications through Two- and Three-Hop Repeater Systems," *ISRN Electronics*, vol. 2013, Article ID 472190, pp. 1-19, 2013. [Online]. Available: http://www.hindawi.com/isrn/electronics/aip/472190/

[20] A. G. Lazaropoulos, "Green Overhead and Underground Multiple-Input Multiple-Output Medium Voltage Broadband over Power Lines Networks: Energy-Efficient Power Control," *Springer Journal of Global Optimization*, vol. 2012 / Print ISSN 0925-5001, pp. 1-28, Oct. 2012.

[21] P. Amirshahi and M. Kavehrad, "High-frequency characteristics of overhead multiconductor power lines for broadband communications," *IEEE J. Sel. Areas Commun.*, vol. 24, no. 7, pp. 1292-1303, Jul. 2006.

[22] T. Sartenaer, "Multiuser communications over frequency selective wired channels and applications to the powerline access network," Ph.D. dissertation, Univ. Catholique Louvain, Louvain-la-Neuve, Belgium, Sep. 2004.

[23] T. Calliacoudas and F. Issa, ""Multiconductor transmission lines and cables solver," An efficient simulation tool for plc channel networks development," presented at the *IEEE Int. Conf. Power Line Communications and Its Applications*, Athens, Greece, Mar. 2002.

[24] A. G. Lazaropoulos, "Measurement Differences, Faults and Instabilities in Intelligent Energy Systems – Part 1: Identification of Overhead High-Voltage Broadband over Power Lines Network Topologies by Applying Topology Identification Methodology (TIM)," *Trends in Renewable Energy*, vol. 2, no. 3, pp. 85 – 112, Oct. 2016. DOI: 10.17737/tre.2016.2.3.0026

[25] A. G. Lazaropoulos, "Measurement Differences, Faults and Instabilities in Intelligent Energy Systems – Part 2: Fault and Instability Prediction in Overhead High-Voltage Broadband over Power Lines Networks by Applying Fault and Instability Identification Methodology (FIIM)," *Trends in Renewable Energy*, vol. 2, no. 3, pp. 113 – 142, Oct. 2016. DOI: 10.17737/tre.2016.2.3.0027

[26] A. G. Lazaropoulos, "Power Systems Stability through Piecewise Monotonic Data Approximations – Part 1: Comparative Benchmarking of L1PMA, L2WPMA and L2CXCV in Overhead Medium-Voltage Broadband over Power Lines Networks," *Trends in Renewable Energy*, vol. 3, no. 1, pp. 2 – 32, Jan. 2017. DOI: 10.17737/tre.2017.3.1.0029

[27] A. G. Lazaropoulos, "Power Systems Stability through Piecewise Monotonic Data Approximations – Part 2: Adaptive Number of Monotonic Sections and Performance of L1PMA, L2WPMA and L2CXCV in Overhead Medium-Voltage Broadband over Power Lines Networks," *Trends in Renewable Energy*, vol. 3, no. 1, pp. 33 – 60, Jan. 2017. DOI: 10.17737/tre.2017.3.1.0030

[28] P. Amirshahi, "Broadband access and home networking through powerline networks" Ph.D. dissertation, Pennsylvania State Univ., University Park, PA, May 2006. [Online]. Available: http://etda.libraries.psu.edu/theses/approved/WorldWideIndex/ETD-1205/index.html

[29] M. D'Amore and M. S. Sarto, "Simulation models of a dissipative transmission line above a lossy ground for a wide-frequency range-Part I: Single conductor configuration," *IEEE Trans. Electromagn. Compat.*, vol. 38, no. 2, pp. 127-138, May 1996.

[30] M. D'Amore and M. S. Sarto, "Simulation models of a dissipative transmission line above a lossy ground for a wide-frequency range-Part II: Multi-conductor configuration," *IEEE Trans. Electromagn. Compat.*, vol. 38, no. 2, pp. 139-149, May 1996.

[31] A. Milioudis, G. T. Andreou, and D. P. Labridis, "Detection and location of high impedance faults in multiconductor overhead distribution lines using power line communication devices," *IEEE Trans. on Smart Grid*, vol. 6, no. 2, pp. 894-902, 2015.

[32] A. G. Lazaropoulos, "Designing Broadband over Power Lines Networks Using the Techno-Economic Pedagogical (TEP) Method – Part I: Overhead High Voltage Networks and Their Capacity Characteristics (Invited Review Article)," *Trends in Renewable Energy*, vol. 1, no. 1, pp. 16-42, Mar. 2015. DOI: 10.17737/tre.2015.1.1.002

[33] A. G. Lazaropoulos, "Designing Broadband over Power Lines Networks Using the Techno-Economic Pedagogical (TEP) Method – Part II: Overhead Low-Voltage and Medium-Voltage Channels and Their Modal Transmission Characteristics," *Trends in Renewable Energy*, vol. 1, no. 2, pp. 59-86, Jun. 2015. DOI: 10.17737/tre.2015.1.2.006

[34] T. Sartenaer and P. Delogne, "Deterministic modelling of the (Shielded) outdoor powerline channel based on the multiconductor transmission line equations," *IEEE J. Sel. Areas Commun.*, vol. 24, no. 7, pp. 1277-1291, Jul. 2006.

[35] A. G. Lazaropoulos, "Policies for Carbon Energy Footprint Reduction of Overhead Multiple-Input Multiple-Output High Voltage Broadband over Power

Lines Networks," *Trends in Renewable Energy*, vol. 1, no. 2, pp. 87-118, Jun. 2015. DOI: 10.17737/tre.2015.1.2.0011

[36] A. G. Lazaropoulos, "Wireless Sensor Network Design for Transmission Line Monitoring, Metering and Controlling: Introducing Broadband over PowerLines-enhanced Network Model (BPLeNM)," *ISRN Power Engineering*, vol. 2014, Article ID 894628, 22 pages, 2014. DOI: 10.1155/2014/894628. [Online]. Available: http://www.hindawi.com/journals/isrn.power.engineering/2014/894628/

[37] A. G. Lazaropoulos, "Wireless Sensors and Broadband over PowerLines Networks: The Performance of Broadband over PowerLines-enhanced Network Model (BPLeNM) (Invited Paper)," *ICAS Publishing Group Transaction on IoT and Cloud Computing*, vol. 2, no. 3, pp. 1-35, 2014. [Online]. Available: http://icas-pub.org/ojs/index.php/ticc/article/view/27/17

[38] A. G. Lazaropoulos, "The Impact of Noise Models on Capacity Performance of Distribution Broadband over Power Lines (BPL) Networks," *Hindawi Computer Networks and Communications*, vol. 2016, Article ID 5680850, 14 pages, 2016. doi:10.1155/2016/5680850. [Online]. Available: http://www.hindawi.com/journals/jcnc/2016/5680850/

[39] I. C. Demetriou and M. J. D. Powell, "Least squares smoothing of univariate data to achieve piecewise monotonicity,"*IMA J. of Numerical Analysis*, vol. 11, pp. 411-432, 1991.

[40] I. C. Demetriou and V. Koutoulidis, "On Signal Restoration by Piecewise Monotonic Approximation", in Lecture Notes in Engineering and Computer Science: *Proceedings of The World Congress on Engineering 2013*,London, U.K., Jul. 2013, pp. 268-273.

[41] I. C. Demetriou, "An application of best *L*1 piecewise monotonic data approximation to signal restoration," *IAENG International Journal of Applied Mathematics*, vol. 53, no. 4, pp. 226-232, 2013.

[42] I. C. Demetriou, "L1PMA: A Fortran 77 Package for Best L1 Piecewise Monotonic Data Smoothing," *Computer Physics Communications*, vol. 151, no. 1, pp. 315-338, 2003.

[43] I. C. Demetriou, "Data Smoothing by Piecewise Monotonic Divided Differences,"*Ph.D. Dissertation*, Department of Applied Mathematics and Theoretical Physics, University of Cambridge, Cambridge, 1985.

[44] I. C. Demetriou, "Best L1 Piecewise Monotonic Data Modelling,"*Int. Trans. Opl Res.*, vol. 1, no. 1, pp. 85-94,1994.

Trends in Renewable Energy
OPEN ACCESS ISSN: 2376-2144
Peer-Reviewed Article futureenergysp.com/index.php/tre

Bioelectricity Generation using Carbon Felt Electrode in Microbial Fuel Cell (MFC) Inoculated with Mixed Cultures

Shishir Kanti Pramanik[1*], Md. Mohosin Rana[2]

[1]*Department of Chemistry, School of Physical Sciences, Shahjalal University of Science and Technology, Sylhet -3114, Bangladesh.*
[2]*Department of Genetic Engineering and Biotechnology, School of Life Sciences, Shahjalal University of Science and Technology, Sylhet -3114, Bangladesh.*

[*]*Corresponding Author:* Shishir Kanti Pramanik; Phone: +88-0821-716123, Fax: +88-0821-715257, E-mail: shishir_kantif@yahoo.com

Received June 19, 2017; Accepted July 6, 2017; Published July 7, 2017

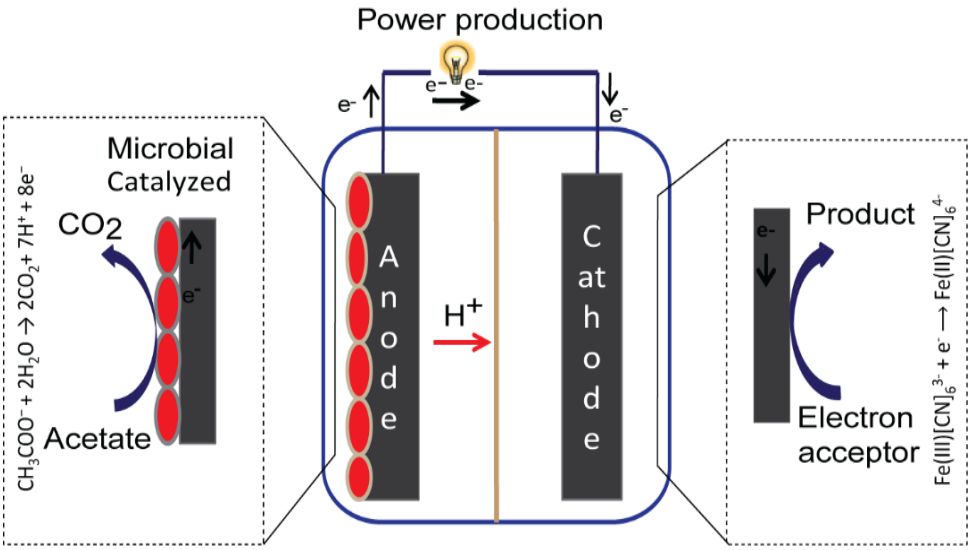

Microbial fuel cell (MFC) that was configured with the carbon felt electrode and the cation exchange membrane, and inoculated with mixed culture was demonstrated to yield bioelectricity. The cell was operated under four external loads with pHs ranging from 4 to 10 and the total cell operation was monitored up to 25 days. The presented results revealed that the potentiality of maximum current and power production was achieved while hexacyanoferrate(III) used as a cathodic reaction and at neutral pH condition of media. The maximum current density 2.5 Am^{-2} and power density 1410 mWm^{-2} were observed on the 25th day at an anode potential of -378 mV. Stable and steady power was produced by MFC on the day 22nd to 25th when cell operated at 250 Ω external load. The internal resistance of the fuel cell was decreased with the increase of the operation time. Coulombic efficiency (CE %) was found 22.70 % at the stable phase of fuel cell operation.

Keywords: MFC; Bioelectricity; Carbon felt; Mixed culture microorganisms; Power density

Introduction

In the recent years, green energy production utilizing renewable resources is becoming an active area of research in the research fraternity. Ethanol, bio-diesel, bio-hydrogen, and bioelectricity production from waste materials are finding prominence in this direction [1-2]. Now, the efforts are devoted in developing alternative electricity production methods. New electricity production from renewable resources is much indispensable [3-4]. In this regard, microbial fuel cell (MFC) is a promising technology that can convert biodegradable materials *e.g.* organic materials present in wastewater, into clean and renewable electricity. In MFC, bacteria can be used to convert the energy stored in the chemical bonds of organic compounds into electrical energy [5].

Electrochemically active microorganisms play a crucial role in the generation of electricity through MFC by oxidizing different biodegradable materials to CO_2 and protons for their growth while transferring the electrons towards a solid electrode [5]. Electron transfer from the microorganisms to the electrode was explained by several proposed mechanisms [6-7]. In MFC, anodic oxidation is accompanied by a cathodic reduction that is enclosed in a separate compartment [8]. An external electrical circuit is used with a resistor or by the power user to transfer electrons from the anode to the cathode. Protons and other cations are transferred from the anode to the cathode through a cation exchange membrane in order to close the circuit and maintain electroneutrality in both anodic and cathodic compartments.

The performance of the MFC mainly relies on the materials and the reactor configuration, and the microorganisms that required to produce the current [5, 9]. Power output from the MFC is thus affected by the variations in these operating conditions. Thus, based on these factors, different mediators and their different configurations, wide variety of substrates and anode inoculum were studied to increase the efficiency in the conversion of electricity from substrate [1, 10-11]. In the MFC, microorganisms act as a catalyst in the transfer of electrons from the substrate to the anode, thus, high performing microbial consortium (either pure or mixed culture) is very important to enhance MFC performance [12-13]. Up until now, it has been reported that the mixed cultures used in MFC have greater potentiality to produce power densities than those using pure cultures [9, 14-15]. Wastewater is often considered as a rich source of a variety of exoelectrogenic bacteria and thus it could be used in the MFC to increase its performance [16-17]. A mixed culture of bacteria often consists of different type of exoelectrogenic bacteria including *Geobactor sp.*, *Pseudomonas sp.*, *Bacillus sp*., *Shewanella sp*., *Brevibacillus sp.*, and so on, which serve as the bacterial inoculum for the formation of primary electrochemically active biofilm on carbon electrode [9,15]. The mixed culture electroactive biofilms were consisted of these different types of bacteria that vary in morphology from spherical, rod, and oval shape. Bacteria, such as spherical and rod shape, shows the presence of nanowires (pili), which can be responsible for extracellular electron transfer (EET). For producing the bioelectricity, the electrons generated by the bacteria upon the oxidation of organic substrate could be transported effectively through these living nanowires to an electrode [9].

Porous carbon-based materials such as graphite granules, graphitic felt, carbon cloth, and reticulated vitreous carbon (RVC) have been used currently as the anode of the MFC to make the entire process more economically feasible [18]. Relatively cheap and porous nature of carbon-based materials are becoming attractive because their high specific surface areas lead to the high volumetric activity. To increase the power production,

different strategies have been reported, for example, precipitating iron oxide onto carbon electrodes [19], adding Mn^{4+} [20], Fe_3O_4, or Fe_3O_4 and Ni^{2+} to graphite anodes [21], ammonia treatment of carbon cloth anodes [22]. However, inefficient attachment of bacterial nanowires to carbon cloth electrodes could be the cause of limiting power production.

The eventual aim of this study was to investigate bioelectricity production as well as power production by mixed culture MFC, in which the plain carbon felt was used as the electrode materials. The overall MFC performance was evaluated in terms of maximum power based on polarization and power density curves, internal resistance, and columbic efficiency (CE).

Materials and Methods

Microbial fuel cell design and setup

The experiments were conducted in the same electrochemical cell as described previously [23]. MFC consists of two plexiglass plates containing a single flow channel, two electrodes, and two plexiglass support plates (Figure 1A). The two plates with the flow channel were separated by the cation exchange membrane (Fumasep FKB, Fumatech, St. Ingbert, Germany). The other side of the flow channel faced the electrode. Both the anode and the cathode were made with the carbon felt. The projected surface area of the both electrodes in contact with the solution was 22 cm^2, and the volume of the flow channel was 33 mL (11.2 cm length × 2.0 cm width × 1.5 cm height). Both inlet and outlet of the anode and cathode chambers were connected to a 600 mL glass reservoir. The cation exchange membrane was pre-treated subsequently in 30% H_2O_2, deionized water, 0.5 M H_2SO_4, and deionized water (for 1 h each) to increase porosity. All electrochemical experiments were carried out in a three-electrode cell arrangement that consists of a working electrode, the reference electrode, and the cathode counter electrode. To measure the anode, cathode, membrane and cell potential, both anode and cathode compartments were equipped with an Ag/AgCl (3M KCl, +0.205 V vs NHE) reference electrode. A schematic overview of the experimental setup is presented in Figure 1B.

Startup and MFC operation

Anode chamber was inoculated with the enriched mixed bacterial culture from another MFC run on acetate. The source of inoculums was wastewater, which served as the bacterial inoculum for the formation of a primary electrochemically active biofilm on a potentiostatically positive poised carbon electrode (0.4 V vs. SHE (the standard hydrogen electrode)). Acetate (20 mM) served as the substrate in the growth medium, whose pH was adjusted to 6.8 with 20 mM phosphate buffer solution at pH 7. The bacterial growth medium solution contained following chemicals (per liter): 10 mL/L of a macronutrient solution containing 28 g/L NH_4Cl, 10 g/L $MgSO_4 \cdot 7H_2O$, and 0.57 g/L $CaCl_2 \cdot 2H_2O$; 2 mL/L of micronutrient solution containing 2 g/L $FeCl_2 \cdot 4H_2O$, 1 g/L $CoCl_2 \cdot 6H_2O$, 0.5 g/L $MnCl_2 \cdot 4H_2O$, 0.05 g/L $ZnCl_2$, 0.05 g/L H_3BO_3, 0.04 $CuCl_2.2H_2O$, 0.07 g/L $(NH_4)6Mo7O_{24} \cdot 5H_2O$, 1 g/L $NiCl_2 \cdot 6H_2O$, 0.16 g/L $Na_2SeO_3 \cdot 5H_2O$, and 2 mL/L 37% HCl; and 2 mL/L of a vitamin solution as reported previously by Ter Heijne *et al.*(2008) [23]. In order to ensure anaerobic conditions, the substrate and buffer solutions were purged with nitrogen for 30 min before use. The anolyte and catholyte (volume 550 mL) were continuously recirculated at a rate of 100 mL/min using a peristaltic pump. MFC was

operated in batch mode at the temperature of (27 ± 2ºC) under anaerobic conditions. During a feeding event, the anode chamber was purged with N_2 gas for 30 min to create the anaerobic microenvironment in the cell.

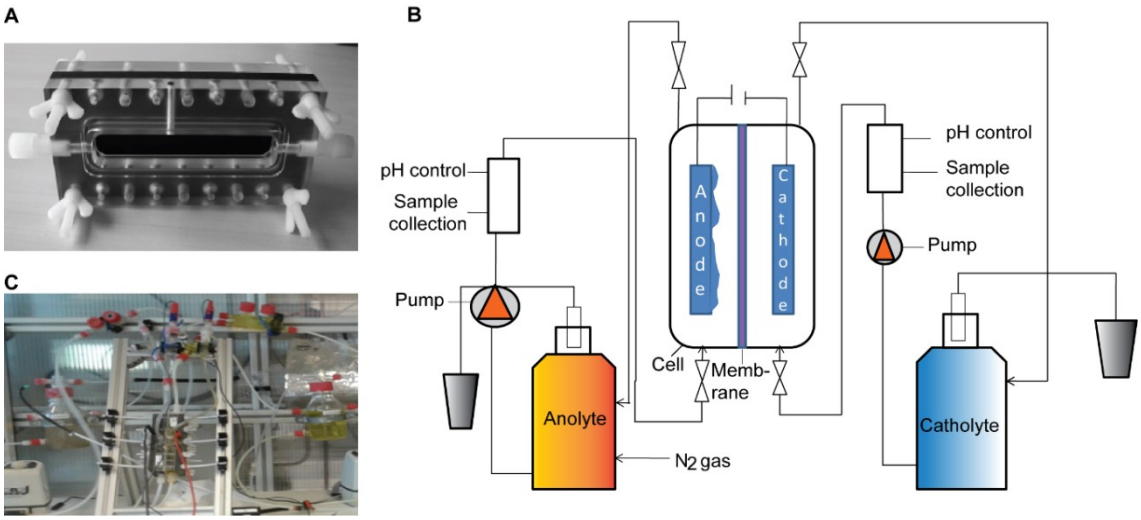

Figure 1. (A) MFC design: the assembly of flow channel, carbon felt electrode, and support plate of one side of the MFC; (B) Schematic of MFC operation to produce bioelectricity; (C) Photograph of the experimental setup.

The MFC was started with an external load of 16 kΩ and a 0.020 M phosphate buffer at pH 7 in the cathode, and air was continuously circulated through the catholyte. Firstly, the system was stabilized overnight to reach a steady state. Four resistors with a range of 0–16 kΩ were used, and thereupon potential was measured two times a day with constant interval using a Keithley 2700 multimeter (Keithley Instruments, Cleveland, OH, USA). Polarization and power density curves were obtained by varying the external resistance applied to the circuit. Here, all electrode potentials were given as vs Ag/AgCl (3M KCl, + 0.205 V vs NHE (the normal hydrogen electrode)) and all the current density values were normalized to the geometric surface area.

After 25th day of operation, the catholyte was replaced with a Fe (III) $[CN]_6^{3-}$ solution (0.050M) in 0.020M buffer (pH 7) for a fast cathode reaction (reduction of Fe(III)$[CN]_6^{3-}$ to Fe(II)$[CN]_6^{4-}$). In this case, the MFC was also operated at three different resistances with first R = 16 kΩ during the first 8 days, second R = 2 & 0.5 kΩ during the next 5 days, and third R=250 Ω during the last 12 days. After reaching stable performance, power output was monitored by measuring voltage using an external resistor (250 Ω) connected across the electrodes.

To characterize pH effects on the MFC performance, media with pHs ranging from 4.0 to 10 at 0.5 pH unit increments were created with 5 M solutions of HCl or NaOH.

Analysis

Cell voltage across an external resistor was recorded using a multimeter. Polarization curves were obtained by varying the external resistance applied to the circuit (in a decreasing order) and using the average voltage obtained after stabilization (2 times in a day). Current density was calculated using I = V/R, where I (mA/m^2) is the current, V (mV) is the measured voltage, and R (Ω) is the applied resistance, and A (m^2) is the

geometric surface area of the anode electrode. Power densities (mWm^{-2}) were calculated using P= IV, and normalized by the projected anode surface area [5].

Coulombic efficiency was calculated as CE (%) = (C_{Ex}/C_{Th}) × 100, where C_{Ex} is the total Coulombs calculated by integrating the current over time, C_{Th} is the theoretical number of Coulombs available from the oxidation of acetate calculated as, C_{Th} = FbMv, F is the Faraday's constant (96,485 C/ mole, b is the number of moles of electrons available per mole of substrate (8 mol e^-/ mol acetate), M is the acetate concentration ($molL^{-1}$), and v is the volume of liquid in the anode chamber (L) [5].

The energy losses of MFC were measured in three parts, which were anode, cathode, and membrane losses. These energy losses therefore led to the internal resistance of the system. Internal resistance can be split into partial internal resistances, for instance, anodic resistance, cathodic resistance, and membrane resistance. Anodic and cathodic resistances were calculated as overpotential divided by current density.

Anodic resistance calculated according to R_{an}= (E_{an}-$E°_{an}$)/I, where, R_{an} = anodic resistance ($\Omega.m^2$), E^0_{an}= Theoretical anode potential (V), E_{an} = measured anode potential at certain external load (V), I = current density (A/m^2). Assumed that theoretical anode potential is open circuit potential (at zero current). Cathodic resistance, R_{cat} = ($E°_{cat}$-E_{cat})/I, where R_{cat} = cathodic resistance ($\Omega.m^2$), E^0_{cat} = theoretical cathode potential (V), E_{cat} = measured cathode potential, I = current density (A/m^2) [24].

Results and Discussion

Reactor performance

Following inoculation of the anode, the operation of MFC were started with a 0.020 M phosphate buffer at pH 7 in the cathode, in which oxygen was circulated continuously for reduction reaction ($O_2 + 4H^+ + 4e^- \rightarrow 2H_2O$). Firstly, to obtain polarization and power density curve, MFC was started with a 16 kΩ external resistor, and stabilized overnight to reach a steady state. Afterward, the polarization test was performed (every day two times) to evaluate the development of activity of electrochemically active microorganisms in time that means the performance of the bioanode. Higher current density accompanying the lowest anode overpotential is indicating best performance of MFC [5]. During the polarization test, the current density was extracted from the maximum current densities of the batch experiments. At the beginning of the experiment, negligible current was observed, and this is due to the lack of biocatalysts at the electrode surface. About 12 day after the initial inoculation, the current rose significantly, indicating the formation of an electrochemically active biofilm. The biocatalytic current density and the power density reached the maximum values of about 51.5 mAm^{-2} and 11.6 mWm^{-2}, respectively, on day 25^{th} after inoculation at 250 Ω for operation.

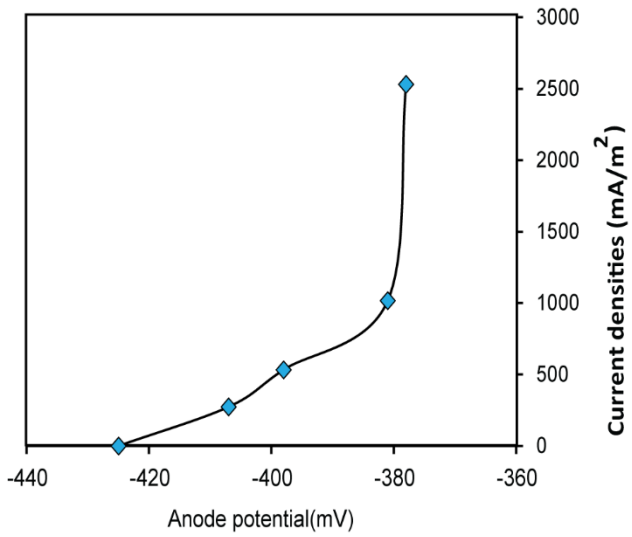

Figure 2. Polarization test gave insight into the performance of a bio-anode at operation 250 Ω in time using potassium hexacynonoferrate(III) reduction at the cathode on 25th day.

To investigate the effect of the catholyte on the performance of MFC (in terms of power generation), the catholyte was replaced by Potassium hexacyanoferrate(III) (Fe (III) $[CN]_6^{3-}$ solution, 0.050M). In this case, the MFC was started with freshly inoculated anolyte. With the cathodic reaction of potassium hexacyanoferrate(III), a higher current density as well as a higher power density was observed (current density 2.5 Am^{-2}, power density 1410 mWm^{-2}) at the anode potential of -378 mV on day 25 (see in Figure 2), while the MFC was operated at 250 Ω. From the polarization test, Figure 3 is depicted an overview of obtained cell voltage, cathode potential, and anode potential during maximum power generation.

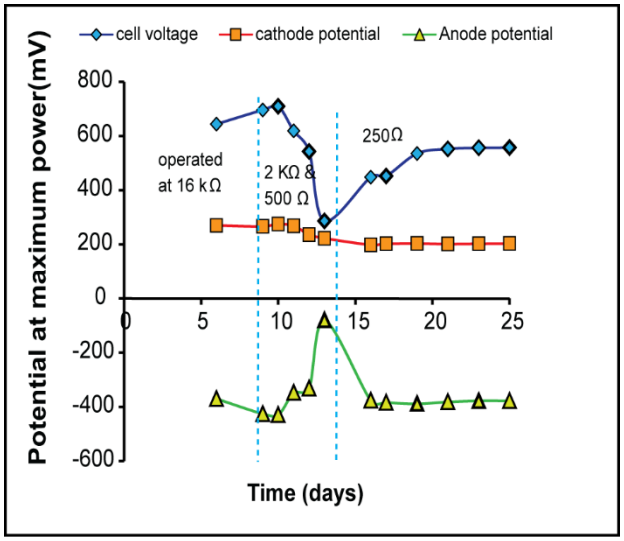

Figure 3. Cell voltage, cathode potential, and anode potential were recorded from the polarization test while maximum power produced by MFC, using Hexacyanoferrate (III) as the catholyte. First 8 days, the cell was operated with a 16 kΩ external resistor, next 9-13 days, cell was operated at 2 KΩ & 500 Ω and last 14-25 days, cell was operated at 250 Ω.

Higher current density as well as higher power density was obtained for Potassium hexacyanoferrate(III) reduction than the oxygen reduction at the cathode. This lower current density for oxygen reduction at the cathode could be the results of (i) oxygen diffusion through the membrane from cathode to anode leading to a parasitic reaction at the anodic compartment, therefore limiting the number of electrons available for electricity production. The parasitic side reaction that leads to the formation of mixed potential, may substantially lower the anode potential and reduce the cell voltage as well as current density and power density. Furthermore, this side reaction may not only reduce the cell voltage but also reduce the columbic efficiency of the electrode reaction [25]. (ii) Competing reduction reaction may be occurred during oxygen reduction at the cathode. (for instance, not only formation of water, but often considerable extent of hydrogen peroxide formation). This competing reaction can lead to the formation of mixed cathode potential (reduce cell voltage), which limits the overall performance of MFC. (iii) Due to limited diffusion of oxygen in the electrode surface, the higher cathodic partial internal resistance produced (3050 $m\Omega.m^2$ at maximum current density 51.5 mAm^{-2}, on day 25) can limit the performance of the cell.

Improvisation of the MFC performance by operating at a lower external resistor was revealed through the polarization test. Figure 4 depicts that the MFC operation at a lower external resistor caused higher current densities. The potential difference in the anode (between the electron donor (acetate) and the electron acceptor (the anode) became larger due to lower resistance of the MFC that helped the electrochemically microorganisms to attain more energy from the substrate. This energy gaining for the growth of microorganisms in turn helped produce higher current that reflected the maximum bioelectrocatalytic activity of the biofilm [23].

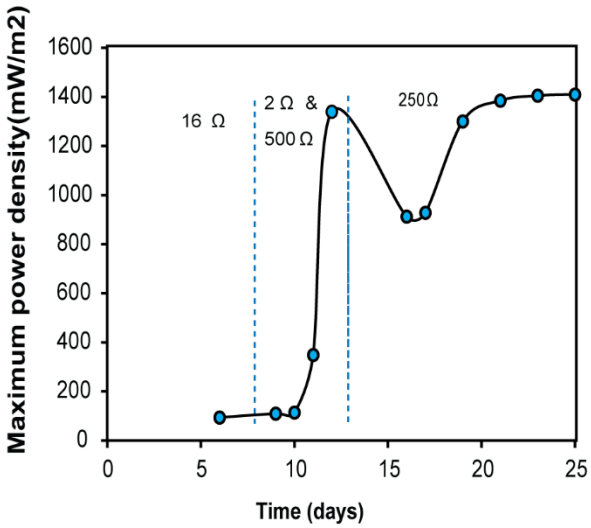

Figure 4. Maximum power evolution was recorded from days 6th to 25th during cell operated at different external loads 16 KΩ, 2 KΩ, 500 Ω, and 250 Ω. (Hexacyanoferrate(III) used as a catholyte).

To determine the performance of a microbial fuel cell, the internal resistance (R_{int}) has been recognized as an important factor [16]. Thus, the internal resistance profile was observed over the operation period in order to envisage the changes in performance of MFC, while hexacyanoferrate (III) was reduced at the cathode (hexacyanoferrate (III) used

as a catholyte). Figure 5 depicts the anode and cathode resistances over the period of operation.

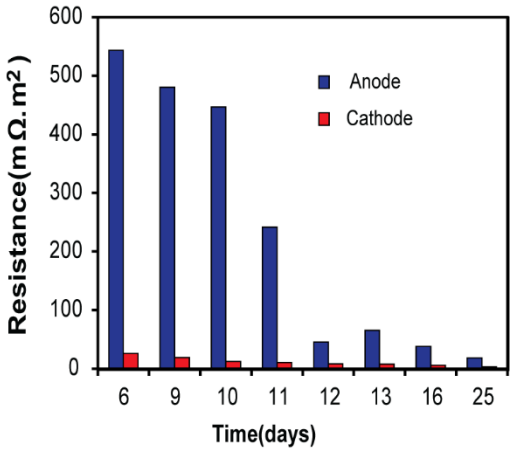

Figure 5. Internal resistances profile of anode and cathode over the period of MFC operation.

The results revealed that the anode resistance declined from 543.9 mΩ.m^2 to 18.5 mΩ.m^2 (from day 6 to 25), indicating the enhancement in activity of the electroactive biofilm. Cathode resistance also decreased from 25.9 mΩ.m^2 to 3.1 mΩ.m^2 (from day 6 to 25). As both anode and cathode resistances decreased with time, it indicted that the performance of MFC increased with time. The total cell resistance (sum of the anode, cathode and membrane internal resistances) decreased from 582.7 mΩ.m^2 to 27.48 mΩ.m^2 (from 6 day to 25 day). At the maximum performance on the day 25th, the anode, the cathode, and the membrane contributed to 67%, 11%, and 20% of the total resistance, respectively.

When MFC was operated with potassium hexacyanoferrate(III) for cathodic reaction, the Coulombic efficiencies (CE %) 22.70 % of MFC was observed at the stable phase of fuel cell operation.

Effect of pH on MFC performance

Physiologically permissive medium is crucial for the growth of a viable biocatalyst on an electrode. To enhance the MFC operation and performance, an improved understanding of the bioanode process as a function of medium pH conditions is of crucial importance. Therefore, MFC performance was examined by using media with pHs ranging from 4.0 to 10 at 0.5 pH unit increments. MFC performance was characterized based on current densities as well as power densities produced using the polarization test.

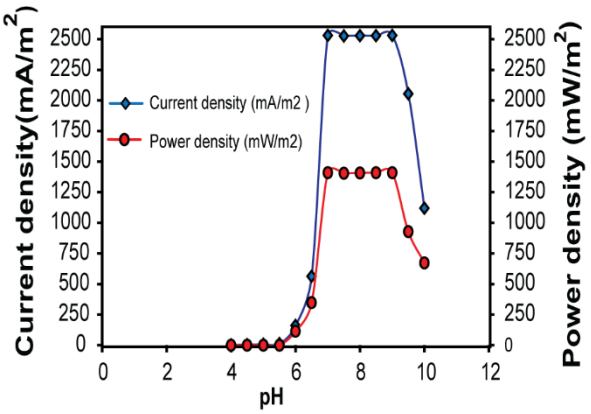

Figure 6. Obtained current density and power density correspond to cell operated with media of pHs ranging 4 to 10. The maximum current density and power density were extracted from 25 day when MFC operated with 250 Ω external load.

Figure 6 shows that MFC performance was enhanced as pH became neutral, and this result is consistent with a previous study [26]. However, at low pH condition, the current densities and power densities decreased. The acidification of the anode biofilm affected current generation, because microbial activity is inhibited in low pH [27]. The produced current densities and power densities were remained almost steady from pH 7 to 9. In alkaline medium and high buffer concentration, bioanode performance was enhanced by increasing flux of proton shuttles out of the anode biofilm [28]. However, the maximum power density (P_{max}) decreased at pH 9.5, showing that neutral pH was the optimum pH for attaining the highest power density in this system.

Conclusion

In this study, we have shown that the bioelectricity yield at neutral pH condition from microbial fuel cell (MFC), where untreated carbon felt was used as both the anode and the cathode, and the anolyte was inoculated with mixed culture. The performance of MFC was enhanced by replacing continuous air cathode with potassium hexacyanoferrate (III). Potassium hexacyanoferrate (III) reduced at cathode that increased current density by addressing the limited diffusion of the substrate into the electrode surface. The increase in power density to 1410 mWm^{-2} resulted in the improved performance of the system at higher current densities (51.5 mAm^{-2} to 2500 mAm^{-2}). Power generation using MFC with low cost electrodes and mixed culture was considered as cost-effective and environmentally sustainable process which will also provide a great potentiality for other applications like handy power supplies for remote sensors using native fuels.

Declarations

Availability of data and materials

Data and materials related to this work are available upon request.

Authors' contribution

All authors contribute equally during the research study and preparation of the manuscript. All authors read and approved the final manuscript.

Competing interests
The authors declare that they have no competing interests.

Consent for publication
All authors approve the manuscript for publication.

REFERENCES

[1] Bond, D. R., Holmes, D. E., Tender, L. M., and Lovley, D. R., 2002. Electrode-reducing microorganisms that harvest energy from marine sediments. *Science*, *295*(5554): 483-485. DOI: 10.1126/science.1066771

[2] Rodrigo, M. A., Canizares, P., Lobato, J., Paz, R., Sáez, C., and Linares, J. J., 2007. Production of electricity from the treatment of urban waste water using a microbial fuel cell. *J. Power Sources*, *169*(1): 198-204. DOI:10.1016/j.jpowsour.2007.01.054

[3] Lovley, D. R., 2006. Bug juice: harvesting electricity with microorganisms. *Nat. Rev. Microbiol.*, *4*(7): 497-508. DOI:10.1038/nrmicro1442

[4] Davis, F., and Higson, S. P., 2007. Biofuel cells—recent advances and applications. *Biosens. Bioelectron.*, *22*(7): 1224-1235. DOI:10.1016/j.bios.2006.04.029

[5] Logan, B. E., Hamelers, B., Rozendal, R., Schröder, U., Keller, J., Freguia, S., Aelterman, P., Verstraete, W., and Rabaey, K., 2006. Microbial fuel cells: methodology and technology. *Environ. Sci. Technol.*, *40*(17): 5181-5192. DOI**:** 10.1021/es0605016

[6] Lovley, D. R., 2006. Microbial fuel cells: novel microbial physiologies and engineering approaches. *Curr. Opin. Biotechnol.*, *17*(3): 327-332. DOI: 10.1016/j.copbio.2006.04.006

[7] Schröder, U., 2007. Anodic electron transfer mechanisms in microbial fuel cells and their energy efficiency. *Phys. Chem. Chem. Phys.*, *9*(21): 2619-2629. DOI: 10.1039/b703627m

[8] Freguia S, Rabaey K, Yuan Z, and Keller J., 2008. Sequential anode–cathode configuration improves cathodic oxygen reduction and effluent quality of microbial fuel cells. *Water Res.*, 42(6):1387-96. DOI:10.1016/j.watres.2007.10.007

[9] Logan, B. E., 2009. Exoelectrogenic bacteria that power microbial fuel cells. *Nat. Rev. Microbiol.*, *7*(5): 375-381. DOI:10.1038/nrmicro2113

[10] Logan, B. E., and Regan, J. M., 2006. Electricity-producing bacterial communities in microbial fuel cells. *TRENDS Microbiol.*, *14*(12): 512-518. DOI: 10.1016/j.tim.2006.10.003

[11] Venkata Mohan S, Saravanan R, Veera Raghuvulu S, Mohanakrishna G, Sarma PN.,2008.Bioelectricity production from wastewater treatment in dual chambered microbial fuel cell (MFC) using selectively enriched mixed microflora. *Eff. Catholyte Biores. Technol*., *99*: 596–603. DOI:10.1016/j.biortech.2006.12.026

[12] Maness, P. C., Huang, J., Smolinski, S., Tek, V., and Vanzin, G., 2005. Energy generation from the CO oxidation-hydrogen production pathway in *Rubrivivax gelatinosus*. *Appl. Environ. Microbiol.*, *71*(6): 2870-2874. DOI: 10.1128/AEM.71.6.2870-2874.2005

[13] Venkata Mohan S, Veer Raghuvulu S, Sarma PN.,2008. Biochemical evaluation of bioelectricity production process from anaerobic wastewater treatment in a single chambered microbial fuel cell (MFC) employing glass wool membrane. *Biosens Bioelectron., 23*:1326–32. DOI:10.1016/j.bios.2007.11.016

[14] Rezaei, F., Xing, D., Wagner, R., Regan, J. M., Richard, T. L., and Logan, B. E., 2009. Simultaneous cellulose degradation and electricity production by Enterobacter cloacae in a microbial fuel cell. *Appl. Environ. Microbiol.*, *75*(11): 3673-3678. DOI:10.1128/AEM.02600-08

[15] Zuo, Y., Xing, D., Regan, J. M., and Logan, B. E., 2008. Isolation of the exoelectrogenic bacterium Ochrobactrum anthropi YZ-1 by using a U-tube microbial fuel cell. *Appl. Environ. Microbiol.*, *74*(10): 3130-3137. DOI: 10.1128/AEM.02732-07

[16] He, Z., Minteer, S. D., & Angenent, L. T., 2005. Electricity generation from artificial wastewater using an upflow microbial fuel cell. *Environ. Sci. Technol.*, *39*(14): 5262-5267. DOI: 10.1021/es0502876

[17] Min, B., and Logan, B. E., 2004. Continuous electricity generation from domestic wastewater and organic substrates in a flat plate microbial fuel cell. *Environ. Sci. Technol.*, *38*(21): 5809-5814. DOI: 10.1021/es0491026

[18] Ter Heijne, A., Hamelers, H. V., De Wilde, V., Rozendal, R. A., and Buisman, C. J., 2006. A bipolar membrane combined with ferric iron reduction as an efficient cathode system in microbial fuel cells. *Environ. Sci. Technol.*, *40*(17): 5200-5205. DOI: 10.1021/es0608545

[19] Kim, J. R., Min, B., and Logan, B. E., 2005. Evaluation of procedures to acclimate a microbial fuel cell for electricity production. *Appl. Microbiol. Biotechnol.*, *68*(1): 23-30. DOI: 10.1007/s00253-004-1845-6

[20] Park, D. H., & Zeikus, J. G., 2003. Improved fuel cell and electrode designs for producing electricity from microbial degradation. *Biotechnol. Bioeng.*, *81*(3): 348-355. DOI: 10.1002/bit.10501

[21] Lowy, D. A., Tender, L. M., Zeikus, J. G., Park, D. H., and Lovley, D. R., 2006. Harvesting energy from the marine sediment–water interface II: kinetic activity of anode materials. *Biosens. Bioelectron.*, *21*(11): 2058-2063. DOI: 10.1016/j.bios.2006.01.033

[22] Cheng, S., and Logan, B. E., 2007. Ammonia treatment of carbon cloth anodes to enhance power generation of microbial fuel cells. *Electrochem. Commun.*, *9*(3): 492-496. DOI:10.1016/j.elecom.2006.10.023

[23] Ter Heijne, A., Hamelers, H. V., Saakes, M., and Buisman, C. J., 2008. Performance of non-porous graphite and titanium-based anodes in microbial fuel cells. *Electrochim. Acta*, *53*(18): 5697-5703. DOI:10.1016/j.electacta.2008.03.032

[24] Helder, M., Strik, D. P., Hamelers, H. V., and Buisman, C. J., 2012. The flat-plate plant-microbial fuel cell: the effect of a new design on internal resistances. *Biotechnol. Biofuels*, *5*(1): 70. DOI: 10.1186/1754-6834-5-70

[25] Harnisch, F., and Schröder, U., 2010. From MFC to MXC: chemical and biological cathodes and their potential for microbial bioelectrochemical systems. *Chem.l Soc. Rev.*, *39*(11): 4433-4448. DOI: 10.1039/c003068f

[26] He, Z., Huang, Y., Manohar, A. K., and Mansfeld, F., 2008. Effect of electrolyte pH on the rate of the anodic and cathodic reactions in an air-cathode microbial fuel cell. *Bioelectrochemistry*, *74*(1): 78-82. doi:10.1016/j.bioelechem.2008.07.007

[27] Franks, A. E., Nevin, K. P., Jia, H., Izallalen, M., Woodard, T. L., and Lovley, D. R., 2009. Novel strategy for three-dimensional real-time imaging of microbial fuel cell communities: monitoring the inhibitory effects of proton accumulation within the anode biofilm. *Energy Environ. Sci.*, *2*(1): 113-119. DOI: 10.1039/B816445B

[28] Fan, Y., Hu, H., & Liu, H., 2007. Sustainable power generation in microbial fuel cells using bicarbonate buffer and proton transfer mechanisms. *Environ. Sci. Technol.*, *41*(23): 8154-8158. DOI: 10.1021/es071739c

Trends in Renewable Energy
OPEN ACCESS ISSN: 2376-2144
Peer-Reviewed Review Article futureenergysp.com/index.php/tre

Techno-Economic Analysis of Biodiesel Production from Microalgae: A Review

Junying Chen[1,2], Qingliang Li[1,2], Chun Chang[1,2], Jing Bai[1,2*], Liping Liu[1,2], Shuqi Fang[1,2], Hongliang Li[1,2]

1: School of Chemical Engineering and Energy, Zhengzhou University, China;
2: Engineering Laboratory of Henan Province for Biorefinery Technology and Equipment, Zhengzhou, China

Received June 8, 2017; Accepted September 21, 2017; Published September 22, 2017

The development of the microalgae-based biodiesel technology has become a hot research topic in the bioenergy field in recent years. Presently, the technical possibility of the conversion of microalgae to biodiesel has been confirmed at the laboratory scale. The fundamental issues impeding the industrialization of microalgae-based biodiesel include the high cost of production and the lack of research on the scaling-up technology. In this paper, the technical challenges and economic aspects of biodiesel production from microalgae were analyzed. It was found that the production cost of microalgae-based biodiesel mainly come from three processes: microalgae cultivation, harvest, and lipid extraction, among which microalgae cultivation represented the highest cost. Finally, the prospect of the industrialization of the microalgae-based biodiesel was proposed.

Keywords: Microalgae; Biodiesel; Technical challenges; Economic Analysis; Cultivation; Harvest; Lipid extraction

1. Introduction

Environmental pollution and energy shortages have become important issues that restrict the sustainable development of the world economy. Biodiesel as a green and renewable energy has received more attention. Biodiesel consists of long chain fatty acid methyl esters or ethyl esters, which are produced by esterification or transesterification reaction with animal fats and vegetable oils [1]. Biodiesel is free of sulfur and aromatics components, and used as an additive of diesel fuels that can significantly reduce the sulfur oxides, hydrocarbons, nitrogen oxides, and other pollutant emissions [2]. As a new type of renewable energy, a major problem restricting its development is the serious shortage of feedstock. Currently, biodiesel made from vegetable oils and animal fats can fulfil about 3% of the required diesel fuel, and the increasing use of these feedstock for biodiesel production may result in world food supply problems [3].

Microalgae is the most widely distributed and the largest species in nature, representing a large quantity of biomass resource. Compared to other biomass, microalgae have the advantages of high photosynthetic efficiency, short growth period, high biomass yield, no need for arable land, high efficiency of carbon fixation, high oil content, and environmental friendly resource. It is considered as one of the ideal feedstock for biodiesel production [4].

*Corresponding author: baijing8279@163.com

Tr Ren Energy, 2017, Vol.3 No.2 141-152. doi: 10.17737/tre.2017.3.2.0035

2. Production Process of Biodiesel from Microalgae

The production process of microalgae-based biodiesel mainly includes four steps, namely microalgae culture, harvest, oil extraction, and esterification as shown in Figure 1. There are several different process routes to choose for each step in this production process. In order to establish an industrial technology route, it is necessary to study the key technical issues in each step. The existing production processes of microalgae-based biodiesel require high cost and show low production efficiency. Some of the bottlenecks have seriously restricted the development of industrialization. Currently, the microalgae industry is small in scale, and research and development are required.

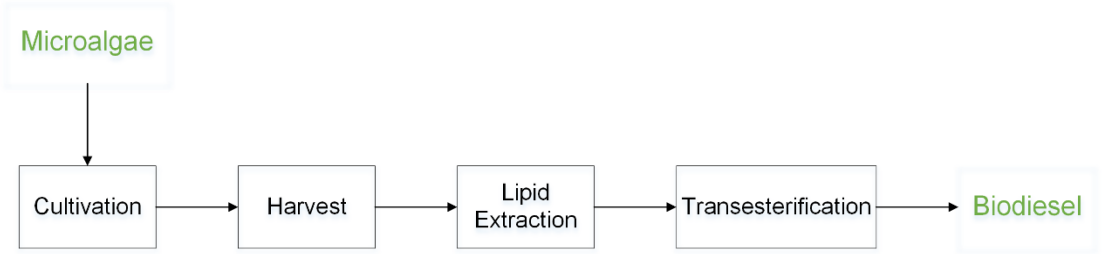

Figure 1. Production process of biodiesel using microalgae

2.1 Microalgae cultivation

Microalgae such as *Prymnesiophytes* (Class *Prymnesiophyceae*), *Eustigmatophytes* (Class *Eustigmatophyceae*), diatoms (Class *Bacillariophyceae*), green algae (Class *Chlorophyceae*), goldenbrown algae (Class *Chrysophyceae*) and blue-green algae (Class *Cyanophyceae*) have shown the potential to accumulate high levels of polyunsaturated fatty acids (also known as microalgal lipids or microalgal oils). Table 1 summarizes the lipid content and the biomass yield of some typical microalgal species.

Microalgal lipids are similar to vegetable oils, which can be used as a substitute of vegetable oils for biodiesel production or even cooking [5]. At present, there are a lot of studies on utilization of microalgal lipids, and reported microalgal species include *Chlorella* sp., *Isochrysis galbana*, diatoms, and *Scenedesmus.* These microalgae perform photosynthesis using water, carbon dioxide, and simple inorganic elements with the sunlight as the energy source. The resulting lipids can be converted into biodiesel (fatty acid methyl ester or ethyl ester) via esterification. Microalgal residues after lipid extraction can be used for production of animal feed, organic fertilizer, and methane.

The amount of lipids accumulated in microalgal cells is closely related to the cultivation conditions. Adequate carbon sources and other nutrient deficiencies are an induction factor in production of a higher lipid content. Generally, microbial production of lipids can be divided into two stages, namely, cell proliferation and lipid accumulation period. Different carbon-nitrogen ratios can be applied for these two stages. The role of nitrogen source is to promote cell growth. The low carbon and nitrogen ratio during the first stage is favorable for biomass production, while lipid-producing stage requires a high carbon to nitrogen ratio [6]. The effect of temperature on the accumulation of lipids is various among different microalgal species. The light intensity is one of the important factors that affect the growth and biochemical composition of microalgae. In general, a low light intensity can induce synthesis of polar lipids, while a high light intensity can lead to accumulation of neutral lipids [7].

The way that was used to grow microalgae is another key factor affecting the rate of microalgal biomass synthesis. The growth modes of microalgae include autotrophic, heterotrophic, and mixotrophic. Autotrophic is the most common way of microalgal growth. Different microalgal species have very different lipid contents during autotrophition. Generally, the lipid content of algal cells can be improved by reducing either nitrogen source or other nutrient elements in the culture medium. However, due to the need of adequate light, the cell density of autotrophic algae is relatively low. The cell density is even lower under nutrient deficiencies and nutritional stress, which greatly reduces the efficiency of microalgae production and make harvest more difficult [8].

Heterotrophic cultivation of microalgae is generally carried out using traditional fermentation equipment, in which microalgae are not affected by environmental conditions and grow fast without light. This method can shorten the culture cycle, and reduce the cost of harvest. However, some scholars believe that heterotrophic culture of microalgae will discharge CO_2, instead of fixing it [9]. The need of additional organic carbon sources rises the cultivation cost. The autotrophic feature of microalgae is lost, but the ability of lipid production still cannot compete with oleaginous microorganisms.

Mixotrophic grown microalgae obtain energy mainly via photosynthesis, but the external organic carbons and CO_2 are also necessary. This culture condition reduces the release of CO_2, but the microalgae lipid content and cell density are not significantly improved. So, this method is not extensively applied.

Table 1. Lipid content and yield of some microalgal species [8]

Microalgal species	Growth condition	Lipid content (wt% of cell dry weight)	Growth rate (g/(L·d))	Lipid production rate (mg/(L·d))
Chlorella protothecoides CCAP 211/8D	Autotrophic	11.0~23.0	0.002~0.02	0.2~5.4
Chlorella protothecoides	Heterotrophic	50.3~57.8	2.2~7.4	1209.6~3701.1
Chlorella protothecoides	Mixotrophic	58.4	23.9	11800
Chlorella vulgaris #259	Autotrophic	33.0~38.0	0.01	4.0
Chlorella vulgaris #259	Mixotrophic	21.0~34.0	0.09~0.25	22.0~54.0
Dunaliella tertiolecta ATCC 30929	Autotrophic	60.6~67.8	0.10	60.6~69.8
Isochrysis sp. F&M-M37	Autotrophic	27.4	0.14	37.8
Nannochloropsis oculata NCTU-3	Autotrophic	22.7~29,7	0.37~0.48	84.0~142.0
Pavlova lutheri CS 182	Autotrophic	35.5	0.14	50.2
Scenedesmus sp. DM	Autotrophic	21.1	0.26	53.9

The autotrophic culture system for microalgae can be divided into two categories: outdoor open pond and closed photobioreactor. Table 2 summarizes the properties of open ponds and enclosed photobioreactors. Open ponds may adopt one of the raceway type, round pool, and slope type designs. Closed photobioreactor designs can be columns, tubes, plates, and some other special types [10]. The raceway pond is the most important culture system for commercial cultivation of microalgae. The system is generally a shallow pool with 15-30 cm depth and natural light as the light source and the heat source. The rotation of the impeller(s) mixes the culture medium, prevents algae precipitation, and improves the light utilization. Air or CO_2 gas may be pumped into the system via bubbling or airlift stirring. The raceway pond can be covered with a transparent film that can prevent pollution and reduce water evaporation.

Table 2. Properties of open ponds and enclosed photobioreactors [10]

Cultivation system	Advantages	Disadvantages
Open pond	Low construction cost, low operation cost, ease to clean, mature technology, ease to scale-up	Need large area, ease to be contaminated, hardly to grow monoculture, low biomass yield, water evaporation, difficulty of harvesting, affected by environmental conditions, hardly to supply extra CO_2.
Closed photobioreactor	Grow monoculture, low possibility of contamination, high biomass yield, ease to harvest, low water evaporation, ease to control, hardly affected by the environment	High construction cost and operation cost, forming biofilm, hardly to clean, need enhanced mass transfer, heat transfer and light, technologies under development

2.2 Harvest of Microalgae

Microalgae harvest from the culture broth has been a bottleneck in the industrial scale microalgae production. Individual microalgal cells are small (1-30 μm diameter). The cell surface often possesses with hydroxyl, carboxyl, amino, mercapto, and phosphate groups and shows a negative charge [11]. It is possible to form a stable dispersion system in the culture medium, and the biomass concentration in the culture medium is very low (usually 0.5 to 5.0 g/L), so that the harvest of microalgae is difficult. The cost of harvesting microalgae accounts for 20% to 30% of the cost of microalgae farming that includes cultivation and harvesting [12]. Therefore, there is an urgent need to develop high efficiency and low-cost harvesting methods.

Due to the special nature of microalgae and its culture medium, the traditional solid-liquid separation technology cannot be directly applied for microalgae harvesting. Generally, microalgae are first physically or chemically treated, and then separated [13]. The harvesting methods include sedimentation, flotation, dissolved air floatation (DAF), filtration, and centrifugation. Sedimentation and flotation are the preferred harvesting methods for open large ponds due to the low cost [14]. The flotation method uses a flocculant such as Fe^{3+}, $Al_2(SO_4)_3$ or a cationic polymer. The flotation method is only applicable to few species like *Chlorella* and *Scenedesmus*, and it must combine with other methods to work effectively. Sedimentation is suitable for microalgae easily settled. Some microalgae can be precipitated by changing pH. Meanwhile, the DAF method can easily, safely, and efficiently concentrate the microalgae cells via adjusting the pH value, increasing the reflux ratio, and prolonging the dissolved gas time and contact residence time [15]. Centrifugation and ultrafiltration are suitable for the harvest of microalgae from photobioreactors, in which microalgae can usually achieve higher cell density. Centrifugation is a fast harvesting method, but it is also more energy intensive and only applicable when extracting high-value products from microalgae. Ultrafiltration is not suitable for the large-scale harvest due to the high cost of the membrane. The development of low cost membrane materials can also serve as an effective way to reduce the cost of microalgae biodiesel.

2.3 Extraction of Microalgal Lipids

Microalgal lipids are mainly distributed in the forms of triglycerides or fatty acids in the cells. The extraction of intracellular lipid components is also an important part of microalgae biodiesel production process. The extraction technologies of microalgal lipids

include mechanical crushing, organic solvent extraction, water enzymatic, supercritical fluid extraction, thermal cracking, etc. These methods require microalgae as a dry powder [16].

Cell density of microalgae in the large-scale culture is generally less than 10 g/L. Even after solid-liquid separation (such as centrifugation, flocculation, flotation, membrane filtration, etc.), the microalgae slurry still has a high water content of 95.5% to 67%. The drying methods for microalgae slurry include sun drying, drum drying, spray drying, fluidized bed drying, freeze drying, and refractance window dehydration technology. According to the life cycle analysis (LCA), the energy output of the products produced by using dry microalgae is less than the energy input [17]. In order to avoid the energy intensive drying process, the development of conversion technologies that use wet algae as raw material has become an important research direction.

Mechanical crushing is the simplest method for microalgal lipid extraction. With the assistance of the high osmotic shock and ultrasonic assisted technologies, the cell rupture and intracellular release of substances can be accelerated. But these technologies are energy consumption, and different extrusion methods must be selected according to the specific physical characteristics of microalgal species.

Solvent extraction method commonly uses chemical solvents such as benzene, ether, and n-hexane, as well as mixing co-solvent extraction. Mixing co-solvent extraction refers to mixing a polar solvent and a non-polar solvent to form a single-phase system to extract microalgal lipids. At present, the methanol-chloroform system is the most commonly used method for extraction of microalgal lipids. This methanol-chloroform system is based on the principle of "similar compatibility". Microalgae are fully contacted with the methanol-chloroform mixed solvent. The polar solvent of methanol binds to the polar lipids of the cell membrane, and thereby destroying the hydrogen bonds and electrostatic interactions between the lipid and the protein molecules; while the non-polar solvent of chloroform diffuses into the cell and dissolves the intracellular hydrophobic neutral lipids. After extraction, water is added to the system. Methanol is dissolved in the water phase, and separated from the lipid-containing chloroform phase. Crude microalgal lipids can be obtained after evaporation of chloroform [16].

Water enzymatic method is the use of enzymes to decompose the cell wall and release microalgal lipids. The major limitation of this method is the high cost of enzymes.

Supercritical carbon dioxide extraction is another potential extraction method of microalgal lipids. Supercritical carbon dioxide possesses the characteristics of both liquid and gas, which can greatly speed up the extraction process of lipids with a high oil recovery rate. But the expensive equipment and operating conditions make it difficult for industrialization.

2.4 Production of biodiesel

Biodiesel preparation methods can be categorized as physical and chemical methods. Physical methods include direct mixing and micro-emulsion method, while chemical methods include thermal cracking and transesterification [13]. The most widely used biodiesel preparation method is a chemical method - transesterification, in which methanol reacts with natural lipids that is in the form of triglycerides. The triglycerides are broken into three long-chain fatty acid methyl esters and glycerol, thereby reducing the length of the carbon chain. The viscosity of the oil product (often called biodiesel) is reduced and the fluidity is improved. The biodiesel product meets the requirements of the transportation fuel. Fatty acids that are suitable for producing biodiesel have a chain

length of 16 to 18 carbon, and the majority of high-lipid content microalgae accumulate triglycerides with a fatty acid content falling into this range. The transesterification reaction can reduce the molecular weight of the original lipids by 1/3 and the viscosity by 8 times, improve the volatility, and make the products compatible with diesel.

2.4.1 Biodiesel Production by in-situ Transesterification

During in-situ transesterification, the dried microalgae powder reacts with an alcohol (such as methanol) to produce fatty acid methyl esters in presence of a strong acid catalyst such as HCl and H_2SO_4. In-situ esterification eliminates the need for lipid extraction steps, and effectively simplifies the production process of biodiesel. It is suitable for methyl esterification of fatty acid contents in microalgal biomass with a high oil content. Studies on the in-situ esterification of microalgae showed that the reaction can be done within 1 h at 100°C in a closed vessel, and purification of fatty acid methyl esters can be done simultaneously by adding n-hexane [18]. By mixing the substrate alcohol with a weakly polar solvent such as diethyl ether or toluene, the yield can be improved by changing the polarity of the reaction medium. Alternatively, microalgae can be converted into liquid biodiesel under supercritical methanol transesterification conditions [19].

2.4.2 Biodiesel Production by Hydrocracking

Recently, some researchers in the United States and Europe are exploring the technology for the preparation of microalgae-based diesel by using hydrocracking. The technology is different from the transesterification technology [20]. The final products obtained by transesterification are fatty acid methyl esters – biodiesel, while the hydrocracking technology yields the green diesel (also called renewable diesel) whose composition is identical to that of petrochemical diesel. The green diesel can be mixed with petrochemical diesel in any proportion. The existing hydrocracking technology and equipment in the refinery can be directly used to refine microalgal crude lipids. Because this technology requires less investment and can be industrialized easily, it has been considered as a promising conversion pathway of microalgae.

2.5 Challenges in Production of Biodiesel from Microalgae

The use of microalgae for biodiesel production is still in its infancy, though it has shown many advantages. Currently, the biodiesel production technology for vegetable oil processing is relatively mature. Because microalgal lipids are similar to the vegetable oil, conversion of the microalgal lipids to biodiesel is technically feasible. However, according to the existing microalgae processing technologies, there is still a considerable distance to commercial applications. The bottleneck is the difficulty of obtaining enough microalgal biomass, which results in the high cost of microalgae-based energy products [21]. The main problems include:

(1) Selection of high quality energy microalgae

The lipid content and composition of microalgae are an important factor to determine the yield and quality of biodiesel. The selection of high quality microalgae species satisfying the industrial demand is a necessary condition for the mass production of microalgae-based biodiesel. The growth rate and the final cell density of microalgae are relatively low, and the cultivation process and harvesting costs are high. To solve these problems, mixotrophic or heterotrophic microalgae can be adopted to improve the

oil production rate, and engineering fast-growing lipid-rich microalgal species is necessary [22].

(2) Large-scale, low-cost, high-efficiency cultivation system and cultivation technology

Developing microalgae cultivation systems that can reach a high cell density is one way to improve the economy of harvest. An optimal design of photobioreactors can ensure maximized use of light energy, high growth rate and cell density, reduction of the all over cost, and ease to scale up culture system [13].

(3) Optimizing the microalgae separation process

Separation of microalgae from the culture media may involve mechanical mixing, centrifugal harvesting, drying, etc. These processes require a high energy consumption, and making energy input and output not economical. The dry matter content in the microalgae culture media is usually less than 1 wt%. Concentration and drying steps extend the production cycle of biodiesel, and affect the efficiency of oil extraction [16].

(4) Comprehensive biorefinery of microalgae Production

Lipid-rich microalgae contain a large amount of protein, polysaccharides, pigments, and other nutrients. If these high value-added products and microalgae biodiesel are manufactured at the same time, it is possible to reduce the cost [5].

Industrialization of microalgae-based biodiesel is a project of complex system engineering. Microalgal growth for energy production requires large scale systems. A large amount of waste culture media may cause serious environmental pollution if handled improperly. Therefore, when planning a site for the large-scale microalgae cultivation, combining the treatment of wastewater, waste gas, and solid wastes should be considered. Industrial flue gas containing CO_2 may be used to culture autotrophic microalgae, while carbon-rich or nitrogen-rich agricultural wastes and industrial wastewater may culture heterotrophic microalgae.

3. Economic Analysis of Microalgae Production

3.1 Microalgae Cultivation

As aforementioned, open ponds and photobioreactors are two major systems for microalgae cultivation. Through the technical and economic analysis of these two kinds of cultivation methods, it is found that there is an obvious economy difference between two approaches (Table 3) [23, 24].

Zhang *et al.* [25] studied the life cycle (LCA) of microalgae cultivated in open race way ponds. It was found that microalgae culture is the costliest part of the whole production process. Their assumptions included that the cell concentration of microalgae in the pond was 0.5 kg/m^3; its location was close to the power plant, and the flue gas discharged from the power plant was used to cultivate microalgae; the medium in the pond was continuously stirred to keep the flow rate; and the diesel was used as the fuel for both transport and equipment maintenance. So the calculated parameters for the growth process of microalgae were: the microalgae yield per hm^2 (dry weight) is about 54.8 t, which requires 10 L diesel oil and 148.9 GJ electricity. If taking into account the nutrients consumption (like nitrates, sulfuric acid, salts, and phosphates) during microalgae cultivation, producing 1 t microalgae biomass needs to consume nitrates 349.74 kg, phosphates 52.969 kg, and sulfates 47.526 kg. The fossil energy consumed in the cultivation process of microalgae accounts for 73.8% of the total fossil fuel

consumption, so the comprehensive utilization of energy is related to the energy balance of the whole microalgae-based biodiesel industry.

Table 3. Economic estimates of microalgae culture in open ponds and photobioreactors [23]

Economic assessment	Open ponds	Photobioreactors
Production scale		
Algae productivity	25(g/m^2/day)	1.25(kg/m^3/day)
Algae cell density (g/L)	0.5	4
Lipid yield (dry wt%)	25%	25%
Operating days/yr	330	330
Lipid production (MM gal/yr)	10	10
Biodiesel production (MM gal/yr)	9.3	9.3
Resource assessment		
Net water demand (MM gal/yr)	10,000	3,000
-water evaporated/water blowdown to treatment (gal/gal lipid)	570	250
- water blowdown to treatment/discharge (gal/gal lipid)	430	50
Fresh CO2 demand (ton/yr)	145,000	145,000
Fresh NH3 required for algae growth (ton/yr)	5,100	5,100
Fresh DAP required for algae growth (ton/yr)	4,800	4,800
Power coproduct exported to grid (MM kW h/yr)	80	100
System cost		
Total capital cost (direct + indirect) ($MM)	$390	$990
Net operating cost ($MM/yr)	$37	$55
Total coproduct credits ($MM/yr)	$6	$7

Presently, the comprehensive utilization technologies of energy mainly include the concentrated solar power [26] and the flue gas and wastewater co-utilization (FWC) technology [27]. Concentrated solar power converts the solar energy into heat that is stored in water, oil, sand, or other media. When needed, the stored heat will be used to generate electricity to supply the microalgae culture system, which can minimize the weather effects and provide continuous and stable energy supply. The FWC strategy uses the wastewater to provide N, P, and other nutrients, and industrial flue gas as the CO_2 source for microalgae culture. FWC saves resources and controls the pollution. The types of wastewater include domestic sewage, aquaculture wastewater, fermentation wastewater, papermaking wastewater, and so on.

3.2 Microalgae Harvesting Process

When the density or the lipid content of microalgae reaches a certain concentration, microalgae will be harvested. The cost of harvesting microalgae accounted for 20 to 30 percent of the total production cost. Commonly used harvesting technologies are flocculation, centrifugation, and filtration. The cost and energy consumption of these harvesting techniques are summarized in Table 4.

Membrane filtration often uses modified cellulose as the filter, which is easy to be polluted, though the counter-current operation may improve the efficiency to some extent. Centrifugation is a commonly used method for cell separation, which uses centrifugal separation without introducing other chemical reagents, but requires a high energy cost [28]. Flocculation is an industrial separation technology. This method requires the addition of $AlCl_3$, $FeCl_3$ or chitosan as flocculant to fix microalgae cells into flakes. However, the flocculant is difficult to be removed during the downstream separation

processes. Microbial flocculation is a new method developed in recent years. Kim studied the flocculation of several green algae by using bacteria, and the recovery ratio was over 90% [29]. The microbial flocculation method has the advantages of low cost, safety, and pollution-free.

Table 4. Summary of harvest costs and energy consumption of microalgae [27,30]

Technique	Pros	Cons	Cost（$·hm^{-2}）	Energy consumption (kwh·m^{-3})
Flocculation	Low capital cost	Low water removal ratio	2,000	~0
Centrifugation	Fast separation rate, high recovery rate	High cost and high energy cost	12,500	3.29
Filtration	High efficiency, medium cost	Limited application, pollution of filters	9,884	0.5~5.9

hm^2: square hectometer

3.3 Microalgae Dehydration and Lipid Extraction

The most effective dewatering technology can only reduce the water content of microalgae slurry to 65-80 wt%. Drying microalgae to a lower water content of less than 80% requires dehydration processes, which increase energy consumption and cost [31]. Such dehydration processes include drying microalgae with sunlight, fixed bed or spray dryers. The energy input of the microalgae-based biodiesel process using dry microalgae is more than energy output. Traditional lipid extraction processes separate microalgal lipids from the water phase with organic solvents, such as methyl ether and n-hexane. But the extraction efficiency is low and it is difficult to recover the extraction solvent. Table 5 compares the cost of microalgae dehydration and lipid extraction.

Table 5. Summary of costs of microalgae dehydration and lipid extraction [27]

Operation	Capital cost ($)	Operation cost ($)	Methods
Dehydration	250,000	45,251	Solar drying/fixed bed drying
Extraction	150,000	7,332	methyl ether, n-hexane

4.Conclusions and Prospects

At the present stage, the production of biodiesel from microalgae is still not an economical process, and it is difficult to achieve industrialization in China. Reducing the cost is the major goal in the future [32, 33]. The cost of microalgae processes decreases in following order: microalgae culture > microalgae harvest > dehydration and lipid extraction. These three steps account for the major cost of microalgae-based diesel production, and they are closely related to each other. The low microalgae concentration is the reason of the high harvest cost, while the concentration of microalgae harvested is the key to the cost of lipid extraction. Therefore, the development of the novel microalgae technology should not only focus on the main steps, but also consider coupling between different processes.

Such technologies may include metabolic engineering, comprehensive utilization of energy, and well-developed scaling-up technology. For the microalgae cultivation, with the progress of genetic engineering, it is expected to develop ideal algal species, which can be cultivated with the improved culture system. To reduce simultaneously the cost of equipment and energy consumption of harvesting microalgae, the new technologies like biological flocculation might be used. For the microalgal lipid extraction, some new techniques may avoid the dehydration step and combine harvesting and extraction steps together, and thus develop an economical biodiesel production process. Furthermore, microalgae are rich in pigment, protein, polysaccharides, unsaturated fatty acids, and other bioactive substances, which can be used for the chemical, food, pharmaceutical and feed industry, etc. These useful components should be co-produced with the biodiesel to reduce the processing cost.

ACKNOWLEDGMENTS

This research was supported by the program for Henan Province Natural Science Foundation of China (No. 162300410250), and the crosswise project of Henan Tianguan Biofuel Eng. Co. Ltd., China. (No. 211500532704).

CONFLICTS OF INTEREST

The authors declare that there is no conflict of interests regarding the publication of this paper.

REFERENCES

[1] Li Hua, Wang Wei-bo, Liu Yong-ding, Xu Ai-hua, Li Dun-hai, Shen Yin-wu. The development of microalgae biodiesel and the utilization of oleaginous microalgae. Renewable Energy Resources, 2011, 29(4): 84-89
[2] Liu Jian-guo, Long Yuan- ru, Huang Yuan, Pang Tong, Lin Wei, Li Ling. The research status, problems and developmental strategies in culture microalgal for biodiesel. Marine Sciences, 2013, 37(10): 132-141
[3] You Jin-kun, Yu Xu-ya, Cui Jia-li. Review on the situation and trend of producing biodiesel from microalgae. China Oils and Fats. 2011, 36(3): 47-51
[4] Huang Ying-ming, Wang Wei-liang, Li Yuang-guang, Xie Jing-li, Fan Jian-hua, Tao Li-ming. Strategies for research and development and commercial production of microalgae bioenergy. Chinese Journal of Biotechnology, 2010, 26(7): 907-913
[5] Mei Hong, Zhang Cheng-wu, Yin Da-cong, Gen Ya-hong, Ouyang Zheng-rong, Li Ye-Guang. Survey of studies on renewable energy production by microalgae. Journal of Wuhan Botanical Research, 2008, 26(6): 650-660
[6] Illman AM, Scragg AH, Shales SW. Increase in Chlorella strains calorific value when grown in low nitrogen medium. Enzyme Microb Technol, 2000, 27: 631-635
[7] Takagi M, Karseno, Yoshida T. Effect of salt concentration on intra-cellular accumulation of lipids and triacylglyceride in marine microalgae Dunaliella cells. Journal of Bioscience and Bioengineering, 2006, 101(3): 223-226
[8] Gao Chun-fang, Yu shi-shi, Wu Qing-yu. Advance of Biodiesel from microalgae. Biology Bulletin, 2011, 46(6): 1-5

[9] Liao Xiaoling, Wu Qingyu. Bio-oil fuel production from microalgae after heterotrophic growth. Renewable Energy, 2004, (4): 41-44
[10] Li Daoyi, Li Shujun, Liu Tianshu, Zhao Fengmin, Yang Juntai, Li Dong. Technology of Microalgae Bioenergy Industrialization. Journal of Agricultural Machinery, 2010, 41(S1): 160-166
[11] Chen P, Min M, Chen Y, *et al.* Review of the biological and engineering aspects of algae to fuels approach. International Journal of Agricultural and Biological Engineering 2009, 2(4): 1-30
[12] Molina G E, Belarbi E H. Acien Fernandez F G, *et al*. Recovery of microalgal biomass and metabolites process options and economics. Biotechnology Advances, 2003, 20(7-8): 491-515
[13] Sun Li-ying, He Hao, Tian Yi-shui, Qi Pan-lun, Zhao Li-xin. Key issues discussion of large-scale production of microalgae. Renewable Energy Resource, 2012, 30(9): 70-74
[14] Hao Zong-di, Yang Xun, Shi Jie, Zhang Sen, Liu Ping-huai. Research progress of microalgal biodiesel. Journal of Shanghai Ocean University, 2013, 22(2): 282-288
[15] Chen Jianqiu. Green renewable energy –development and utilization of energy microalgae. Journal of Green Science and Technology, 2012, (9): 117-118.
[16] Zhang Fang, Cheng Li-hua, Xu Xin-hua, Zhang Lin, Chen Huan-lin. Technologies of Microalgal Harvesting and Lipid Extraction. Progress in Chemistry, 2012, 24(10): 2062-2072
[17] Liu Tian-zhong, Wang Jun-feng, Chen Lin. Status and trends of energy microalgae and their biorefinery. Biobusiness, 2015, (4): 31-39
[18] Wahlen BD, Willis RM, Seefeldt LC. Biodiesel production by simultaneous extraction and conversion of total lipids from microalgae, cyanobacteria, and wild mixed-cultures. Bioresource Techonlogy, 2011, 102(3): 2724-2730
[19] Zhang Gui-zhi, Wang Yong, Cao Ning, Du Chang. Preparation of Biodiesel from Microalgae by direct transesterification under supercritical methanol conditions. Biomass Chemical Engineering, 2012, 46(1): 6-19
[20] Yang C, Li R, Cui C, *et al*. Catalytic Hydroprocessing of Microalgae-Derived Biofuels: A Review. Green Chemistry, 2016, 18(13): 3684-3699
[21] Wu Li-zhu, Dou Shi-juan, Cong Jun-guang, Yang Guo-jun, Liu Jin-feng. The background and development strategy of Microalgae Biodiesel. Current Biotechnology, 2015, 5(2): 85-88
[22] Zhang Ying-wei, Liu Wei. Advances in the research of Microalgae Bioenergy. Marine Sciences, 2012,36(1): 132-138
[23] Ryan Davis, Andy Aden, Philip T. Pienkos. Techno-economic analysis of autotrophic microalgae for fuel production. Applied Energy, 2011, 88(10): 3524-3531
[24] Jason C. Quinn, Ryan Davis. The potentials and challenges of algae based biofuels: A review of the techno-economic, life cycle, and resource assessment modeling. Bioresource Technology, 2015, 184: 444-452
[25] Zhang Ting-ting, Xie Xiao-min, Huang Zhen. Life Cycle Analysis of Microalgal Biodiesel in China. Journal of Shanghai Jiao Tong University, 2014, 48(6): 750-755.
[26] Benjamin Taylor, Ning Xiao, Janusz Sikorski, *et al*. Techno-economic assessment of carbon-negative algal biodiesel. Applied Energy, 2013, 106(6): 262-274.
[27] Li Fei, Bai Jing, Chang Chun, Fang Shu-qi, Li Hong-liang, Chen Jun-ying, Han Xiu-li. Developments of cost control technologies to produce biodiesel from microalgae. Modern Chemical Industry, 2015, 35(5): 16-20

[28] Chen guo, Zhao Jun, Su Peng-fei, Chen Hong-wen. Progress in biodiesel production from microalgae. Chemical Industry and Engineering Progress, 2011, 30(10): 2186-2193
[29] Kim D, La H, Ahn C, *et al*. Harvest of Scenedesmus sp. with bioflocculant and reuse of culture medium for subsequent high-density cultures. Bioresource Technology, 2011, 102(3): 3163-3168
[30] Jason C Quinn, Gordon T Smith, Cara Meghan Downes, *et al*. Microalgae to biofuels lifecycle assessment-multiple pathway evaluation. Algal Research, 2014, 4(4): 116-122
[31] Lardon L, Hélias A, Sialve B, *et al*. Life-cycle assessment of biodiesel production from microalgae. Environ Sci Technol, 2009, 43(17): 6475–6481
[32] Qiao Kai, Jia Lu. Biodiesel production from microalgae and its case economic analysis. Petroleum & Petrochemical Today, 2015, (9): 30-35
[33] Hasan R, Zhang B, Wang L, *et al*. Bioremediation of Swine Wastewater and Biodiesel Production by Using Chlorella Vulgaris, Chlamydomonas Reinhardtii, and Chlamydomonas Debaryana. Journal of Petroleum & Environmental Biotechnology, 2014, 5(3): 175

Trends in Renewable Energy
OPEN ACCESS ISSN: 2376-2144
Peer-Reviewed Article futureenergysp.com/index.php/tre

Energetic and Exergetic Evaluation of Biomass Fired Water Heating System

N. L. Panwar* and Arjun Sanjay Paul

Department of Renewable Energy Engineering, College of Technology and Engineering, Maharana Pratap University of Agriculture and Technology, Udaipur (Rajasthan) 313001, India.

Received October 6, 2017; Accepted November 2, 2017; Published November 4, 2017

This paper deals with thermal and exergy efficiencies of biomass fired water heating system. Water heating system is extensively suitable to generate hot water in rural areas. The developed water heating system was tested with Desi babul (*Acacia nilotica*) wood. Thermal and exergy efficiencies of the system were estimated at 54.5 percent and 6.79 percent, respectively.

Keywords: Biomass water heater; Exergy efficiency; Thermal efficiency; Rural applications

Introduction

It is well known fact that biomass is an indirect source of solar energy, and it is a renewable energy resource available where the climatic conditions are favorable for plant growth and production [1-3]. Biomass combustion is going to increase worldwide for a provision of heat and electricity. Approximately 60% of total biomass is used for energy purposes are traditional biomass that is fuel wood, while crop residues and the remaining biomass are used for modern bio-energy. Biomass can play vital role in responding to concerns over the protection of the environment as well as the security of an energy supply [4-5]. From ancient time, biomass is the main fuel which is used for cooking and water heating. But due to urbanization and industrialization, these biomass are replaced by modern fuel like kerosene, LPG and electricity. However, these conventional sources of energy are exhaustible in nature. It is essential to find an economical, convenient and efficient way to replace these conventional sources by renewable sources like biomass and solar as alternate fuel with improved technology to maximize the energy efficiency.

Comprehensive literature is available on various aspects of biomass combustion devices. However, literature on exergy analysis of biomass fired water heating system is limited. Saidur *et al.* performed an exhaustive literature survey on the exergy assessment of various biomass that can be used as fuel for cookstove [6]. Tyagi *et al.* presented an experimental and comparative performance evaluation, using energy and exergy analyses, of four metallic types of cook stoves [7]. Further, Panwar presented a study on assessment of energy and exergy of improved biomass cookstoves [8]. Biomass fired water heating systems are capable to generate hot water whenever it is required, and significantly contribute to reduction of greenhouse gases. Despite these advantages, there is very little literature available on energetic and exergetic analyses of such water heating system.

*Corresponding author: nlpanwar@rediffmail.com

Tr Ren Energy, 2017, Vol.3, No.2, 153-159. doi: 10.17737/tre.2017.3.2.0043

Therefore, the present experimental study was conducted to assess the energetic and exergetic performance of the biomass fired water heating system.

Materials and Methods

System Description

The biomass-fired water heating system consists of two concentric cylinders, *i.e.* the inner cylinder and the outer cylinder made of stainless steel SS 304. Actual combustion takes place in the inner cylinder, which has a diameter of 20 cm, whereas the outer shell has a diameter of 30 cm. During the experiment, the water was poured between these two cylinders. The outer shell was insulated with glass wool to minimize heat loss. The grate was made of a mild steel round bar. To maintain the proper draft during the combustion of the biomass, a chimney was placed on the top of the combustion chamber, as illustrated in Figure 1. One water tap was placed at on the upper side of the water tank to drain hot water, and another tap was placed at the bottom side to drain the water when the system is not in use. The technical specification of the developed water heating system is presented in Table 1.

Table 1. Technical specification of biomass fired water heating system.

No.	Component	Dimension in cm	Material
1.	Inner cylinder	Diameter = 20 Height = 60	SS 304
2.	Outer cylinder	Diameter = 30 Height = 60	SS 304
3.	Chimney	Diameter = 5 Height = 90	Galvanised iron（GI)
4.	Grate	Diameter = 19	Mild steel round bar
5.	Insulation	Thickness = 0.4	Glass wool
6.	Insulation cover	Diameter = 30.8 Height = 90	Aluminum sheet

Thermal Performance

Proximate analysis of the fuel - Desi Babul wood (*Acacia nilotica*), which was purchased from a local market, was carried out prior to the test by using the method suggested by the literature [9]. The physical and thermal properties of the fuel wood are presented in Table 2.

Seven trials were undertaken under different conditions to study the thermal efficiency of the developed system. The calorific value of fuel wood was calculated by using a digital bomb calorimeter (Advance Research Instruments Company, Delhi, India). A multi-channel temperature scanner (ADI-Vadodara, Gujarat, India) with calibrated NiCr–Ni thermocouples was used to measure the ambient air temperatures, water inlet and out temperature.

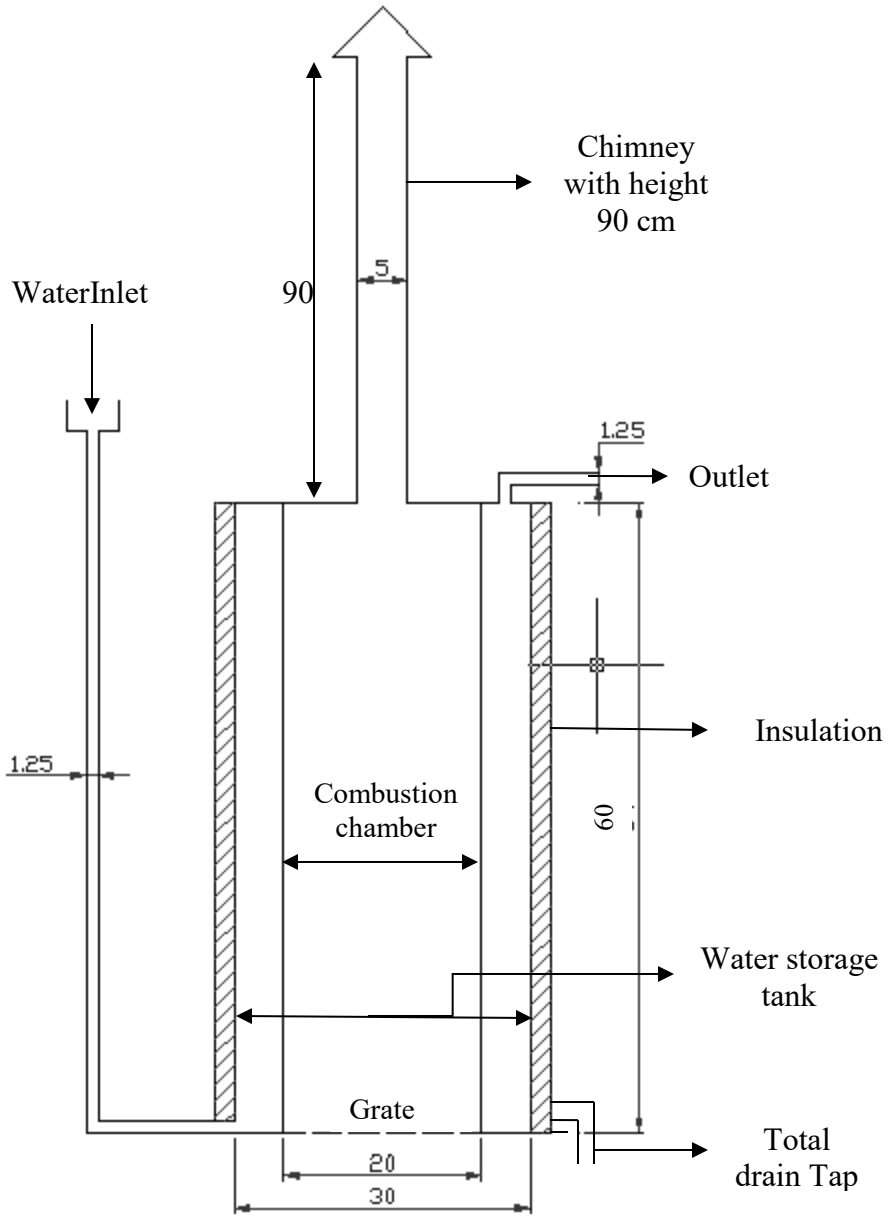

Figure 1. Schematic of biomass fired water heating system (all dimension in cm).

Table 2. Physical and thermal properties of the fuel wood

Characteristic	Biomass (Desi Babul wood, *Acacia nilotica*)
Size (mm)	25-40
Length (mm)	50-75
Bulk density (kg·m^{-3})	350
Moisture content (wt% wet basis)	5.6
Volatile matter (wt% dry basis)	82.52
Ash content (wt% dry basis)	1.05
Fixed carbon (wt% dry basis)	16.43
Calorific value (Higher heating Value, HHV, unit: MJ/kg)	19.157

Thermal efficiency of system is calculated by the following formula:

$$\mathrm{H_{out}} = M_w Cp_w \Delta T \qquad \text{Eqn. 1}$$

$$\mathrm{H_{in}} = M \times Cv \qquad \text{Eqn. 2}$$

$$\eta_{\mathrm{th}} = \frac{heat\ utilized\ by\ system}{total\ thermal\ energy\ avialable\ in\ wood} = \frac{H_{out}}{H_{in}} \qquad \text{Eqn. 3}$$

Exergy Analysis

Energy assessment is the customary method of assessing the way that energy is used in an operation involving the physical or chemical processing of materials and the transfer and/or conversion of energy. Energy analysis is based on the first law of thermodynamics: Net heat supplied is converted in order to work. Thus, energy analysis ignores reductions of energy potential and can provide sound management guidance for those applications in which the usage effectiveness depends exclusively on energy quantities. Such analyses are suitable for sizing and analyzing of systems using only one form of energy [10].

The exergy contents of biomass can be calculated by using their higher heating or lower heating values. Both higher and lower heating values are the function of the weight fraction (wt%, dry) of the chemical composition of biomass such as carbon (C), hydrogen (H), oxygen (O), nitrogen (N), etc. The higher heating value (HVV) of biomass can be calculated by using the correlation proposed by [11-12].

$$HHV = \left[33.5(C) + 142.3(H) - 15.4(O) - 14.5(N)\right] \times 10^{-2} \qquad \text{Eqn. 4}$$

Similarly, lower heating value (LHV) can be computed using correlation proposed by [13].

$$LHV = HHV\left(1 - H_2O_i\right) - 2440\left(H_2O_i + 9H_i\right) \qquad \text{Eqn. 5}$$

where H_2O_i and H_i state the moisture content of biomass and the weight of hydrogen in biomass.

Correlation can be used for estimating the exergy of biomass suggested by [14].

$$Ex_{biomass} = \beta \times LHV_{biomass} \qquad \text{Eqn. 6}$$

where β is the quality factor and can be calculated as follows:

$$\beta = \frac{1.0412 + 0.2160\left(\frac{H}{C}\right) - 0.2499\left(\frac{O}{C}\right)\left[1 + 0.7884\left(\frac{H}{C}\right)\right] + 0.0450\left(\frac{N}{C}\right)}{1 - 0.3035\left(\frac{O}{C}\right)} \quad \text{Eqn. 7}$$

Exergy output of improved cookstove is depended on the heat utilized to boil the water and amount of water evaporated. It can be written as follows:

$$Ex_{out} = H_{out}\left(1 - \frac{T_o}{T_{aw}}\right) \quad \text{Eqn. 8}$$

where T_{aw} state for average water temperature

Therefore, exergy efficiency (ψ) can be written as follows:

$$\psi = \frac{Ex_{out}}{Ex_{biomass}} \quad \text{Eqn. 9}$$

Results and Discussion

Thermal Performance

Thermal efficiency of the developed system was estimated using equations (1-3). To assess the thermal performance, total 80 liters of water was used to raise the temperature from 30°C to average temperature about 61°C in one hour, and one kg of babool (*Acacia nilotica*) wood was consumed. The developed biomass fired system illustrated in Figure 2. Thermal efficiency was estimated at about 54.50 %.

Figure 2. Developed biomass fired water heater

Exergy Assessment

Ultimate analysis of Desi babul (*Acacia nilotica*) was carried out to assess the exergetic performance of cookstoves as presented in Table 3. Exergy efficiency was calculated using equation (9). The exergy efficiency of biomass fired water heating system was about 6.79 %

Table 3. Ultimate analysis of biomass (wt%)

Biomass	C	H	O	N
Acacia nilotica	48.82	4.78	0.28	46.12

Conclusions

Biomass is the most convenient form of renewable resources. A country's socio-economy cannot show progressive development unless energy is explored, developed, distributed and utilized in an efficient and appropriate way. In this study, the performance of the developed system was tested with Desi babul (*Acacia nilotica*) wood. Efficiency was determined through water heating tests. The developed system delivers 80 litres of hot water per hour per one kg of biomass at average temperature 61°C. The developed water heating system brings potential benefits like reduced emission of the greenhouse gases and reduced fuel demand with economic and time saving benefits to the household, and increases sustainability of the natural resources.

CONFLICTS OF INTEREST

The authors declare that there is no conflict of interests regarding the publication of this paper.

REFERENCES

[1] Panwar, N.L. and Rathore, N.S., 2008. Design and performance evaluation of a 5 kW producer gas stove. *Biomass and Bioenergy*, 32(12), 1345–1352. DOI:10.1016/j.biombioe.2008.04.007

[2] Panwar, N.L., 2010. Performance evaluation of developed domestic cook stove with Jatropha shell., *Waste Biomass Valor.*, (1), 309–314. DOI:10.1007/s12649-010-9040-8

[3] Panwar, N.L., Kaushik, S.C. and Kothari, S., 2011. Role of renewable energy sources in environmental protection: a review. *Renewable and Sustainable Energy Reviews*, 15, 1513–1524. DOI:10.1016/j.rser.2010.11.037

[4] Xu, R., Ferrante, L., Briens, C. and Berruti, F., 2009. Flash pyrolysis of grape residues into biofuel in a bubbling fluid bed. *J. Anal. Appl. Pyrol.*, 86(1), 58–65. DOI:10.1016/j.jaap.2009.04.005

[5] Kobayashi, N. and Fan, L-S., 2011. Biomass direct chemical looping process: a perspective. *Biomass and Bioenergy.*, 35(3), 1252–1262. DOI:10.1016/j.biombioe.2010.12.019
[6] Saidur, R., BoroumandJazi, G., Mekhilef, S. and Mohammed, H.A., 2012. A review on exergy analysis of biomass based fuels. *Renew Sustain Energy Rev.*, 16(2), 1217–1222. DOI:10.1016/j.rser.2011.07.076
[7] Tyagi, S.K., Pandey, A.K., Sahu, S., Bajala, V. and Rajput, J.P.S., 2013. Experimental study and performance evaluation of various cook stove models based on energy and exergy analysis. *J. Therm. Anal. Calorim.*, 111(3), 1791–1799. DOI:10.1007/s10973-012-2348-9
[8] Panwar, N.L., 2014. Energetic and exergetic performance evaluation of improved biomass cookstoves. *Int. J. Exergy*. 14(4), 430–440. DOI:10.1504/IJEX.2014.062910
[9] ASTM (1983) *Annual Book of ASTM Standard*, American Society for Testing and Materials 19103, Philadelphia.
[10] Panwar, N. L., Kothari,, S., and Kaushik, S.C., 2013. Energetic and exergetic analysis of three different solar cookers. J. Renewable Sustainable Energy., 5(023102). DOI: 10.1063/1.4793784
[11] Bilgen, S., Kaygusuz, K. and Sari, A., 2004. Second law analysis of various types of coal and woody biomass in Turkey. *Energy Sources*, 26(11), 1083–1094. DOI:10.1080/00908310490494621
[12] Kalinci, Y., Hepbasli, A. and Dincer, I., 2011. Exergetic performance assessment of gasification and pyrolysis processes of pre-treated wood board wastes. *Int. J. Exergy*., 8(1), 99–112. DOI:10.1504/IJEX.2011.037217
[13] Finet, C., 1987. Heating value of municipal solid waste. Waste Management and Research, 5(1), 141–145. DOI:10.1016/0734-242X(87)90047-4
[14] Szargut, J. and Styrylska, T., 1964. Approximate evaluation of the exergy of fuels. *Brennstoff Wärme Kraft*, 16, 589–596.

Trends in Renewable Energy
OPEN ACCESS ISSN: 2376-2144
Peer-Reviewed Article futureenergysp.com/index.php/tre

A Review of Regression Models Employed for Predicting Diffuse Solar Radiation in North-Western Africa

Ogbulezie Julie C.[1], Ushie Ogri James[2], Nwokolo Samuel Chukwujindu[1*]

[1]*Department of Physics, Faculty of Physical Sciences, University of Calabar, Nigeria, P.O. Box 2892, Calabar, Nigeria*
[2]*Department of Electrical/Electronic Engineering, Faculty of Engineering, University of Calabar, P.O. Box 2892, Calabar, Nigeria*

Received September 28, 2017; Accepted November 14, 2017; Published November 14, 2017

The knowledge of diffuse solar radiation (H_d) is of almost importance for determining the gross primary productivity, net ecosystem, exchange of carbon dioxide, light use efficiency and changing colour of the sky. However, routine measurement of H_d is not available in most locations in North-Western Africa. During the past 36 years in order to predict H_d in the horizontal surface on hourly, daily and monthly mean basis, several regression models have been developed for numerous locations in North-Western Africa. As a result, several input parameters have been utilized and different functional forms applied. The regression models so far utilized were classified into six main categories and presented based on the input parameters applied. The models were further reclassified into numerous main groups and finally represented according to their developing year. In general, 188 regression models, 33 functional forms and 20 groups were reported in literature for predicting H_d in North-Western Africa. The regression and soft computing models developed within North-Western Africa and across the globe were examined in order to determine the best technique of prediction. The result revealed that soft computing models are more suitable for predicting H_d in North-Western Africa and across the globe.

Keywords: Diffuse solar radiation; Regression models; Classification; Functional forms; North-Western Africa

1. Introduction

As a result of exponentially increasing costs of fossils, uncertainty of availability and transportation, environmental pollution, and general awareness amongst common people, the renewable sources which are environmental friendly since they have much lower environmental impact compared to conventional sources have enabled smart energy to gain more attention from researchers, governments, non-governmental organisations (NGOs) and industries etc. in recent years due to the rapid growth of the global energy demands. Solar energy in the form of radiation received at the surface of the earth is the most preferred sustainable source of renewable energy in the form of solar photovoltaic, solar thermal. Other sources of renewable energy are wind, biomass, small and big hydro, tidal, wave, ocean etc. as a result of their inexhaustible nature and abundant availability globally. These attributes make solar energy to be accepted worldwide as a key energy

*Corresponding author: nwokolosc@stud.unical.edu.ng

Tr Ren Energy, 2017, Vol.3, No.2, 160-206. doi: 10.17737/tre.2017.3.2.0042

source for the future with respect to the environmental issues associated with fossils as well as their limited reserves. Therefore, solar energy is the best substitute of fossils owing to the ever growing demand for energy globally. In fact, about 40 GW of solar photovoltaics (PV) capacity was installed in 2014 and the International Energy Agency, IEA [1] predicts that by 2050, photovoltaic (PV) as a renewable energy source (solar energy) may become one of the most promising sources of energy that will provide about 11% of global electricity production and would reduce 2.3 gigatonnes of CO_2 emissions per year. As a result, more and more penetration of solar energy technologies to the worlds' energy sector is indeed appealing for supplying a notable part of the electricity, heating, cooling, cooking, and drying of all types of things: clothes, agricultural produce, cash crops, and bricks etc. Therefore, a good working knowledge of available solar energy obtained principally from global solar radiation with its diffuse and direct components in a particular location are of great importance in designing and sizing of solar energy conversion systems.

Diffuse solar radiation is the component of global solar radiation reaching the earth's surface after having been scattered from the direct horizontal irradiation by molecules, aerosols or suspended particular matter such as black carbon, organic carbon, dust and sea salt in the atmosphere. Diffuse solar radiation plays an important role in determining the gross primary productivity, net ecosystem exchange of carbon dioxide, light use efficiency, changing colour of the sky and baseline for estimating and understanding diffuse solar radiation parameters such as diffuse solar radiation and global solar radiation on surfaces, diffuse photosynthetically active radiation etc. Moreover, solar energy among other sources of renewable energy has remained the most viable source of energy that has the capacity to sustain and maintain all the activities and processes that support life of animals, supply heat to the atmosphere and lands, generate its wind, drive the water cycle, warm the ocean and support life of plants.

The accurate determination and clear understanding of the diffuse solar radiation parameters is required for many applications such as energy management, solar energy, light studies, architectural research, hydrological process and biometeorology, crop production, remote sensing of vegetable and carbon cycle modelling, designing and sizing photovoltaic systems, development of thermal and electrical solar energy devices [2-6].

Diffuse solar radiation arises as a result of the interaction between the solar radiation incident on the top of the earth's atmosphere and the matter within it. Thus, understanding how this radiometric flux interacts with the matter within it and relates with its immediate environment thereby influencing diffuse light availability for energy, sky colour, agricultural, material and technological production and utilization for man's need is of utmost importance for modelling and estimating diffuse solar radiation in a particular geographical environment.

Diffuse solar radiation varies from one geographical location to another. It is a function of meteorological parameters such as evaporation, effects of cloudiness, relative humidity, precipitation, temperature, sunshine duration, extraterrestrial solar radiation, and reflection of the environs; geographical parameters such as latitude, longitude and elevation of the site; geometrical factors such as azimuth angle, sun azimuth angle; astronomical parameters like solar constant, earth-sun distance, solar declination and hour angle; physical parameters such as scattering air molecules, water vapour content, scattering of dust and other atmospheric constituents like O_2, N_2, CO_2, and O.

Measurement of diffuse solar radiation is often performed in many parts of the world by mounting a pyranometer on the axis of the ring on a roof top so as to receive only diffuse solar radiation and the ring is normally adjusted regularly to ensure that the direct

irradiance does not reach the pyranometer. As a result of cost of measuring equipment, its maintenance and calibration requirements, in rural and developing countries in Africa and several places around the world, several empirical models had been developed in Africa and other locations across the globe that can produce diffuse solar radiation data without the substantial cost of the instrumentation network that would otherwise be needed [7-10].

The most primitive model for estimating diffuse solar radiation was developed by Liu and Jordan [11]. These solar energy researchers correlated diffuse fraction (H_d/H) with clearness index (k_t). Their investigation has been adopted by numerous solar energy researchers in Nigeria and Egypt and across the globe as a baseline further developing regression models for estimating diffuse solar radiation using the same parameter, other meteorological parameters, geographical parameters, geometrical parameters and astronomical parameters that will best fit the local climate of their study.

However, diffuse solar radiation and other components of solar radiation such as direct normal irradiance, photosynthetically active radiation, evapotranspiration etc. have been predicted employing different soft computing techniques in recent times. This constitutes a widely accepted technique offering an alternative way to synthesize complex problems associated with solar energy prediction. These problems include inability to handle non-linear relationships in data; applying only calculable atmospheric, meteorological, astronomical, geographical, geometrical parameters such as extraterrestrial solar radiation, latitude, altitude, longitude, maximum sunshine duration, azimuth angle, solar declination, cosine of solar zenith angle, and hour angle. The soft computing technique has the capacity of accepting many input parameters for a particular model which is not possible applying regression technique and this strengthens its reliability. Therefore, applying soft computing techniques compared to regression techniques according to previous studies offers greater accuracy with prediction error in a range (less than 20 %) and could be very good in terms of diffuse solar radiation prediction as more and more soft computing approaches are demanded in the domains of renewable energy resource prediction [12-21].

Therefore, the main purpose of the study was to review regression models fitted in literature for predicting diffuse solar radiation in North-Western Africa and its objectives are identifying several input parameters and functional forms ever applied for predicting diffuse solar radiation in North-Western Africa; classify the regression models commonly employed in this part of Africa according to the main input parameters; compare the performance of regression and soft computing models applied and decide the best technique that can yield high accuracies of estimation for future purposes and finally identify the research gap.

2. Basic Parameters

The principal parameter of sunshine duration fraction, daily extraterrestrial radiation on the horizontal surface is significant for the prediction of diffuse solar radiation. Sunshine duration fraction is the ratio of actual sunshine duration to maximum possible sunshine duration expressed theoretically as:

$$S_o = \frac{2}{15}\cos^{-1}\left[-\tan\delta\tan\phi\right] \quad (1)$$

$$\delta = 23.45 \sin\left[\frac{360(n+284)}{365}\right] \quad (2)$$

Where ϕ is the latitude, δ is the solar declination given by Yaniktepe and Genc [22] and n is the number of days of the year starting from first January. The daily extraterrestrial solar radiation is the solar radiation intercepted by horizontal surface during a day without the atmosphere and hourly extraterrestrial radiation has similar definition.

Hourly extraterrestrial solar radiation on the horizontal surface is given by Zhang *et al.* [23] as:

$$I_O = \frac{12 \times 3600 \times I_{SC}}{\pi}\left(1 + 0.033\cos\frac{360n}{365}\right) \times \left(\cos\phi\cos\delta(\sin\omega_2 - \sin\omega_1)\sin\omega_S + \frac{\pi(\omega_2 - \omega_1)}{180}\sin\phi\sin\delta\right) \quad (3)$$

While the daily extraterrestrial solar radiation on the horizontal surface is given by Yaniktepe and Genc [23] as:

$$H_O = \frac{24}{\pi} I_{SC}\left(1 + 0.033\cos\frac{360n}{365}\right) \times \left(\cos\phi\cos\delta\sin\omega_S + \frac{2\pi\omega_S}{360}\sin\phi\sin\delta\right) \quad (4)$$

Where the mean sunrise hour angle (ω_s) can be evaluated as:

$$\omega_s = \cos^{-1}[-\tan\delta\tan\phi] \quad (5)$$

Isc is the solar constant, ω_1 and ω_2 are the limit hour angle of an hour, in which ω_2 is the larger, all in degrees and other symbols retain their usual meaning.

3. Evaluation Metrics

Evaluation, principally compares how well the observed and predicted fit each other. This evaluation is applied at numerous steps of the computing model development as for instance during the evaluation of the prediction model itself (during the training of a statistical model for instance), for judging the improvement of the computing model after some modifications and for comparing numerous computing models. As previously mentioned, this performance comparison is not easy for numerous reasons such as different predicted time horizons, numerous time scales of the predicted data and variability of the meteorological conditions from one site to another one. It works by comparing the predicted outputs $\hat{y}$ with observed data y which are also measured data themselves linked to an error (or precision) of a measure.

Graphic tools are available for predicting the adequacy of the computing model with the experimental measurements via:

1. Time series of predicted diffuse solar radiation in comparison with measured diffuse solar radiation which allows visualizing easily the estimation quality. In Fig. 1a, for instance, high estimate accuracy in clear-sky conditions and a low one in partly cloudy conditions can be seen.
2. Scatter plots of estimated over measured diffuse solar radiation(as shown in Fig. 1b) which can reveal systematic bias and deviations depending on the diffuse solar radiation conditions and show the range of deviations that are related to the estimates.
3. Receiver Operating Characteristic (ROC) curves which compare the rates of true positives and false positive.

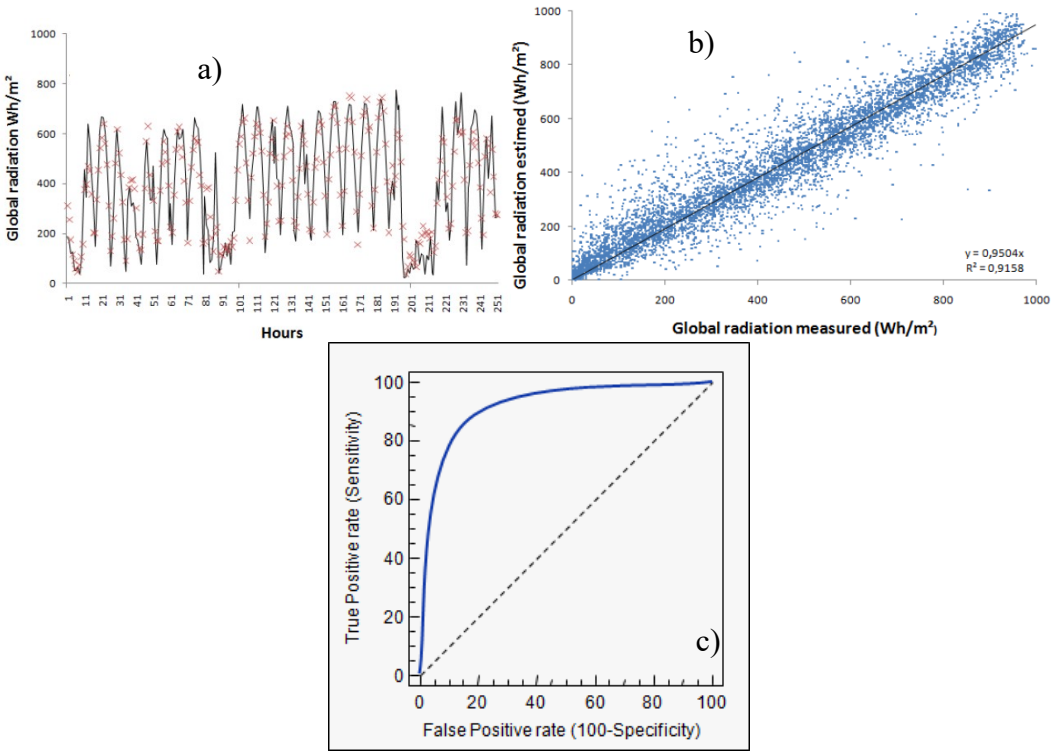

Fig. 1. a) Time series of predicted and measured global radiation for 2008 in Ajaccio (France); b) Scatter plot of predicted vs. measured global radiation in Ajaccio (France); c) Example of ROC curve (an ideal ROC curve is near the upper left corner).

Up till now, there is no standard evaluation measures accepted for diffuse solar radiation measurement, which makes the comparison of the estimating methods difficult. Sperati *et al.* [24] presented a benchmarking exercise within the framework of the European Actions Weather Intelligence for Renewable Energies (WIRE) with the purpose of evaluating the performance of state of the art computing models for short term renewable energy prediction or forecasting. This research is a very good example of reliability parameter utilization. They concluded that: "More work using more test cases, data and computing models needs to be performed in order to achieve a universal overview of all possible conditions. They also pointed out that test cases located all over Europe, the US and other relevant countries should be considered, in an effort to represent most of the possible meteorological conditions". This study therefore illustrates very well the difficulties of performance comparisons encountered for diffuse solar radiation prediction. The commonly applied statistics for diffuse solar radiation prediction include the following: The Mean Bias Error (MBE) represents the mean bias of the prediction:

$$MBE = \frac{1}{N} \times \sum_{i=1}^{N} \left(\hat{y}(i) - y(i) \right) \quad (6)$$

$\hat{y}$ is the predicted diffuse solar radiation, y the measured diffuse solar radiation and N the number of observations. The prediction will under-estimate or over-estimate the observations. Thus, MBE is not a good statistical indicator for the reliability of a computing model because the errors compensate each other but it allows seeing how much it overestimates or underestimates.

The Mean Absolute Error (MAE) is appropriate for comparing diffuse solar radiation estimation with linear cost functions, *i.e.*, where the costs resulting from a poor prediction are proportional to the estimation error:

$$MAE = \frac{1}{N} \times \sum_{i=1}^{N} \left| \hat{y}(i) - y(i) \right| \quad (7)$$

The mean square error (MSE) applies the squared of the difference between observed and estimated data. This statistical indicator penalizes the highest gaps:

$$MSE = \frac{1}{N} \times \sum_{i=1}^{N} \left(\hat{y}(i) - y(i) \right)^2 \quad (8)$$

MSE is principally the statistical parameter which is minimized by the training algorithm.

The Root Mean Square Error (RMSE) is more sensitive to big prediction errors, and thus is good for applications where small errors are more tolerable and larger errors cause disproportionately high costs, as in the case of utility applications (http://www.cost.eu/about_cost). It is probably the reliability parameter that is most appreciated and employed:

$$RMSE = \sqrt{MSE} = \sqrt{\frac{1}{N} \times \sum_{i=1}^{N} \left(\hat{y}(i) - y(i) \right)^2} \quad (9)$$

The Mean Absolute Percentage Error (MAPE) is close to the MAE but each gap between observed and predicted value is divided by the observed value so as to consider the relative gap.

$$MAPE = \frac{1}{N} \times \sum_{i=1}^{N} \left| \frac{\hat{y}(i) - y(i)}{y(i)} \right| \quad (10)$$

This statistical indicator has a challenge that it is unstable when y(i) is near zero and it cannot be defined for y(i)=0.

Of recent, these errors are normalized particularly for the RMSE; as reference the mean value of global radiation is generally employed but other definitions can be applied:

$$nRMSE = \frac{\sqrt{\frac{1}{N} \times \sum_{i=1}^{N} \left(\hat{y}(i) - y(i) \right)^2}}{\bar{y}} \quad (11)$$

With $\bar{y}$ is the mean value of y. Other statistical indicators exist and can be employed as the correlation coefficient (R), coefficient of determination (R^2), or the index of agreement (d) which is normalized between 0 and 1.

As the prediction accuracy strongly depends on the location and time period applied for evaluation and on other parameters, it is difficult to evaluate the quality of estimation from accuracy metrics alone. Then, it is best to compare the accuracy of different estimations against a common set of test data Pelland *et al.* [25]. "Trivial" prediction approach can be applied as a reference [26], the most common one is the persistence model ("things stay the same", Trapero *et al.*, 2015) where the prediction is always equal to the last known data point. The diffuse solar radiation has a deterministic component due to the geometrical path of the sun. This characteristic may be included as a constraint to the simplest form of persistence in considering as an example, the measured data of the previous day or the previous hour at the same time as a prediction value. Other common reference forecasts include those based on climate constants and simple autoregressive methods. Such comparison with referenced NWP computing model is shown in Fig. 2. Generally, after 1 hour the forecast is better than persistence. For forecast horizons of more

than two days, climate averages show lower errors and should be preferred for diffuse solar radiationprediction.

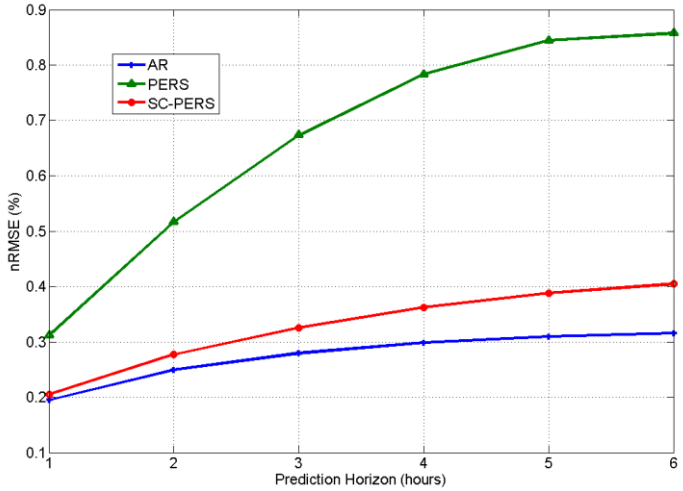

Fig. 2. Relative RMSE of forecasts (persistence, auto regression, and scaled persistence) and of reference models depending on the forecast horizon Lauret *et al.* [27].

Classically, a comparison of performance is performed with a reference computing model and to do it, a skill factor is employed. The skill factor or skill score defines the difference between the forecast and the reference forecast normalized by the difference between a perfect and the reference forecast Lauret *et al.* [27]:

$$SkillScore = \frac{Metric_{forecasted} - Metric_{reference}}{Metric_{perfectfoœcast} - Metric_{reference}} = 1 - \frac{MSE_{forecatd}}{MSE_{reference}} \quad (12)$$

Its value thus ranges between 1 (perfect forecast) and 0 (reference forecast). A negative value indicates a performance which is even worse compared to the reference (observed data). Skill scores can be adopted not only for comparison between observed and predicted diffuse solar radiation values but also for inter-comparisons of different diffuse solar radiation prediction techniques.

4. Regression Models

A regression model relates diffuse solar radiation (H_d) with other easily measurable parameters such as clearness index, mean daily extraterrestrial solar radiation, sunshine fraction and cloud cover by applying concise mathematical functions. As a result of its simplicity and high operability, the regression model is much more convenient for engineering applications.

Several regression models have been reported in literature for prediction H_d on the horizontal surface either on hourly mean basis (HB) or daily mean basis (DB) or monthly mean daily basis (MB) in Nigeria and Egypt. In this review, the H_d models are classified according to the basis of their input parameters applied in correlating with either diffuse fraction (H_d/H) or diffuse coefficient (H_d/H_o).

It has been accepted that H_d is relatively affected by meteorological parameters, astronomical factors, geographical factors, and geometrical factors [7, 9, 28-29]. This could be attributed to the uniqueness of local climate in determining the meteorological and

atmospheric parameters that best fit that particular locality. This also depends on the availability of input meteorological/atmospheric parameter(s) that a given radiometric station or an individual is capable of measuring routinely which finally turns out to be the best input parameter at the disposal of the researcher for predicting H_d in that location factors [7, 9]. Thus, in North-Western Africa, the models for predicting H_d can be classified into six (6) following categories based on the employed meteorological and atmospheric parameters via:

1. Clearness index-based models
2. Sunshine-based models
3. Cloud-based models
4. Extraterrestrial Solar Radiation-based models
5. Monthly-based models
6. Hybrid Parameter-based models

4.1 Clearness Index-Based Models

The clearness index (k_t) indicates the percentage depletion by the sky of the incoming solar radiation and therefore gives both the level of availability of solar radiation and changes in the atmospheric condition in a given environment [8, 30-32]. Mathematically, clearness index is the ratio of horizontal global solar radiation to the extraterrestrial solar radiation (H_o) on daily or monthly basis as found in literature expressed as:

$$k_t = \frac{H}{H_o} \tag{13}$$

For this reason, clearness index is closed related to H_d, hence, it has been known as a determinant parameter for estimation of H_d. One of the greatest characteristics of the models from this class is their convenient application, since for utilizing them only measured H data is needed. Numerous functional forms (exponential form, logistic form, logarithm form, second order, third order and power form) have been applied for estimating HB, DB and MB diffuse horizontal irradiation in literature are introduced according to their developing year under this section.

4.1.1 Group 1

Empirical models from this group are parameterized as the first-order polynomial function of the clearness index according to their functional forms and developing year. The functional forms are as follows:

$$\frac{H_d}{H_o} = a + b\left(\frac{H}{H_o}\right) \tag{14}$$

$$\frac{H_d}{H} = a + b\left(\frac{H}{H_o}\right) \tag{15}$$

$$\frac{H_d}{H} = a + b\left(\frac{H}{H_o}\right)^{-1} \tag{16}$$

$$H_d = a + b\left(\frac{H}{H_o}\right) \tag{17}$$

Ezekwe and Ezeilo [33] developed the following MB models in Nsukka

For January to May

$$\frac{H_d}{H} = 1.13 - 1.48\left(\frac{H}{H_o}\right) \quad (18a)$$

For dry season

$$\frac{H_d}{H} = 1.14 - 1.69\left(\frac{H}{H_o}\right) \quad (18b)$$

Said and Ibrahim [34] developed the following MB model for Cairo, Egypt as:

$$\frac{H_d}{H} = 0.86 - 0.86\left(\frac{H}{H_o}\right) \quad (19)$$

Maduekwe and Chendo [35] developed HB diffuse solar radiation for Lagos as:

$$\frac{H_d}{H} = 1.021 - 0.151\left(\frac{H}{H_o}\right) \qquad 0 \le \left(\frac{H}{H_o}\right) \le 0.30 \quad (20a)$$

$$\frac{H_d}{H} = 1.385 - 1.396\left(\frac{H}{H_o}\right) \qquad 0.30 < \left(\frac{H}{H_o}\right) < 0.80 \quad (20b)$$

Babatunde and Aro [36] established the following MB model for Ilorin as:

$$\frac{H_d}{H} = 0.945 - 0.97\left(\frac{H}{H_o}\right) \quad (21)$$

Maduekwe and Chendo [37] proposed the following HB models for Lagos

$$\frac{H_d}{H} = 1.021 - 1.151\left(\frac{H}{H_o}\right) \qquad 0 \le \left(\frac{H}{H_o}\right) \le 0.30 \quad (22a)$$

$$\frac{H_d}{H} = 1.385 - 1.396\left(\frac{H}{H_o}\right) \qquad 0.30 < \left(\frac{H}{H_o}\right) < 0.80 \quad (22b)$$

Trabea [38] obtained the following MB model for AL-Arish, AL-Tahrir, Marsa Matroh, Cairo, Al-Kharga and Aswan located in Egypt as:

$$\frac{H_d}{H} = 0.924 - 0.894\left(\frac{H}{H_o}\right) \quad (23)$$

Maduekwe and Garba [39] developed the following HB models for Lagos and Zaria with the appropriate intervals as:

For Zaria

$$\frac{H_d}{H} = 1.009 - 0.273\left(\frac{H}{H_o}\right) \qquad \left(\frac{H}{H_o}\right) \le 0.18 \quad (24a)$$

$$\frac{H_d}{H} = 1.077 - 1.136\left(\frac{H}{H_o}\right) \qquad 0.18 < \left(\frac{H}{H_o}\right) < 0.68 \quad (24b)$$

For Lagos

$$\frac{H_d}{H} = 1.002 - 0.028\left(\frac{H}{H_o}\right) \qquad \left(\frac{H}{H_o}\right) \le 0.20 \quad (24c)$$

$$\frac{H_d}{H} = 1.336 - 1.369\left(\frac{H}{H_o}\right) \qquad 0.20 < \left(\frac{H}{H_o}\right) < 0.78 \quad (24d)$$

Shaltout *et al.* [40] developed the following MB models for Cario and Aswan in Egypt.

For Cario

$$\frac{H_d}{H} = 0.93 - 1.08\left(\frac{H}{H_o}\right) \quad (25a)$$

For Aswan

$$\frac{H_d}{H} = 1.01 - 1.16\left(\frac{H}{H_o}\right) \quad (25b)$$

El-Sebaii and Trabea [41] developed the following MB models for four Egyptian locations' For Matruh

$$\frac{H_d}{H} = 1.299 - 1.435\left(\frac{H}{H_o}\right) \quad (26a)$$

For Al-Arish

$$\frac{H_d}{H} = 1.377 - 1.550\left(\frac{H}{H_o}\right) \quad (26b)$$

For Rafah

$$\frac{H_d}{H} = 1.257 - 1.531\left(\frac{H}{H_o}\right) \quad (26c)$$

For Aswan

$$\frac{H_d}{H} = 0.580 - 0.339\left(\frac{H}{H_o}\right) \quad (26d)$$

Burari [42] developed the following MB models for Bauchi as follows:

$$\frac{H_d}{H} = 0.775 - 0.804\left(\frac{H}{H_o}\right) \quad (27)$$

Ugwuoke and Okeke [43] developed the following models for Nsukka as:

$$H_d = 0.137255 - 0.1143\left(\frac{H}{H_o}\right) \quad (28)$$

Khalil and Shaffie [44] established the following HB models for Cario, Egypt as:

$$\frac{H_d}{H} = 5.817 - 6.517\left(\frac{H}{H_o}\right) \quad (29)$$

Okundamiya *et al.* [45] established the following MB models for six Nigerian locations For Sokoto

$$\frac{H_d}{H} = 1.0658 - 1.2566\left(\frac{H}{H_o}\right) \quad (30a)$$

For Maiduguri

$$\frac{H_d}{H} = 1.0600 - 1.2526\left(\frac{H}{H_o}\right) \quad (30b)$$

For Abuja

$$\frac{H_d}{H} = 1.0506 - 1.2461\left(\frac{H}{H_o}\right) \quad (30c)$$

For Ikeja

$$\frac{H_d}{H} = 1.0467 - 1.2461\left(\frac{H}{H_o}\right) \quad (30d)$$

For Enugu

$$\frac{H_d}{H} = 1.0454 - 1.2467\left(\frac{H}{H_o}\right) \quad (30e)$$

For Benin City

$$\frac{H_d}{H} = 1.0387 - 1.2419\left(\frac{H}{H_o}\right) \quad (30f)$$

Nwokolo and Ogbulezie [10] developed the following MB models for all sky and clear sky in numerous stations in six tropical ecological zones in Nigeria.

For Port Harcourt (All sky)

$$H_d = 14.273 - 13.50\left(\frac{H}{H_o}\right) \quad (31a)$$

For Port Harcourt (Clear sky)

$$H_d = -1.874 + 16.922\left(\frac{H}{H_o}\right) \quad (31b)$$

For Owerri (All sky)

$$H_d = 10.814 - 7.031\left(\frac{H}{H_o}\right) \quad (31c)$$

For Owerri (Clear Sky)

$$H_d = -5.400 + 23.21\left(\frac{H}{H_o}\right) \quad (31d)$$

For Ibadan (All sky)

$$H_d = 12.059 - 9.542\left(\frac{H}{H_o}\right) \quad (31e)$$

For Ibadan (Clear Sky)

$$H_d = -7.4955 + 26.902\left(\frac{H}{H_o}\right) \quad (31f)$$

For Abuja (All sky)

$$H_d = 14.076 - 13.008\left(\frac{H}{H_o}\right) \quad (31g)$$

For Abuja (clear sky)

$$H_d = 35.705 - 49.757\left(\frac{H}{H_o}\right) \quad (31h)$$

For Maiduguri (All sky)

$$H_d = 18.049 - 19.256\left(\frac{H}{H_o}\right) \quad (31i)$$

For Maiduguri (clear sky)

$$H_d = 33.121 - 45.136\left(\frac{H}{H_o}\right) \quad (31j)$$

For Sokoto (All sky)

$$H_d = 19.008 - 20.404\left(\frac{H}{H_o}\right) \quad (31k)$$

For Sokoto (Clear sky)

$$H_d = 7.8579 - 3.1059\left(\frac{H}{H_o}\right) \quad (31L)$$

4.1.2. Group 2

Empirical models from this group are parameterized as the second-order polynomial function of the clearness index according to their functional forms and developing year. The functional forms are as follows:

$$\frac{H_d}{H} = a + b\left(\frac{H}{H_o}\right) + c\left(\frac{H}{H_o}\right)^2 \quad (32)$$

Trabea [38] obtained the following MB model for AL-Arish, AL-Tahrir, Marsa Matroh, Cairo, Al-Kharga and Aswan located in Egypt as:

$$\frac{H_d}{H} = 0.534 + 0.384\left(\frac{H}{H_o}\right) - 1.0366\left(\frac{H}{H_o}\right)^2 \quad (33)$$

El-Sebaii and Trabea [41] developed the following MB models for four Egyptian locations'
For Matruh

$$\frac{H_d}{H} = -4.914 + 18.170\left(\frac{H}{H_o}\right) - 15.439\left(\frac{H}{H_o}\right)^2 \quad (34a)$$

For Al-Arish

$$\frac{H_d}{H} = -4.138 + 16.540\left(\frac{H}{H_o}\right) - 14.778\left(\frac{H}{H_o}\right)^2 \quad (34b)$$

For Rafah

$$\frac{H_d}{H} = 2.635 - 5.652\left(\frac{H}{H_o}\right) + 3.312\left(\frac{H}{H_o}\right)^2 \quad (34c)$$

For Aswan

$$\frac{H_d}{H} = 10.45 - 29.47\left(\frac{H}{H_o}\right) + 21.459\left(\frac{H}{H_o}\right)^2 \quad (34d)$$

Burari [42] developed the following MB models for Bauchi as follows:

$$\frac{H_d}{H} = 0.908 - 1.31\left(\frac{H}{H_o}\right) + 0.474\left(\frac{H}{H_o}\right)^2 \quad (35)$$

Okundamiya and Nzeako [46] developed the following MB models for selected cities in Nigeria
For Abuja

$$\frac{H_d}{H} = 0.8733 - 0.5902\left(\frac{H}{H_o}\right) - 0.583\left(\frac{H}{H_o}\right)^2 \quad (36a)$$

For Benin City

$$\frac{H_d}{H} = 0.9467 - 0.809\left(\frac{H}{H_o}\right) - 0.4755\left(\frac{H}{H_o}\right)^2 \quad (36b)$$

For Katisna

$$\frac{H_d}{H} = 3.031 - 7.64\left(\frac{H}{H_o}\right) - 5.166\left(\frac{H}{H_o}\right)^2 \quad (36c)$$

Sanusi and Abisoye [47] proposed the following MB models for Lagos, Nigeria as:

$$\frac{H_d}{H} = 0.9676 - 1.2654\left(\frac{H}{H_o}\right) + 0.3199\left(\frac{H}{H_o}\right)^2 \quad (37)$$

Okundamiya *et al.* [45] established the following MB models for six Nigerian locations
For Sokoto

$$\frac{H_d}{H} = 1.1198 - 1.4433\left(\frac{H}{H_o}\right) + 0.1600\left(\frac{H}{H_o}\right)^2 \quad (38a)$$

For Maiduguri

$$\frac{H_d}{H} = 0.7087 - 0.0103\left(\frac{H}{H_o}\right) - 1.0845\left(\frac{H}{H_o}\right)^2 \quad (38b)$$

For Abuja

$$\frac{H_d}{H} = 0.8994 - 0.6674\left(\frac{H}{H_o}\right) - 0.5466\left(\frac{H}{H_o}\right)^2 \quad (38c)$$

For Ikeja

$$\frac{H_d}{H} = 0.9225 - 0.7240\left(\frac{H}{H_o}\right) - 0.5340\left(\frac{H}{H_o}\right)^2 \quad (38d)$$

For Enugu

$$\frac{H_d}{H} = 0.9571 - 0.8786\left(\frac{H}{H_o}\right) - 0.3753\left(\frac{H}{H_o}\right)^2 \quad (38e)$$

For Benin City

$$\frac{H_d}{H} = 0.9994 - 1.0627\left(\frac{H}{H_o}\right) - 0.1983\left(\frac{H}{H_o}\right)^2 \quad (38f)$$

Nwokolo and Ogbulezie [10] developed the following MB models for all sky and clear sky in several locations in six tropical ecological zones in Nigeria.
For Port Harcourt (All Sky)

$$\frac{H_d}{H} = 1.011 - 1.091\left(\frac{H}{H_o}\right) - 0.195\left(\frac{H}{H_o}\right)^2 \quad (39a)$$

For Port Harcourt (Clear Sky)

$$\frac{H_d}{H} = -34.62 + 122.42\left(\frac{H}{H_o}\right) - 106.44\left(\frac{H}{H_o}\right)^2 \quad (39b)$$

For Owerri (All Sky)

$$\frac{H_d}{H} = 0.987 - 1.003\left(\frac{H}{H_o}\right) - 0.257\left(\frac{H}{H_o}\right)^2 \quad (39c)$$

For Owerri (Clear Sky)

$$\frac{H_d}{H} = -13.81 + 47.749\left(\frac{H}{H_o}\right) - 39.80\left(\frac{H}{H_o}\right)^2 \quad (39d)$$

For Ibadan (All Sky)

$$\frac{H_d}{H} = 0.942 - 0.825\left(\frac{H}{H_o}\right) - 0.447\left(\frac{H}{H_o}\right)^2 \quad (39e)$$

For Ibadan (Clear Sky)

$$\frac{H_d}{H} = 20.86 - 77.77\left(\frac{H}{H_o}\right) - 73.75\left(\frac{H}{H_o}\right)^2 \quad (39f)$$

For Abuja (All Sky)

$$\frac{H_d}{H} = 0.981 - 1.020\left(\frac{H}{H_o}\right) - 0.195\left(\frac{H}{H_o}\right)^2 \quad (39g)$$

For Abuja (Clear Sky)

$$\frac{H_d}{H} = -49.95 + 175.55\left(\frac{H}{H_o}\right) - 153.0\left(\frac{H}{H_o}\right)^2 \quad (39h)$$

For Maiduguri (All Sky)

$$\frac{H_d}{H} = 0.907 - 0.721\left(\frac{H}{H_o}\right) - 0.456\left(\frac{H}{H_o}\right)^2 \quad (39i)$$

For Maiduguri (Clear Sky)

$$\frac{H_d}{H} = 29.75 - 96.05\left(\frac{H}{H_o}\right) + 78.178\left(\frac{H}{H_o}\right)^2 \quad (39j)$$

For Sokoto (All Sky)

$$\frac{H_d}{H} = 2.132 - 4.750\left(\frac{H}{H_o}\right) - 2.852\left(\frac{H}{H_o}\right)^2 \quad (39k)$$

For Sokoto (Clear Sky)

$$\frac{H_d}{H} = 0.678 - 1.082\left(\frac{H}{H_o}\right) + 0.001\left(\frac{H}{H_o}\right)^2 \quad (39L)$$

4.1.3. Group 3

Empirical models from this group are parameterized as the third-order polynomial function of the clearness index according to their functional forms and developing year. The functional forms are as follows:

$$\frac{H_d}{H} = a + b\left(\frac{H}{H_o}\right) + c\left(\frac{H}{H_o}\right)^2 + d\left(\frac{H}{H_o}\right)^3 \quad (40)$$

Said and Ibrahim [34] developed the following MB model for Cairo, Egypt as:

$$\frac{H_d}{H} = 0.636 - 0.279\left(\frac{H}{H_o}\right) - 0.194\left(\frac{H}{H_o}\right)^2 - 0.383\left(\frac{H}{H_o}\right)^3 \quad (41)$$

El-Sebaii and Trabea [41] developed the following MB models for four Egyptian locations' For Matruh

$$\frac{H_d}{H} = 113.3 - 540.92\left(\frac{H}{H_o}\right) - 564.79\left(\frac{H}{H_o}\right)^2 + 461.38\left(\frac{H}{H_o}\right)^3 \quad (42a)$$

For Rafah

$$\frac{H_d}{H} = 6.140 - 22.58\left(\frac{H}{H_o}\right) + 30.519\left(\frac{H}{H_o}\right)^2 - 14.543\left(\frac{H}{H_o}\right)^3 \quad (42b)$$

For Aswan

$$\frac{H_d}{H} = -65.81 - 306.75\left(\frac{H}{H_o}\right) - 472.70\left(\frac{H}{H_o}\right)^2 + 241.42\left(\frac{H}{H_o}\right)^3 \quad (42c)$$

Olopade and Sanusi [48] developed the following MB model for Ilorin as:

$$\frac{H_d}{H} = 0.910 + 1.154\left(\frac{H}{H_o}\right) - 4.936\left(\frac{H}{H_o}\right)^2 + 2.848\left(\frac{H}{H_o}\right)^3 \qquad 0.1 \le \left(\frac{H}{H_o}\right) \le 0.7 \quad (43)$$

Okundamiya *et al.* [45] established the following MB models for six Nigerian locations For Sokoto

$$\frac{H_d}{H} = 2.1699 - 6.9082\left(\frac{H}{H_o}\right) + 9.592\left(\frac{H}{H_o}\right)^2 - 5.4009\left(\frac{H}{H_o}\right)^3 \quad (44a)$$

For Maiduguri

$$\frac{H_d}{H} = 7.3138 - 35.4344\left(\frac{H}{H_o}\right) + 61.7977\left(\frac{H}{H_o}\right)^2 - 36.9520\left(\frac{H}{H_o}\right)^3 \quad (44b)$$

For Abuja

$$\frac{H_d}{H} = 2.7317 - 11.346\left(\frac{H}{H_o}\right) + 19.9398\left(\frac{H}{H_o}\right)^2 - 12.9301\left(\frac{H}{H_o}\right)^3 \quad (44c)$$

For Ikeja

$$\frac{H_d}{H} = 2.3663 - 9.8575\left(\frac{H}{H_o}\right) + 18.4150\left(\frac{H}{H_o}\right)^2 - 12.90721\left(\frac{H}{H_o}\right)^3 \quad (44d)$$

For Enugu

$$\frac{H_d}{H} = 2.5887 - 11.1174\left(\frac{H}{H_o}\right) + 20.7699\left(\frac{H}{H_o}\right)^2 - 14.3774\left(\frac{H}{H_o}\right)^3 \quad (44e)$$

For Benin City

$$\frac{H_d}{H} = 2.3880 - 10.5426\left(\frac{H}{H_o}\right) + 21.0098\left(\frac{H}{H_o}\right)^2 - 15.5605\left(\frac{H}{H_o}\right)^3 \quad (44f)$$

4.1.4. Group 4

Empirical models from this group are parameterized as the four-order polynomial function of the clearness index according to their functional forms and developing year. The functional forms are as follows:

$$\frac{H_d}{H} = a + b\left(\frac{H}{H_o}\right) + c\left(\frac{H}{H_o}\right)^2 + d\left(\frac{H}{H_o}\right)^3 + e\left(\frac{H}{H_o}\right)^4 \quad (45)$$

Bamiro [49] developed the following HB models for Nsukka as:

$$\frac{H_d}{H} = 1.0 - 0.2727\left(\frac{H}{H_o}\right) + 2.4495\left(\frac{H}{H_o}\right)^2 - 11.9514\left(\frac{H}{H_o}\right)^3 + 9.3879\left(\frac{H}{H_o}\right)^4 \left(\frac{H}{H_o}\right) < 0.715$$

(46a)

$$\frac{H_d}{H} = 1.0 + 0.2832\left(\frac{H}{H_o}\right) - 2.555\left(\frac{H}{H_o}\right)^2 + 0.8448\left(\frac{H}{H_o}\right)^3 + 9.3879\left(\frac{H}{H_o}\right)^4 \quad \left(\frac{H}{H_o}\right) < 0.722$$

(46b)

4.1.5 Group 5

In this sub-class, exponential form of diffuse fraction was correlated with clearness index in forms:

$$\frac{H_d}{H} = a\exp^{b\left(H/H_o\right)} \quad (47)$$

Sanusi and Abisoye [47] proposed the following MB models for Lagos, Nigeria as:

$$\frac{H_d}{H} = 1.2313\exp^{-2.2\left(H/H_o\right)} \quad (48)$$

4.1.6 Group 6

In this sub-class, Liu and Jordan type model was modified by correlating diffuse fraction with power form of clearness index in the form:

$$\frac{H_d}{H} = a\left(\frac{H}{H_o}\right)^b \quad (49)$$

Sanusi and Abisoye [47] proposed the following MB models for Lagos, Nigeria as:

$$\frac{H_d}{H} = 0.2\left(\frac{H}{H_o}\right)^{-1.012} \quad (50)$$

4.2 Sunshine-Based Models

Sunshine-based models are the most frequently employed model for predicting diffuse solar radiation in Nigeria and Egypt as a result of its availability and reliable measured data in most meteorological stations in Nigeria and Egypt. This radiometric model modified from Liu and Jordan [11] model have been applied by countless number of researchers for predicting the hourly, daily and monthly mean daily diffuse solar radiation on the horizontal surface for several stations within Nigeria and Egypt and beyond by employing meteorological parameters of the site of interest as stated in this class. Thus, the relation is given as:

$$\frac{H}{H_o} = a + b\left(\frac{S}{S_o}\right) \tag{51}$$

Where a and b are the empirical constants, S is the measure of sunshine duration and S_o is the daily maximum possible sunshine duration.

4.2.1 Group 1

Empirical models from this group are parameterized as the first-order polynomial function of the sunshine fraction according to their functional forms and developing year. The functional forms are as follows:

$$\frac{H_d}{H} = a + b\left(\frac{S}{S_o}\right) \tag{52}$$

$$\frac{H_d}{H_o} = a + b\left(\frac{S}{S_o}\right) \tag{53}$$

Said and Ibrahim [34] developed the following MB model for Cairo, Egypt as:

$$\frac{H_d}{H} = 0.79 - 0.59\left(\frac{S}{S_o}\right) \tag{54}$$

Maduekwe and Chendo [37] developed the following DB and MB models for Lagos.
For DB

$$\frac{H_d}{H_o} = -0.012 + 0.46\left(\frac{S}{S_o}\right) \tag{55a}$$

$$\frac{H_d}{H} = 0.078 + 0.58\left(\frac{S}{S_o}\right) \tag{55b}$$

For MB

$$\frac{H_d}{H} = 0.82 - 0.39\left(\frac{S}{S_o}\right) \tag{55c}$$

Trabea [38] obtained the following MB model for AL-Arish, AL-Tahrir, Marsa Matroh, Cairo, Al-Kharga and Aswan located in Egypt as:

$$\frac{H_d}{H} = 0.896 - 0.688\left(\frac{S}{S_o}\right) \tag{56}$$

El-Sebaii and Trabea [41] developed the following MB models for four Egyptian locations'
For Matruh

$$\frac{H_d}{H} = 0.618 - 0.335\left(\frac{S}{S_o}\right) \quad (57a)$$

$$\frac{H_d}{H_o} = 0.352 - 0.154\left(\frac{S}{S_o}\right) \quad (57b)$$

For Al-Arish

$$\frac{H_d}{H} = 0.941 - 0.683\left(\frac{S}{S_o}\right) \quad (57c)$$

$$\frac{H_d}{H_o} = 0.463 - 0.271\left(\frac{S}{S_o}\right) \quad (57d)$$

For Rafah

$$\frac{H_d}{H} = 0.730 - 0.433\left(\frac{S}{S_o}\right) \quad (57e)$$

$$\frac{H_d}{H_o} = 0.378 - 0.171\left(\frac{S}{S_o}\right) \quad (57f)$$

For Aswan

$$\frac{H_d}{H} = 0.886 - 0.618\left(\frac{S}{S_o}\right) \quad (57g)$$

$$\frac{H_d}{H_o} = 0.627 - 0.453\left(\frac{S}{S_o}\right) \quad (57h)$$

Khalil and Shaffie [44] established the following HB models for Cario, Egypt as:

$$\frac{H_d}{H} = 8.342 - 6.455\left(\frac{S}{S_o}\right) \quad (58a)$$

$$\frac{H_d}{H_o} = 3.815 - 5.319\left(\frac{S}{S_o}\right) \quad (58b)$$

4.2.2 Group 2

Empirical models from this group are parameterized as the second-order polynomial function of the sunshine fraction according to their functional forms and developing year. The functional forms are as follows:

$$\frac{H_d}{H_o} = a + b\left(\frac{S}{S_o}\right) + c\left(\frac{S}{S_o}\right)^2 \quad (59a)$$

$$\frac{H_d}{H} = a + b\left(\frac{S}{S_o}\right) + c\left(\frac{S}{S_o}\right)^2 \quad (59b)$$

Said and Ibrahim [34] developed the following MB model for Cairo, Egypt as:

$$\frac{H_d}{H_o} = 0.252 - 0.0001\left(\frac{S}{S_o}\right) - 0.083\left(\frac{S}{S_o}\right)^2 \quad (60)$$

Maduekwe and Chendo [37] developed the following DB and MB models for Lagos.
For DB

$$\frac{H_d}{H_o} = 0.018 + 0.30\left(\frac{S}{S_o}\right) + 0.167\left(\frac{S}{S_o}\right)^2 \quad (61a)$$

$$\frac{H_d}{H} = 0.083 + 0.56\left(\frac{S}{S_o}\right) + 0.029\left(\frac{S}{S_o}\right)^2 \quad (61b)$$

For MB

$$\frac{H_d}{H_o} = 0.384 - 0.25\left(\frac{S}{S_o}\right) + 0.31\left(\frac{S}{S_o}\right)^2 \quad (61c)$$

$$\frac{H_d}{H} = 0.824 - 0.55\left(\frac{S}{S_o}\right) + 0.377\left(\frac{S}{S_o}\right)^2 \quad (61d)$$

Trabea [38] obtained the following MB model for AL-Arish, AL-Tahrir, Marsa Matroh, Cairo, Al-Kharga and Aswan located in Egypt as:

$$\frac{H_d}{H} = 0.839 - 0.537\left(\frac{S}{S_o}\right) - 0.098\left(\frac{S}{S_o}\right)^2 \quad (62a)$$

$$\frac{H_d}{H_o} = 0.101 + 1.092\left(\frac{S}{S_o}\right) - 0.854\left(\frac{S}{S_o}\right)^2 \quad (62b)$$

$$\frac{H_d}{H_o} = -7.0744 + 31.4386\left(\frac{S}{S_o}\right) - 15.5906\left(\frac{S}{S_o}\right)^2 \qquad 0.6 \le \left(\frac{H}{H_o}\right) \le 0.8 \quad (62c)$$

El-Sebaii and Trabea [41] developed the following MB models for four Egyptian locations' For Matruh

$$\frac{H_d}{H} = 0.113 + 1.198\left(\frac{S}{S_o}\right) - 1.116\left(\frac{S}{S_o}\right)^2 \quad (63a)$$

$$\frac{H_d}{H_o} = -0.012 + 0.948\left(\frac{S}{S_o}\right) - 0.802\left(\frac{S}{S_o}\right)^2 \quad (63b)$$

For Al-Arish

$$\frac{H_d}{H} = -1.888 + 6.999\left(\frac{S}{S_o}\right) - 5.144\left(\frac{S}{S_o}\right)^2 \quad (63c)$$

$$\frac{H_d}{H_o} = -1.353 + 4.659\left(\frac{S}{S_o}\right) - 3.301\left(\frac{S}{S_o}\right)^2 \quad (63d)$$

For Rafah

$$\frac{H_d}{H} = -2.053 + 7.440\left(\frac{S}{S_o}\right) - 5.468\left(\frac{S}{S_o}\right)^2 \quad (63e)$$

$$\frac{H_d}{H_o} = -1.052 + 3.875\left(\frac{S}{S_o}\right) - 2.810\left(\frac{S}{S_o}\right)^2 \quad (63f)$$

For Aswan

$$\frac{H_d}{H} = 3.431 - 6.602\left(\frac{S}{S_o}\right) + 3.506\left(\frac{S}{S_o}\right)^2 \quad (63g)$$

$$\frac{H_d}{H_o} = 1.665 - 2.892\left(\frac{S}{S_o}\right) + 1.429\left(\frac{S}{S_o}\right)^2 \quad (63h)$$

4.2.3 Group 3

Empirical models from this group are parameterized as the third-order polynomial function of the sunshine fraction according to their functional forms and developing year. The functional forms are as follows:

$$\frac{H_d}{H} = a + b\left(\frac{S}{S_o}\right) + c\left(\frac{S}{S_o}\right)^2 + d\left(\frac{S}{S_o}\right)^3 \quad (64)$$

$$\frac{H_d}{H_o} = a + b\left(\frac{S}{S_o}\right) + c\left(\frac{S}{S_o}\right)^2 + d\left(\frac{S}{S_o}\right)^3 \quad (65)$$

El-Sebaii and Trabea [41] developed the following MB models for four Egyptian locations' For Matruh

$$\frac{H_d}{H} = 0.148 - 0.126\left(\frac{S}{S_o}\right) - 0.862\left(\frac{S}{S_o}\right)^2 + 1.031\left(\frac{S}{S_o}\right)^3 \quad (66a)$$

$$\frac{H_d}{H_o} = -0.622 + 3.813\left(\frac{S}{S_o}\right) - 5.165\left(\frac{S}{S_o}\right)^2 + 2.159\left(\frac{S}{S_o}\right)^3 \quad (66b)$$

For Al-Arish

$$\frac{H_d}{H} = -19.58 + 79.25\left(\frac{S}{S_o}\right) - 102.89\left(\frac{S}{S_o}\right)^2 + 43.79\left(\frac{S}{S_o}\right)^3 \quad (66c)$$

$$\frac{H_d}{H_o} = -17.32 + 69.89\left(\frac{S}{S_o}\right) - 91.55\left(\frac{S}{S_o}\right)^2 + 39.53\left(\frac{S}{S_o}\right)^3 \quad (66d)$$

For Rafah

$$\frac{H_d}{H} = 4.129 - 19.02\left(\frac{S}{S_o}\right) + 31.94\left(\frac{S}{S_o}\right)^2 - 17.47\left(\frac{S}{S_o}\right)^3 \quad (66e)$$

$$\frac{H_d}{H_o} = -1.293 + 4.903\left(\frac{S}{S_o}\right) - 4.263\left(\frac{S}{S_o}\right)^2 + 0.679\left(\frac{S}{S_o}\right)^3 \quad (66f)$$

For Aswan

$$\frac{H_d}{H} = -24.32 + 90.86\left(\frac{S}{S_o}\right) - 110.38\left(\frac{S}{S_o}\right)^2 + 44.281\left(\frac{S}{S_o}\right)^3 \quad (66g)$$

$$\frac{H_d}{H_o} = -17.95 + 65.10\left(\frac{S}{S_o}\right) - 79.07\left(\frac{S}{S_o}\right)^2 + 31.299\left(\frac{S}{S_o}\right)^3 \quad (66h)$$

Okundamiya *et al.* [45] established the following MB models for six Nigerian locations
For Sokoto

$$\frac{H_d}{H_o} = 0.6923 - 1.4582\left(\frac{S}{S_o}\right) + 1.2132\left(\frac{S}{S_o}\right)^2 - 0.2869\left(\frac{S}{S_o}\right)^3 \quad (67a)$$

For Maiduguri

$$\frac{H_d}{H_o} = 0.6226 - 1.2632\left(\frac{S}{S_o}\right) + 1.0499\left(\frac{S}{S_o}\right)^2 - 0.2354\left(\frac{S}{S_o}\right)^3 \quad (67b)$$

For Abuja

$$\frac{H_d}{H_o} = 0.1485 - 2.2775\left(\frac{S}{S_o}\right) + 4.3429\left(\frac{S}{S_o}\right)^2 + 2.4702\left(\frac{S}{S_o}\right)^3 \quad (67c)$$

For Ikeja

$$\frac{H_d}{H_o} = -1.2813 + 13.4719\left(\frac{S}{S_o}\right) - 39.3713\left(\frac{S}{S_o}\right)^2 + 37.1341\left(\frac{S}{S_o}\right)^3 \quad (67d)$$

For Enugu

$$\frac{H_d}{H_o} = 0.1179 + 0.7339\left(\frac{S}{S_o}\right) - 1.5841\left(\frac{S}{S_o}\right)^2 + 0.9322\left(\frac{S}{S_o}\right)^3 \quad (67e)$$

For Benin City

$$\frac{H_d}{H_o} = 0.2015 + 0.0459\left(\frac{S}{S_o}\right) + 0.1159\left(\frac{S}{S_o}\right)^2 - 0.4154\left(\frac{S}{S_o}\right)^3 \quad (67f)$$

4.3 Cloud Cover-Based models

Cloud cover as a climate variable is the fraction of the sky obscured by clouds when observed from a given locality. Cloud cover data are periodically obtained from meteorological stations or satellites-derived and are expressed in percent (%) of the maximum cloud amount. Cloud amount is mostly classified into several categories of 0 – 24%, 25 – 49%, 50 – 74% and 75 – 100%. The implication is that zero percent implies no visible cloud in the sky while hundred percent cloud amount indicates no clear sky is visible. Researchers in the domain of renewable energy in the past have investigated and simulated regression computing models to relate cloud amount conditions and diffuse solar radiation owing to the fact that as diffuse fraction or diffuse coefficient increases, clouds cover increases as well. This is because of the absorption of water vapour's waveband selective in the solar spectrum that is, in cloudy and humid conditions, the absorption of solar radiation in the infrared portion of the solar spectrum is enhanced whereas absorption in

the diffuse solar radiation waveband does not vary significantly as shown in the relations below.

4.3.1. Group 1

Empirical models from this group are parameterized as the first-order polynomial function of the diffuse fraction or diffuse coefficient with cloud cover (C) or cloudiness index according to their functional forms and developing year. The functional forms are as follows:

$$\frac{H_d}{H} = a + b(C) \tag{68}$$

$$\frac{H_d}{H} = a + b\left(\frac{C}{8}\right) \tag{69}$$

$$\frac{H_d}{H_o} = a + b\left(\frac{C}{8}\right) \tag{70}$$

Erusiafe and Chendo [50] developed HB model for Lagos as:

$$\frac{H_d}{H} = -0.0859 + 1.316(C) \tag{71}$$

Okundamiya *et al.* [45] established the following MB models for six Nigerian locations

For Sokoto

$$\frac{H_d}{H} = 0.1505 - 0.0439(C) \tag{72a}$$

For Maiduguri

$$\frac{H_d}{H} = 0.1202 - 0.0528(C) \tag{72b}$$

For Abuja

$$\frac{H_d}{H} = 0.1052 - 0.0614(C) \tag{72c}$$

For Ikeja

$$\frac{H_d}{H} = 0.0792 - 0.0706(C) \tag{72d}$$

For Enugu

$$\frac{H_d}{H} = 0.0888 - 0.0669(C) \tag{72e}$$

For Benin City

$$\frac{H_d}{H} = 0.0761 - 0.0759(C) \tag{72f}$$

4.4 Monthly-Based Models

Monthly-based models are applied for estimating diffuse solar radiation as a result of variation effects on diffuse solar radiation striking at ground level in a particular location due to the movement on the earth on its axis. Thus, the functional forms and models employed in Africa are introduced in this section.

4.4.1 Group 1

In this group, clearness index is corrected to month of the year (M) in the form:

$$H_d = a + b(M) + c(M)^2 + d(M)^3 \quad (73)$$

Ugwuoke and Okeke [43] developed the following models for Nsukka as:

$$H_d = 47.2667 - 6.5095(M) + 0.8832(M)^2 - 0.03918(M)^3 \quad (74)$$

4.5 Global Solar Radiation-Based models

Global solar radiation-based models are employed by solar radiation researchers for predicting diffuse solar radiation as a result of their great importance and influence for determining the diffuse solar radiation striking a particular location at the top of the atmosphere and their comprehensive impact on the diffuse solar radiation on the horizontal surface on ground level. Thus, the functional forms and models employed in Africa are presented in this section.

4.5.1 Group 1

In this group, diffuse solar radiation is correlated to global solar radiation (H) in the form:

$$H_d = a + b(H) + c(H)^2 \quad (75)$$

Ugwuoke and Okeke [43] developed the following models for Nsukka as:

$$H_d = 62.53439 - 12.75992(H) + 0.9774(H)^2 \quad (76)$$

4.6 Hybrid Parameter-based models

As far as the input parameter for predicting diffuse solar radiation on the horizontal surface vary periodically with the local climate in a particular geographical location, it therefore implies that to accurately develop a model that can fit a locality, the solar energy researcher must test the local climate with various input parameters owing to the availability of the meteorological parameters at the disposal of the researcher. Several solar energy researchers in Nigeria and Egypt have observed that hybrid parameters-based models fit local climate more than one variable – sunshine-based, global solar radiation-based and cloud cover – based commonly employed for predicting diffuse solar radiation. In this section, numerous hybrid parameter-based models are presented and classified based on their input parameters and developing year.

4.6.1 Group 1

In this group, sunshine duration and clearness index were incorporated with diffuse for estimating diffuse solar radiation in the forms:

$$\frac{H_d}{H_o} = a + b\left(\frac{H}{H_o}\right) + c\left(\frac{S}{S_o}\right) \quad (77)$$

$$\frac{H_d}{H_o} = a + b\left(\frac{H}{H_o}\right) + c\left(\frac{S}{S_o}\right) + d\left(\frac{S}{S_o}\right)^2 \quad (78)$$

$$\frac{H_d}{H_o} = a + b\left(\frac{H}{H_o}\right) + c\left(\frac{S}{S_o}\right)^2 \quad (79)$$

$$\frac{H_d}{H} = a + b\left(\frac{H}{H_o}\right) + c\left(\frac{S}{S_o}\right) \quad (80)$$

$$\frac{H_d}{H} = a + b\left(\frac{H}{H_o}\right) + c\left(\frac{S}{S_o}\right) + d\left(\frac{S}{S_o}\right)^2 \quad (81)$$

$$\frac{H_d}{H} = a + b\left(\frac{H}{H_o}\right) + c\left(\frac{S}{S_o}\right)^2 \quad (82)$$

Maduekwe and Chendo [37] developed the following DB and MB models for Lagos.
For DB

$$\frac{H_d}{H_o} = -0.241 - 0.72\left(\frac{H}{H_o}\right) - 0.16\left(\frac{S}{S_o}\right) \quad (83a)$$

$$\frac{H_d}{H_o} = -0.195 - 0.74\left(\frac{H}{H_o}\right) - 0.15\left(\frac{S}{S_o}\right) + 0.324\left(\frac{S}{S_o}\right)^2 \quad (83b)$$

$$\frac{H_d}{H_o} = -0.213 + 0.71\left(\frac{H}{H_o}\right) + 0.182\left(\frac{S}{S_o}\right)^2 \quad (83c)$$

$$\frac{H_d}{H} = -0.17 + 0.78\left(\frac{H}{H_o}\right) + 0.26\left(\frac{S}{S_o}\right) \quad (83d)$$

$$\frac{H_d}{H} = 0.136 + 0.80\left(\frac{H}{H_o}\right) + 0.03\left(\frac{S}{S_o}\right) + 0.235\left(\frac{S}{S_o}\right)^2 \quad (83e)$$

$$\frac{H_d}{H} = -0.133 + 0.81\left(\frac{H}{H_o}\right) + 0.214\left(\frac{S}{S_o}\right)^2 \quad (83f)$$

For MB

$$\frac{H_d}{H_o} = 0.372 - 0.11\left(\frac{H}{H_o}\right) + 0.06\left(\frac{S}{S_o}\right) \quad (83g)$$

$$\frac{H_d}{H_o} = 0.431 - 0.11\left(\frac{H}{H_o}\right) - 0.22\left(\frac{S}{S_o}\right) + 0.300\left(\frac{S}{S_o}\right)^2 \quad (83h)$$

$$\frac{H_d}{H_o} = 0.385 - 0.12\left(\frac{H}{H_o}\right) + 0.067\left(\frac{S}{S_o}\right)^2 \quad (83i)$$

$$\frac{H_d}{H} = 1.36 - 1.35\left(\frac{H}{H_o}\right) - 0.0012\left(\frac{S}{S_o}\right) \quad (83j)$$

$$\frac{H_d}{H} = 1.429 - 1.44\left(\frac{H}{H_o}\right) - 0.17\left(\frac{S}{S_o}\right) + 0.25\left(\frac{S}{S_o}\right)^2 \quad (83k)$$

$$\frac{H_d}{H} = 1.383 - 1.44\left(\frac{H}{H_o}\right) + 0.076\left(\frac{S}{S_o}\right)^2 \quad (83L)$$

Trabea [38] obtained the following MB model for AL-Arish, AL-Tahrir, Marsa Matroh, Cairo, Al-Kharga and Aswan located in Egypt as:

$$\frac{H_d}{H} = 0.9270 - 0.1640\left(\frac{H}{H_o}\right) - 0.5950\left(\frac{S}{S_o}\right) \quad (84)$$

Khalil and Shaffie [44] established the following HB models for Cario, Egypt as:

$$\frac{H_d}{H} = 6.314 - 5.131\left(\frac{H}{H_o}\right) + 0.136\left(\frac{S}{S_o}\right) \quad (85a)$$

$$\frac{H_d}{H_o} = 5.292 - 4.226\left(\frac{H}{H_o}\right) - 0.321\left(\frac{S}{S_o}\right) \quad (85b)$$

4.6.2 Group 2

In this group, cloud cover and clearness index were incorporated with diffuse for estimating diffuse solar radiation in the forms:

$$\frac{H_d}{H} = a + b\left(\frac{H}{H_o}\right) + c\left(\frac{C}{8}\right) \quad (86)$$

$$\frac{H_d}{H} = a + b\left(\frac{H}{H_o}\right) + c(C) \quad (87)$$

Okundamiya *et al.* [45] established the following MB models for six Nigerian locations

For Sokoto

$$\frac{H_d}{H} = -0.9347 + 0.0154\left(\frac{H}{H_o}\right) + 0.0154(C) \quad (88a)$$

For Maiduguri

$$\frac{H_d}{H} = 0.8189 - 0.940\left(\frac{H}{H_o}\right) + 0.0149(C) \quad (88b)$$

For Abuja

$$\frac{H_d}{H} = 0.8760 - 1.0222\left(\frac{H}{H_o}\right) + 0.0121(C) \quad (88c)$$

For Ikeja

$$\frac{H_d}{H} = 0.8700 - 1.0309\left(\frac{H}{H_o}\right) + 0.0142(C) \quad (88d)$$

For Enugu

$$\frac{H_d}{H} = 0.8490 - 0.9989\left(\frac{H}{H_o}\right) + 0.0445(C) \quad (88e)$$

For Benin City

$$\frac{H_d}{H} = 0.8285 - 0.9784\left(\frac{H}{H_o}\right) + 0.0172(C) \quad (88f)$$

4.6.3 Group 3

In this group, elevation and clearness index were incorporated with diffuse for estimating diffuse solar radiation in the forms:

$$\frac{H_d}{H} = a + b\left(\frac{H}{H_o}\right) + c(h) \quad (89)$$

$$\frac{H_d}{H} = a + b\left(\frac{H}{H_o}\right) + c(\sinh) \tag{90}$$

Maduekwe and Chendo [37] proposed the following HB models for Lagos

$$\frac{H_d}{H} = 1.019 - 0.159\left(\frac{H}{H_o}\right) + 0.0058(\sinh) \qquad 0 \le \left(\frac{H}{H_o}\right) \le 0.30 \tag{91a}$$

$$\frac{H_d}{H} = 1.550 - 1.469\left(\frac{H}{H_o}\right) + 0.1566(\sinh) \qquad 0.30 < \left(\frac{H}{H_o}\right) < 0.80 \tag{91b}$$

$$\frac{H_d}{H} = 0.245\left(\frac{H}{H_o}\right) + 0.085(\sinh) \tag{91c}$$

Maduekwe and Garba [39] developed the following HB models for Lagos and Zaria with the appropriate intervals as:

For Zaria

$$\frac{H_d}{H} = 1.016 - 1.203\left(\frac{H}{H_o}\right) - 0.00455(h) \qquad \left(\frac{H}{H_o}\right) \le 0.18 \tag{92a}$$

$$\frac{H_d}{H} = 0.973 - 0.546\left(\frac{H}{H_o}\right) - 0.00283(h) \qquad 0.18 < \left(\frac{H}{H_o}\right) < 0.68 \tag{92b}$$

$$\frac{H_d}{H} = 0.438\left(\frac{H}{H_o}\right) - 0.00104(h) \qquad \left(\frac{H}{H_o}\right) \ge 0.68 \tag{92c}$$

For Lagos

$$\frac{H_d}{H} = 1.007 - 0.072\left(\frac{H}{H_o}\right) - 0.000085(h) \qquad \left(\frac{H}{H_o}\right) \le 0.20 \tag{92d}$$

$$\frac{H_d}{H} = 1.36 - 1.246\left(\frac{H}{H_o}\right) - 0.00107(h) \qquad 0.20 < \left(\frac{H}{H_o}\right) < 0.78 \tag{92e}$$

$$\frac{H_d}{H} = 0.34\left(\frac{H}{H_o}\right) - 0.00206(h) \qquad \left(\frac{H}{H_o}\right) \ge 0.78 \tag{92f}$$

4.6.4 Group 4

In this group, elevation, atmospheric turbidity and clearness index were incorporated with diffuse for estimating diffuse solar radiation in the forms:

$$\frac{H_d}{H} = a + b\left(\frac{H}{H_o}\right) + c(\sinh) + d(\beta) \tag{93}$$

Maduekwe and Chendo [37] proposed the following HB models for Lagos

$$\frac{H_d}{H} = 1.018 - 0.155\left(\frac{H}{H_o}\right) + 0.0037(\sinh) + 0.0032(\beta) \qquad 0 \le \left(\frac{H}{H_o}\right) \le 0.30 \tag{94a}$$

$$\frac{H_d}{H} = 1.526 - 1.448\left(\frac{H}{H_o}\right) - 0.1679(\sinh) + 0.06704(\beta) \qquad 0.30 < \left(\frac{H}{H_o}\right) < 0.80 \tag{94b}$$

$$\frac{H_d}{H} = 0.232\left(\frac{H}{H_o}\right) + 0.0258(\sinh) + 0.24831(\beta) \qquad 0.80 \le \left(\frac{H}{H_o}\right) \tag{94c}$$

4.6.5 Group 5

In this group, solar elevation and clearness index were incorporated with diffuse for estimating diffuse solar radiation in the form:

$$\frac{H_d}{H} = a + b\left(\frac{H}{H_o}\right) + c(Se) \tag{95}$$

Maduekwe and Chendo [35] developed HB diffuse solar radiation for Lagos as:

$$\frac{H_d}{H} = 1.019 - 0.159\left(\frac{H}{H_o}\right) + 0.0058(Se) \qquad 0 \le \left(\frac{H}{H_o}\right) \le 0.30 \tag{96a}$$

$$\frac{H_d}{H} = 1.550 - 1.469\left(\frac{H}{H_o}\right) + 0.1566(Se) \qquad 0.30 < \left(\frac{H}{H_o}\right) < 0.80 \tag{96b}$$

$$\frac{H_d}{H} = 0.245\left(\frac{H}{H_o}\right) + 0.085(Se) \qquad 0.80 \le \left(\frac{H}{H_o}\right) \tag{96c}$$

4.6.6 Group 6

In this group, solar elevation, turbidity coefficients and clearness index were incorporated with diffuse for estimating diffuse solar radiation in the forms:

$$\frac{H_d}{H} = a + b\left(\frac{H}{H_o}\right) + c(Se) + d(\beta_{500}) \tag{97}$$

$$\frac{H_d}{H} = a + b\left(\frac{H}{H_o}\right) + c(Se) + d(\beta_{880}) \tag{98}$$

Maduekwe and Chendo [35] developed HB diffuse solar radiation for Lagos as:

$$\frac{H_d}{H} = 1.018 - 0.155\left(\frac{H}{H_o}\right) + 0.0037(Se) + 0.00131(\beta_{500}) \qquad 0 \le \left(\frac{H}{H_o}\right) \le 0.30 \tag{99a}$$

$$\frac{H_d}{H} = 1.526 - 1.448\left(\frac{H}{H_o}\right) + 0.1679(Se) + 0.02722(\beta_{500}) \qquad 0.30 < \left(\frac{H}{H_o}\right) < 0.80 \tag{99b}$$

$$\frac{H_d}{H} = 0.232\left(\frac{H}{H_o}\right) + 0.0258(Se) + 0.10165(\beta_{500}) \qquad 0.80 \le \left(\frac{H}{H_o}\right) \tag{99c}$$

$$\frac{H_d}{H} = 1.018 - 0.157\left(\frac{H}{H_o}\right) + 0.0049(Se) + 0.00077(\beta_{880}) \qquad 0 \le \left(\frac{H}{H_o}\right) \le 0.30 \tag{99d}$$

$$\frac{H_d}{H} = 1.529 - 1.449\left(\frac{H}{H_o}\right) + 0.1645(Se) + 0.2881(\beta_{880}) \qquad 0.30 < \left(\frac{H}{H_o}\right) < 0.80 \tag{99e}$$

$$\frac{H_d}{H} = 0.229\left(\frac{H}{H_o}\right) + 0.0569(Se) + 0.0838(\beta_{880}) \qquad 0.80 \le \left(\frac{H}{H_o}\right) \tag{99f}$$

4.6.7 Group 7

In this group, sunshine fraction, mean temperature and relative humidity were incorporated with diffuse for estimating diffuse solar radiation in the form:

$$\frac{H_d}{H} = a + b\left(\frac{S}{S_o}\right) + c\left(\frac{S}{S_o} - \theta - R\right) + d\left(\frac{S}{S_o}\right)^2 \tag{100}$$

Sambo and Doyle [51] established the following MB models for Zaria as:

$$\frac{H_d}{H} = 1.325 - 1.960\left(\frac{S}{S_o}\right) + 0.389\left(\frac{S}{S_o} - \theta - R\right) + 1.65\left(\frac{S}{S_o}\right)^2 \quad (101)$$

4.6.8 Group 8

In this group, clearness index, sunshine fraction, mean temperature and relative humidity were incorporated with diffuse for estimating diffuse solar radiation in the form:

$$\frac{H_d}{H} = a + b\left(\frac{H}{H_o}\right) + c\left(\frac{S}{S_o}\right) + d\left(\frac{T_{\max}}{T_{\min}}\right) + e(RH) \quad (102)$$

Falayi *et al.* [52] applied a new combination of meteorological parameters to proposed eight MB models for some nominated locations in Nigeria.

For Sokoto

$$\frac{H_d}{H} = 1.055 - 0.815\left(\frac{H}{H_o}\right) - 0.0353\left(\frac{S}{S_o}\right) + 0.142\left(\frac{T_{\max}}{T_{\min}}\right) + 0.00078(RH) \quad (103a)$$

For Maiduguri

$$\frac{H_d}{H} = 0.7795 - 0.830\left(\frac{H}{H_o}\right) - 0.0364\left(\frac{S}{S_o}\right) + 0.152\left(\frac{T_{\max}}{T_{\min}}\right) + 0.00023(RH) \quad (103b)$$

For Port Harcourt

$$\frac{H_d}{H} = 0.684 - 0.735\left(\frac{H}{H_o}\right) - 0.095\left(\frac{S}{S_o}\right) + 0.0248\left(\frac{T_{\max}}{T_{\min}}\right) + 0.00065(RH) \quad (103c)$$

For Owerri

$$\frac{H_d}{H} = 0.775 - 0.954\left(\frac{H}{H_o}\right) - 0.056\left(\frac{S}{S_o}\right) + 0.000042\left(\frac{T_{\max}}{T_{\min}}\right) + 0.0762(RH) \quad (103d)$$

For Enugu

$$\frac{H_d}{H} = 0.642 - 0.851\left(\frac{H}{H_o}\right) - 0.044\left(\frac{S}{S_o}\right) + 0.079\left(\frac{T_{\max}}{T_{\min}}\right) + 0.0014(RH) \quad (103e)$$

For Yola

$$\frac{H_d}{H} = 1.1007 - 0.9844\left(\frac{H}{H_o}\right) - 0.0214\left(\frac{S}{S_o}\right) + 0.1117\left(\frac{T_{\max}}{T_{\min}}\right) + 0.0001(RH) \quad (103f)$$

For Jos

$$\frac{H_d}{H} = 1.028 - 1.0081\left(\frac{H}{H_o}\right) - 0.0229\left(\frac{S}{S_o}\right) + 0.031\left(\frac{T_{\max}}{T_{\min}}\right) + 0.0011(RH) \quad (103g)$$

5. Discussion

The global sum of regression models reported by peers and researchers for predicting diffuse solar radiation in North-Western Africa is ever increasing and relatively high, which in turn makes it highly laborious to employ statistical indicators such as Root Mean Square Error (RMSE), Sum of the Square of Relative Error (SSRE), Relative Standard Error (RSE), Standard Deviation of the residual (SD), Mean Absolute Bias Error (MABE), Mean Absolute Percentage error (MAPE), coefficient of determination,

uncertainty at 95% (U_{95}), Mean Bias Error (MBE), Mean Percentage Error (MPE), Nash Sutcliffe coefficient (NS), Index of Agreement (IG), Mean Absolute Error (MAE) and Global Performance Indicator (GPI) etc. to select the best approach for a particular site in a single research paper. Recently, Khorasanizadeh and Mohammad [53] classified numerous diffuse solar radiation models across the globe into four categories such as cleanness index based-models, sunshine based-model, cloud cover-based models and other meteorological parameter based-models.

Sunshine-based models are frequently applied due to their global availability at most weathers stations in North-Western Africa. Cloud cover-based models can be employed in the absence of clearness index and sunshine-based models but are sensible to human biasing [54].

Clearness index based-models are the most frequently applied model for predicting diffuse solar radiation globally as a result of the availability of are reliable measured global solar radiation in most stations around the globe and extraterrestrial solar radiation can be calculated theoretically as given in equation (3). This model pioneered by Liu and Jordan [11] has been applied by several researchers for estimating diffuse solar radiation for several locations across the globe by determining the empirical constants by applying meteorological parameters of their chosen site of interest. Apart from Liu and Jordan [11], those fitted by Page [55] and Iqbal [56] seem to be universally applicable. However, models fitted by numerous researches in Africa [34, 37-39, 57-60] yielded better performance and high accuracy in the fitted sites as compared to reported models in literature that seem to be universally applicable. This result is in agreement with the report in most African countries [33, 43-44, 59, 61-64] confirming that diffuse solar radiation is dependent on the local climate and geographical information of a given site.

Other meteorological parameter-based models are recorded to predict diffuse solar radiation with high precision but most of their input parameters are not really available at most sites of interest in North-Western Africa and across the globe.

In this review, the researchers included two meteorological parameters often applied by one solar energy researcher to predicting solar radiation in Nigeria via: global solar radiation-based models and monthly mean based models. In general, one hundred and eighty-eight (188) theoretical models were reported with 33 functional forms and 20 groups (sub-class) in this review. Eighty three (83) models with the corresponding 8 functional forms and 6 groups were recorded from clearness index-based models representing 44.14 %, 45models with the corresponding 6 functional forms and 3 groups resulting to 23.93 % were applied for sunshine-based models; 7 models with 1 functional form and 1 group amounting to 3.72 %, for cloud cover-based models; 1 model with 1 functional form and 1 group yielding to 0.53 % for extraterrestrial solar radiation-based models and monthly-based models; and 51 models with 16 functional functions and 8 groups resulting to 27.12 % for hybrid parameter-based models as presented in Fig. 8.

Peers and researchers have shown that it is humanly impossible for now to introduce a set of input variables with a particular functional form for optimal prediction of diffuse solar radiation in Nigeria and Egypt or any other geographical environment across the globe because of its dependence on geographical information and local climate of the site [10, 39-40, 41, 45-46, 52, 57-59, 62-64]. To restate this, a brief review of the efforts of researchers in North-Western Africa to enhance the accuracy of prediction of diffuse solar radiation is presented in the following paragraphs.

El-Sebaii and Trabea [41] employed sunshine-based model and clearness index-based model for predictions of diffuse solar radiation on the horizontal surface for four

Egyptian locations. The selected locations include Matruth, Al-Arish, Rafah and Aswan to represent the weather conditions of the North and South of Egypt. The first, second and third order correlations between the diffuse fraction and clearness index produced better accurate results compared to the correlations between sunshine fraction and diffuse fraction or diffuse coefficients in the selected four locations as shown in Table 1.

Table 1. Statistical indicators for Matruth, Ratah and Aswan El-Sebaii and Trabea [41]

Stations	Degree of Correlation	Correlation between	MBE	RMSE	MPE (%)
Matruth	First	H_d/H and H/H_o	0.07	0.022	1.17
	Second	H_d/H and H/H_o	0.007	0.024	-1.05
	Third	H_d/H and H/H_o	0.006	0.020	-1.07
	First	H_d/H and S/S_o	-0.001	0.003	-0.63
	Second	H_d/H and S/S_o	0.001	0.002	-0.38
	Third	H_d/H and S/S_o	0.001	0.002	-0.39
	First	H_d/H_o and S/S_o	0.003	0.007	-0.72
	Second	H_d/H_o and S/S_o	0.002	0.001	-0.40
	Third	H_d/H_o and S/S_o	0.002	0.001	-0.39
Al-Arish	First	H_d/H and H/H_o	-0.005	0.019	-1.27
	Second	H_d/H and H/H_o	-0.005	0.019	-1.07
	Third	H_d/H and H/H_o		Very poor fitting	
	First	H_d/H and S/S_o	0.002	0.008	-1.26
	Second	H_d/H and S/S_o	0.001	0.002	-0.40
	Third	H_d/H and S/S_o	0.005	0.018	-0.83
	First	H_d/H_o and S/S_o	-0.004	0.015	-1.08
	Second	H_d/H_o and S/S_o	-0.003	0.009	-0.73
	Third	H_d/H_o and S/S_o	0.003	0.009	-0.54
Rafah	First	H_d/H and H/H_o	-0.003	0.010	-0.57
	Second	H_d/H and H/H_o	-0.003	0.010	-0.38
	Third	H_d/H and H/H_o	-0.003	0.011	-0.55
	First	H_d/H and S/S_o	-0.002	0.001	-0.36
	Second	H_d/H and S/S_o	0.003	0.012	-0.16
	Third	H_d/H and S/S_o	0.005	0.016	0.46
	First	H_d/H_o and S/S_o	-0.004	0.014	-0.16
	Second	H_d/H_o and S/S_o	0.001	0.001	-0.12
	Third	H_d/H_o and S/S_o	-0.001	0.001	-0.09
Aswan	First	H_d/H and H/H_o	-0.003	0.014	-1.07
	Second	H_d/H and H/H_o	-0.005	0.012	-0.82
	Third	H_d/H and H/H_o	-0.004	0.015	-0.93
	First	H_d/H and S/S_o	-0.002	0.008	-0.43
	Second	H_d/H and S/S_o	-0.003	0.005	-0.40
	Third	H_d/H and S/S_o	-0.003	0.0114	-0.38
	First	H_d/H_o and S/S_o	-0.001	0.005	-0.27
	Second	H_d/H_o and S/S_o	-0.002	0.005	-0.25
	Third	H_d/H_o and S/S_o	-0.002	0.008	-0.23

Sanusi and Abisoye [47] applied Page model (first order polynomial equation), Liu and Jordan model (third order polynomial equation), second order polynomial, power and exponential models to develop an empirical model for Lagos using eleven years (1999 – 2009) data. The performances for the models were tested using statistical indicators such as Mean Percentage Error (MPE), Mean Bias Error (MBE), Root Mean Square Error (RMSE) and coefficient determination (R^2). The results revealed that the second-order quadratic model yielded reasonably high degree of precision in the forecast of monthly

mean daily diffuse solar radiation in the horizontal surfaces as shown in Table 2. These results were in agreement with the findings in literature [41, 45-46, 57, 64].

Table 2. Statistical indication for the models. Sanusi and Abisoye [47]

Models	MPE (%)	RMSE ($MJm^{-2}day^{-1}$)	MBE ($MJm^{-2}day^{-1}$)	Coefficient of Determination (R^2)
Page (1961) (First order polynomial)	4.800	0.129	0.104	0.982
Liu and Jordan (1960) (Third order polynomial)	9.336	0.201	-0.194	0.978
Second-order polynomial	0.010	0.048	0.001	0.982
Exponential	0.012	0.051	-0.001	0.980
Power	0.168	0.065	-0.006	0.971

Okundamiya *et al.* [45] calibrated Okundaniya and Nzeako [46] model for numerous numbers of sites, with varying meteorology covering the entire geographical zones in Nigeria. The authors tested the performance of the newly calibrated multivariable regression model, which uses clearness index and cloud cover as inputs for estimating the monthly daily mean diffuse solar radiation, on a horizontal surface in Nigeria with five existing empirical models, which utilizes the clearness index, cloud cover, relative sunshine duration or the combination of two of these variables as inputs [11, 46, 55, 65-66]. The results revealed that the calibrated multivariable regression model performed better than the other five existing models with a relative percentage error of $\pm$6% over Nigeria as presented in Table 3. These results justify the recommendation made by Munner and Munawwar [67] that the inclusion of cloud cover improves the prediction accuracy of diffuse solar radiation on the horizontal surfaces. This result is also comparable to the report of numerous researchers in Africa [35, 37, 39, 42, 44, 60, 68-69].

Table 3. Validation results of six studies diffuse radiation model for Nigeria based on 22 years' data sets Okundamiya *et al.* [45]

Sites	Error Terms (units)	Page [55]	Liu and Jordan [11]	Butt *et al.* [65]	Karakoti *et al.* [66]	Okundamiya and Nzeako[46]	Okundamiya *et al.* [45]
Sokoto	r	0.9497	0.9461	0.8446	0.8173	0.9521	0.9967
	RMSE (MJ/m^2)	0.4049	0.4219	0.8951	1.0711	0.3966	0.1061
	MBE (MJ/m^2)	-0.1652	-0.1832	0.5307	0.7989	-0.1575	-0.0185
	MABE (MJ/m^2)	0.3261	0.3434	0.6515	0.9239	0.3213	0.0793
Maiduguri	r	0.9470	0.8594	0.9085	0.9246	0.9284	0.9950
	RMSE (MJ/m^2)	0.3976	0.6884	0.7798	0.4401	0.4556	0.1981
	MBE (MJ/m^2)	-0.1506	-0.2523	-0.0831	0.0467	-0.1606	-0.1592
	MABE (MJ/m^2)	0.3269	0.5246	0.7136	0.3557	0.3629	0.1623
Abuja	r	0.9930	0.9951	0.9175	0.9295	0.9937	0.9980
	RMSE (MJ/m^2)	0.1727	0.2427	0.6918	0.5350	0.1802	0.1109
	MBE (MJ/m^2)	-0.0744	-0.1414	0.1298	0.1363	-0.0924	-0.0461
	MABE (MJ/m^2)	0.1182	0.1836	0.5151	0.4277	0.1461	0.1000
Ikeja	r	0.9848	0.9933	0.9307	0.9333	0.9875	0.9951
	RMSE (MJ/m^2)	0.1615	0.1857	0.7551	0.3119	0.1605	0.1098
	MBE (MJ/m^2)	0.0370	0.0662	-0.6056	-0.1614	0.0573	-0.0849
	MABE (MJ/m^2)	0.1395	0.1519	0.6550	0.2568	0.1392	0.0913
Enugu	r	0.9887	0.9890	0.9032	0.8767	0.9887	0.9957
	RMSE (MJ/m^2)	0.1348	0.1282	0.5029	0.4102	0.1289	0.0778
	MBE (MJ/m^2)	-0.0220	-0.0365	0.0973	-0.0216	-0.0237	-0.0030
	MABE (MJ/m^2)	0.1137	0.1018	0.4208	0.3241	0.1113	0.0663
Benin-City	r	0.9869	0.9849	0.9508	0.9360	0.9865	0.9935
	RMSE (MJ/m^2)	0.1537	0.1471	0.5365	0.3942	0.1481	0.1129
	MBE (MJ/m^2)	-0.0599	-0.0781	-0.0262	0.0843	-0.0624	-0.0633
	MABE (MJ/m^2)	0.1197	0.1170	0.4814	0.2932	0.1162	0.0955

From the report of existing studies, it is clear that from above findings that introducing an appropriate set of input for diffuse solar radiation prediction in any geographical site and climatic condition is not a viable work. This could be attributed to

numerous number of required inputs variables, inaccuracies associated with irrelevant variables, difficulty in explaining the model, time consuming task for assembling the needed variable and finally its inability to accept many input variables.

For instant, the Artificial Intelligence (AI) and Computation Intelligence (CI) techniques such as Artificial Neural Network (ANN), machine learning, genetic programming, support vector machine, Adaptive Neural Fuzzy Inference System (ANFIS) and hybrid networks have been widely applied in numerous scientific areas for modeling, estimation, prediction, forecasting and optimization such as Support Vector Machine (SVM) [70-74]; Hybrid network [17, 70-71]; genetic programming [16, 75], Adaptive neural fuzzy inference system [73, 75-77]; and an Automatic Relevance Determination (ARD) methodology Bosch *et al.* [78];can be adopted for predicting diffuse solar radiation in North-Western Africa. Various applications of artificial neural networks are reported in numerous fields such defense, image impression, mathematics, character recognition, aerospace, neurology, meteorology, economic, electronic nose engineering, machine and psychology (Nwokolo and Ogbulezie [9]. These methods have been adopted for prediction and empirical analysis in market trend forecasting, solar and weather.

Boland and Scott [18] determined the comparison between the empirical models and a fuzzy logic based model to estimate hourly diffuse solar radiation in some locations of Australia. The results revealed that coefficients of determination recorded for the fuzzy logic model are comparable, and in most cases more suitable than those of empirical models.

Jiang [19] developed a model based Artificial Neural Network (ANN) model to predict monthly mean daily diffuse solar radiation in China. The researcher employed measured data of eight typical stations for training and data of one station for testing. He proceeded by comparing the estimation of ANN model with those of regression models. According to the author, the results revealed that ANN model compared to the regression model offer is more suitable for estimating diffuse solar radiation in the eight stations studied.

Elminir *et al.* [13] estimated hourly and daily diffuse radiation of Egypt by applying neutral network (ANN) and compared the result with two linear empirical models. The performances of the models were determined on the basis of the Mean Bias Error (MBE), Root Mean Square Error (RMSE) and correlation coefficient (r) between the estimated and measured data. The results reveal that ANN model is more suitable to predict diffuse radiation in hourly and daily scales than empirical models.

Alam *et al.* [20] employed Artificial Neural Network (ANN) to estimate monthly mean hourly and daily diffuse radiation in ten Indian stations with diverse weather conditions. They applied different parameter as inputs and used the feedforward back-propapgation algorithm to train the ANN model. They discovered that that ANN model compared to the regression model offer is more suitable for estimating diffuse solar radiation in the ten stations studied.

Lazarevska and Trpovski [21] applied neuro fuzzy inference system with a relevance vector machine mechanism for estimation of diffuse solar radiation. They used global solar radiation and solar elevation angle as input parameters to estimate the diffuse solar radiation. Their result revealed that the new developed technique is really effective and remarkably outperformed the existing regression models.

Soares *et al.* [14] stimulated a technique based upon artificial neural network (MLP-ANN) method for estimation of hourly diffuse solar radiation in the city of Sao Paulo, Brazil. The result revealed that the estimated diffuse solar radiation values obtained from

MLP-ANN technique are more suitable compared to those of empirical models as shown in Table 4 and Fig. 3-4.

Table 4. Model Statistics Soares *et al.* [14]

	Sample size	MBE (MJm^{-2})	RMSE (MJm^{-2})	t_s	t_c
Correlation model form Oliveira *et al.* (2002)	15258	-0.0169	0.193	11.16	1.96
MLP neural-network - Experiment I	2928	0.0116	0.121	5.19	1.96
MLP neural-network - Experiment II	2928	0.0291	0.152	10.63	1.96
MLP neural-network - Experiment III	2928	0.0110	0.155	3.86	1.96

t_c is given at a level of confidence of 95 %.

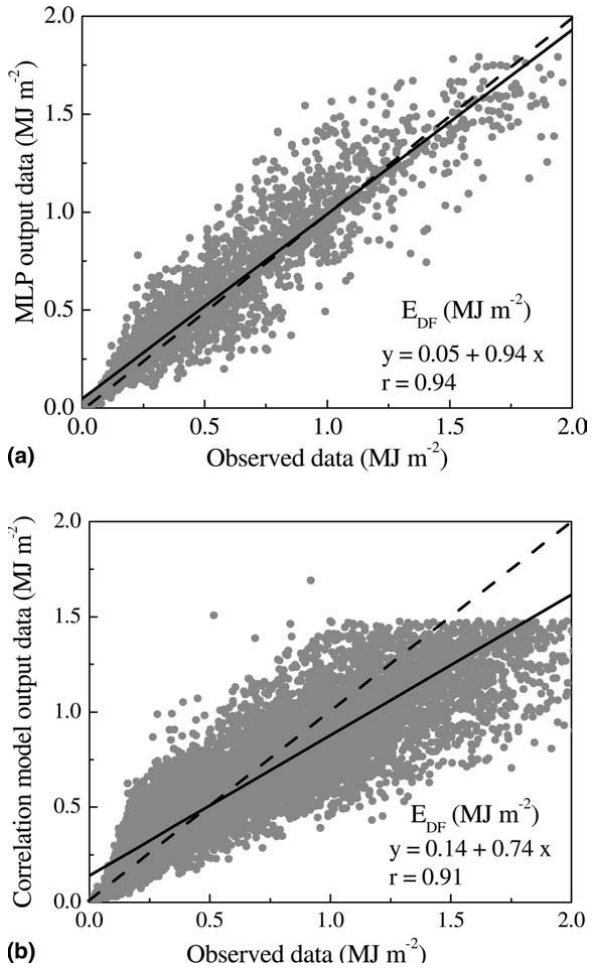

Fig. 3. Dispersion diagram between the hourly values of diffuse radiation observed and (a) using MLP based on 2928 pairs of points and (b) using the correlation model based on 15,258 pairs of points (from Oliveira *et al.* [79]). Dashed line corresponds to diagonal and continuous line corresponds to curve fitted by least squares method. The corresponding linear equations are indicated in the bottom of each diagram and r is the correlation coefficient Soares *et al.* [14].

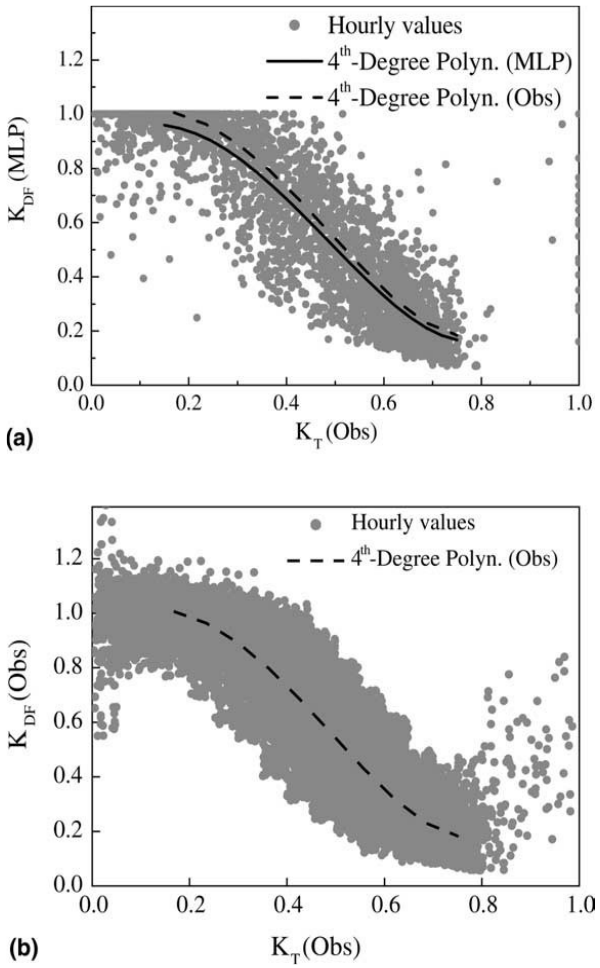

Fig. 4. KT scatter diagram for hourly values of solar radiation. (a) KDF obtained using MLP, based on2928 pairs of points and (b) KDF observed in São Paulo City, based on 15,258 pairs of points (from Oliveira *et al.* [79]). The continuous and dashed lines display the fourth-degree polynomial curves obtained, respectively, from MLP and Lawrence (1991); Soares *et al.* [14].

Lou *et al.* [15] employed machine learning logarithm to estimate the horizontal sky-diffuse irradiance and conduct sensitivity analysis for the meteorological parameters. Apart from the clearness index, the authors discovered that predictors including solar attitude, air temperature, cloud cover and visibility are more suitable for estimating diffuse solar radiation component. The Mean Absolute Error (MAE) of the logistic regression using the aforementioned predictors was less than 21.5w/m^3 and 30w/m^3 for Hong Kong and Denver, USA as presented in Table 5.

Table 5. Results of Logistic Regression Lou *et al.* [15]

Regression	Predictors	Parameters						Performance			
		f_0	f_1	f_2	f_3	f_4	f_5	Data of 2008-2012		Data of 2013	
								MAE (W/m^2)	R^2	MAE (W/m^2)	R^2
1	k_t	-4.61	7.78	0	0	0	0	29.2	0.850	27.5	0.851
2	k_t, μ	-4.42	8.75	-1.16	.0	0	0	26.3	0.867	26.2	0.851
3	k_t, μ, T_a	-4.37	8.85	-1.38	0.12	0	0	25.7	0.875	25.2	0.866
4	k_t μ, T_a, Cld	-3.4	7.4	0.8	0.2	-1	0	23.2	0.400	21.8	0.901
5	k_t, μ, T_a, Cld, VIS	-3.3	7.14	0.68	0.13	-1.08	0.18	21.5	0.914	20.0	0.916

Where Kt is clearness index, μ is the sine of solar attitude angle (sin (α_S)), Ta is air temperature, Cld is the cloud amount, VIS is the visibility

Feng *et al.* [12] proposed four artificial intelligence models including the Extreme Learning Machines (ELM), back propagation neural networks optimized by Genetic Algorithm (GANN) Random Forest (RF), and Generalized Regression Neural Networks (GRNN) for estimating daily diffuse solar radiation at two meteorological stations of North China Plain. Daily global solar radiation and sunshine duration were selected as model inputs to train the models. The proposed models were compared with the empirical Iqbal model to test their performance employing measured daily diffuse solar radiation data. The result revealed that the ELM, GANN, RF, and GRNN models all performed much better than the empirical Iqbal model for estimating daily diffuse solar radiation. On the whole, all the models under-estimated daily diffuse solar radiation for both stations with average relative error ranging from 5.8% to 5.4% for all models and 19.1% for Iqbal model in Beijing; 5.9% to 4.3% and 26.9% in Zhengzhou respectively. Generally, GANN model recorded the best accuracy and ELM ranked the next, followed by RF and GRNN model. The ELM model reported a slightly poorer performance but the highest computation speed, and both GANN and ELM could be highly recommended for estimating daily diffuse solar radiation in North China Plain as presented in Table 6 and Fig. 5.

Table 6: Statistics Performances of different models in estimation daily diffuse solar radiation for each Station Feng *et al.* [12]

Station	Model	RRMSE (%)	MAE ($MJm^{-2}day^{-1}$)	NS
Beijing	ELM	17.3	0.760	0.908
	GANN	17.1	0.748	0.909
	RF	18.3	0.841	0.897
	GRNN	19.2	0.951	0.880
	Iqbal	32.9	0.162	0.666
Zhengzhou	ELM	13.4	0.762	0.924
	GANN	13.4	0.749	0.928
	RF	15.0	0.862	0.910
	GRNN	16.5	0.997	0.892
	Iqbal	35.8	2.359	0.491

RRMSE is the relative root mean square error, MAE is the mean absolute error and NS is Nash Sutcliffe coefficient

Mohammadi *et al.* [16] applied Adaptive Neuro-Fuzzy Influence System (ANFIS) to select the most influential parameters for prediction of daily horizontal diffuse solar radiation (H_d). Ten significant parameters are selected to analyze their impact on estimation H_d in the city of Kerman, situated in the south central part of Iran. For this purpose, a thorough parameter selection was conducted for the cases with 1, 2 and 3 inputs to introduce the best and worst inputs combinations. For the cases with 2 and 3 inputs, 45 and

120 possible combinations of inputs are considered, respectively. For the cases with one input variable, the results revealed that sunshine duration(s) is the most influential variable. Moreover, combination of H, Ho and S are the best sets among the cases with 2 and 3 inputs variables respectively. The observed result revealed that combinations of either 2 or 3 most relevant inputs would be appropriate to provide a balance between the simplicity and high precision. Predictions using the most influential set of 2 and 3 inputs revealed that for the ANFIS model with two inputs variables, the mean absolute percentage error, mean absolute bias error, root mean square error and correlation coefficient are 23.0579%, 1.0176 MJ/m^2, 1.3052 MJ/m^2 and 0.8247, respectively, and for the ANFIS model with three inputs they are 18.3143%, 0.8134 MJ/m^2, 1.1036MJ/m^2 and 0.8783, respectively as presented in Table 7 and Fig. 6.

Table 7. Five most and least relevant combination of inputs and ANFIS regression error (RMSE in MJ/m^2) achieved for training and checking phases Mohammadi *et al.* [16].

Combination No.	Combination of Inputs	RMSE for Training	RMSE for Checking
Combination 1	H, H_o, S (Ist best model)	1.2417	1.2889
Combination 9	H, S, and S_o (2^{nd} best model)	1.2523	1.2968
Combination 15	H, S, and (3rd best model)	1.2532	1.2971
Combination 5	H, H_o and T_{arg} (4th best model)	1.2820	1.2925
Combination 3	H, H_o, and T_{min} (5th best model)	1.2902	1.3222
Combination 28	H, T_{max} and RH (1st worst model)	1.8916	1.9339
Combination 90	So, T_{min} and S (2^{nd} worst model)	1.8671	1.8673
Combination 97	So, T_{avg} and S (3rd worst model)	1.8571	1.8643
Combination 94	So, T_{max} and S (4th worst model)	1.8395	1.8585
Combination 117	T_{ava}, RH and V_p (5th worst model)	1.8231	1.8890

Where S is the sunshine duration, H global solar radiation, δ solar declination, H_o extraterrestrial solar radiation S_o maximum possible sunshine duration V_p water vapour pressure, RH relative humidity, T_{avg} average air temperature, T_{min} minimum temperature, T_{max}maximum temperature.

During the last decades, numerous renewable energy researchers have carried out number of studies for estimation of diffuse solar radiation mainly by developing different soft computing techniques and regression models, but there is still a main challenge regarding the development of powerful hybrid soft computing techniques and models with high level of reliability and adaptability to achieve accurate predictions just as hybrid regression models offer more suitable prediction compared to one parameter-based models. Lately, coupling different approaches of soft computing to build a hybrid model has received a considerable attention in the renewable energy area. On the whole, it is possible to take the advantage of specific nature of different soft computing techniques for enhancing the precision. In fact, the particular features of different soft computing techniques are able to capture different patterns in the data series. Recent findings from literature have revealed that hybrid soft computing approaches would be particularly effective and promising for different applications of renewable energy to enhance the estimation accuracy and reliability.

For instance, in a study to determine diffuse solar radiation in the city of Kerman, Shamshirband *et al.* [81] employed a couple model by integrating the support vector machine (SVM) with Wavelet Transform (WT) algorithm for estimating daily horizontal diffuse solar radiation. In order to test the validity of the coupled SVM-WT method, daily measured global and diffuse solar radiation data sets for city of Kerman located in sunny part of Iran are utilized. Using the developed SVM-WT model diffuse fraction is related

with clearness index as the only input variable. The performance of SVM-WT model is calculated against radial basis function SVM (SVM-RBF), Artificial Neural Network (ANN) and a third order empirical model established by the researchers. The results revealed that the estimated diffuse solar radiation values by the SVM-WT model agreed favourably with measured data. The statistical Indicators revealed that the mean absolute bias error, root mean square error and correlation coefficient are 0.5757 MJm^{-2}, 0.6940MJ/m^2 and 0.9631, respectively. While for the SVM-RBF ranked next the attained values are 1.0877 MJm^{-2}, 1.2583MJ/m^2 and 0.8599, respectively. In a nut shell, the study revealed that SVM-WT is an efficient method which enjoys much higher precision than other models, especially the third order empirical model as shown in Table 8 and Fig. 7.

Table 8. The attained MABE, RMSE and R for all models for the testing data set Shamshirband *et al.* [81].

Model	MABE (MJ/m^2)	RMSE (MJ/m^2)	R
SVM – WT	0.5757	0.6940	0.9631
SVM – REF	1.0877	1.2583	0.8599
ANN	1.1267	1.3183	0.8392
Empirical Model	1.2171	1.4548	0.8156

The regression models for predicting diffuse solar radiation were examine extensively and its performances were compared with the soft computing approach in North-Western Africa and across the globe. This review paper distinctively provided reliable outcome for various approaches (empirical and soft computing model). The regression models regarded as capable and convenient for hourly, daily and monthly estimation are clearness index-based models, sunshine-base models, cloud cover-based models, extraterrestrial solar radiation-based models, monthly-based models and hybrid parameter-based model. A number of important aspects identified in literature as well as shortcomings with solutions recommended in the present study are summed up subsequently.

In the light of presented review literature, it seems that a number of sites do not have meteorological stations, whereby empirical and soft computing models should be developed employing attitude, latitude, longitude, solar declination angle, and extraterrestrial solar radiation inputs for precise measurement as they require no experimental measurement to obtain their values. Soft computing models have newly been initiated for predicting renewable energy resources, but additional work is needed to enhance solar radiation prediction accuracy pertaining to various seasons, climate change and poor weather, on different surfaces, (*e.g.,* tiled) Nwokolo and Ogbulezie [9]. Hence, according to the authors, the greatest advantages may be needed from natural resources to supply increasingly reliable efficient solar systems in the market.

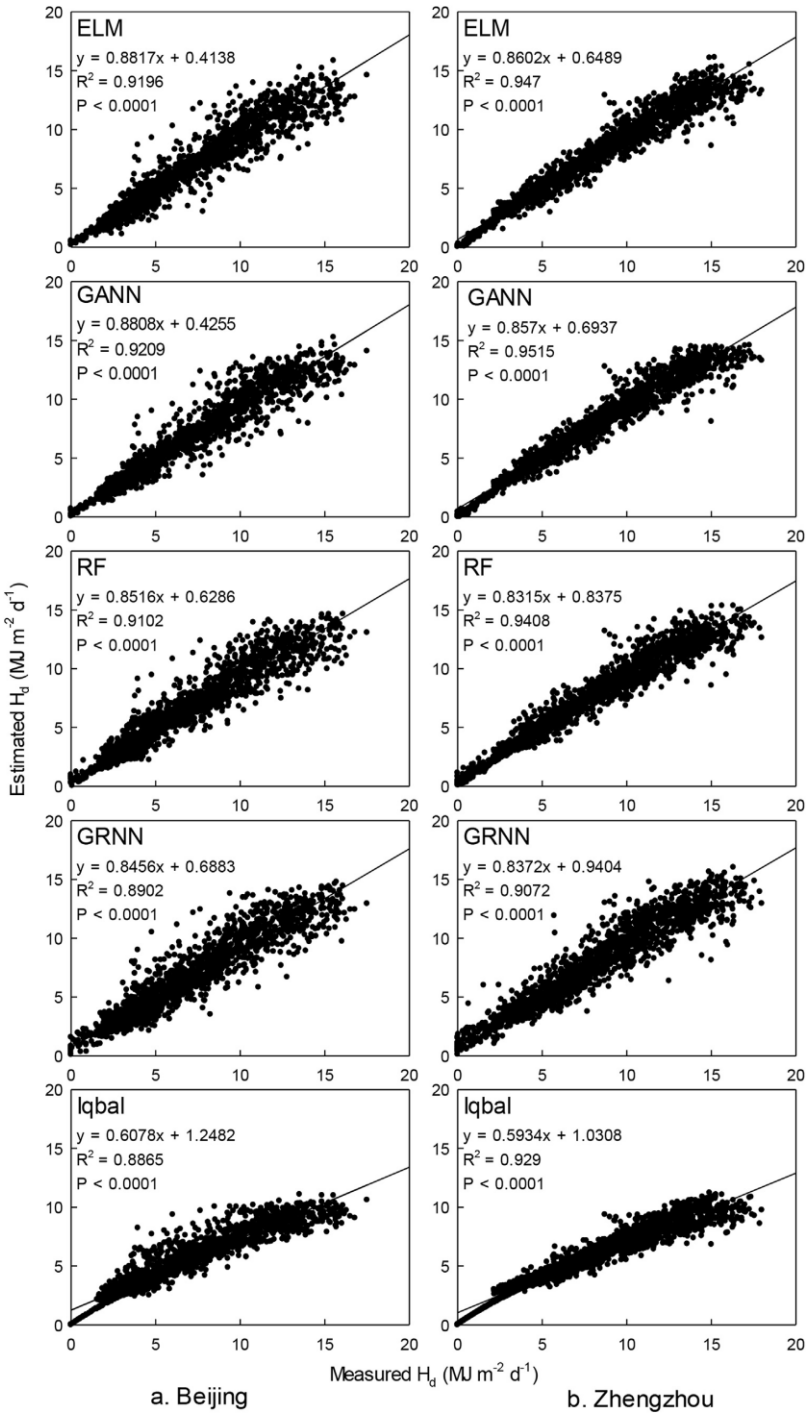

Fig. 5. Scatter plots of the measured versus the estimated daily diffuse solar radiation at (a) Beijing and (b) Zhengzhou of North China Plain by Feng *et al.* [12].

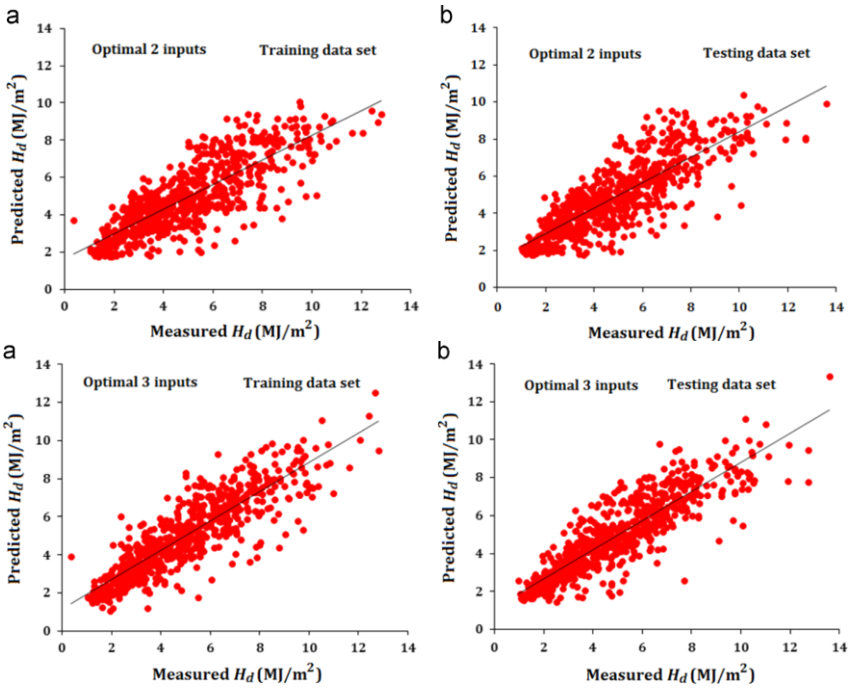

Fig. 6. Performance of the ANFIS model to predict H_d using optimal combination of 3 inputs for: (a) training dataset and (b) checking dataset Mohammadi *et al.* [16].

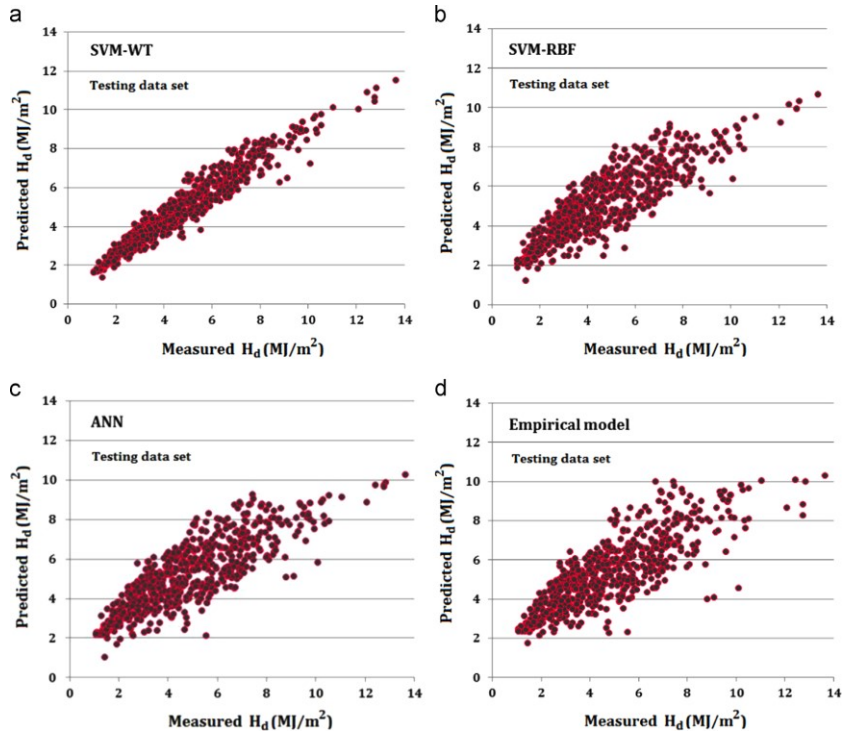

Fig. 7. Scatter plots of them ensured diffuse solar radiation versus predictions of (a) SVM–WT, (b) SVM–RBF, (c) ANN and (d) empirical model for the testing data set (Shamshirband *et al.* [81])

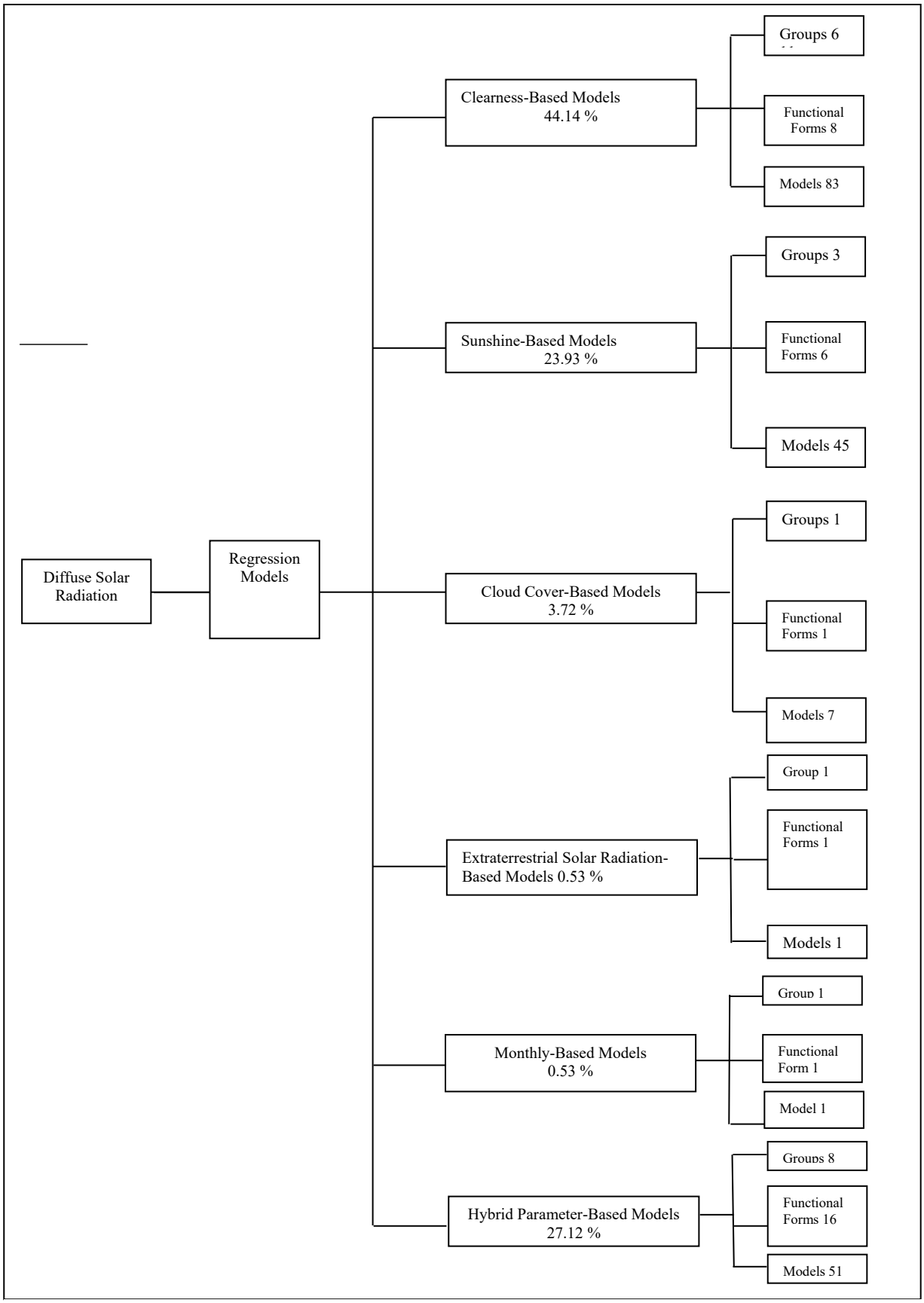

Fig. 8. Classification of diffuse solar radiation and its associated number of groups, functional forms, and models in Nigeria and Egypt

5. Concluding Remarks

The regression models for predicting diffuse solar radiation were investigated extensively and its performances were compared with the soft computing approach in North-Western Africa and across the globe. This review paper distinctively provided reliable outcome for various approaches (regression and soft computing model). The regression models are regarded as capable and convenient for hourly, daily and monthly estimation are clearness index-based models, sunshine-base models, cloud cover-based models, extraterrestrial solar radiation-based models, monthly-based models and hybrid parameter-based model. Owing to the inability of regression models to accept many input parameters but rather strengthened in its reliability, a number studies in literature revealed that soft computing models are more suitable for predicting diffuse solar radiation in several locations distributed across the globe. Thus, applying soft computing and even power hybrid soft computing models will culminate in the greatest understanding of availability diffuse solar radiation in a particular region or location that is needful for supplying increasingly reliable efficient solar systems in the market.

Acknowledgements

Our thanks go to all the authors cited in this paper for their research works that have made this research possible.

Funding

This research did not receive any specific grant from funding agencies in the public, commercial, or not-for-profit sectors.

CONFLICTS OF INTEREST

The authors declare that there is no conflict of interests regarding the publication of this paper.

REFERENCES

[1] International Energy Agency (IEA) Report (Report IEA PVPS TI-26:2015): Snapshot of Global PV markets (1992-2014), ISBN: 978-3-906042-32-9.
[2] McCree K J. Test of current definitions of photosynthetically active radiation against leaf photosynthesis data. Agric. For. Meteorol., 1972, 10: 443–453.
[3] Wang Q, Kakubari Y, Kubota M. Variation of PAR to global solar radiation ratios along altitude gradient in Naeba Mountain. Theo. and Appl. Clima., 2007, 87: 239-253.
[4] El-Sebaii A A, Al-Agel F. Estimation of horizontal diffuse solar radiation from common meteorological parameters: a case study for Jeddah, Saudi Arabia, International Journal of Ambient Energy, 2012, 34: 1-8.

[5] Mohammed A A A. The Analysis of the characteristics of the solar radiation climate of the daily global radiation and diffuse radiation in Amman, Jordan, International Journal of Renewable Energy, 2010, 5, 23-38.
[6] Bhattacharya A B, Kar S K, Bhattacharya R. Diffuse solar radiation and associated meteorological parameters in India, Ann. Geophysi., 1996, 14: 1051-1059.
[7] Nwokolo S C. A comprehensive review of empirical models for estimating global solar radiation in Africa. Renewable and Sustainable Energy Reviews, 2017, 78: 955-995.
[8] Nwokolo S C, Ogbulezie J C, Toge C K, John-Jaja S A. Modeling the influence of relative humidity on photosynthetically active radiation from global horizontal irradiation in six tropical ecological zones in Nigeria. New York Science Journal, 2016a, 9: 40-55.
[9] Nwokolo S C, Ogbulezie J C. A quantitative view and classification of empirical models for predicting global solar radiation in West Africa. Beni-Suef Univ J. Basis Appl. Sci., 2017a, DOI: 10.1016/j.bjbus.2017.05.001.
[10] Nwokolo S C, Ogbuezie J C. Modelling the influence of cloudiness on diffuse horizontal irradiation under various sky conditions over six tropical ecological zones in Nigeria. International Journal Physical Sciences, 2017b, 5(2): 91-100.
[11] Liu B V H, Jordan R C. The interrelationship and characteristics distribution of direct, diffuse and total solar radiation, Solar Radiation, 1960, 22: 87-90.
[12] Feng Y, Cui N, Zhang Q, Zhao L, Gong D. Comparison of artificial intelligence and empirical models for estimation of daily diffuse solar radiation in North China plain. International Energy of Hydrogen Energy, 2017, DOI: 10.1016/jijhydene.2017.04.084.
[13] Elminir H K, Azzam Y A, Younes E L. Prediction of hourly and daily diffuse fraction using neural network, compared to linear regression models. Energy, 2007, 32: 1513-1523.
[14] Soares J, Oliveira A P, Boznar M Z, Mlakar P, Escobedo J F, Machado A J. Modeling hourly diffuse solar-radiation in the City of Sao Paulo using a neural-network technique. Applied Energy, 2004, 79: 201-214.
[15] Lou S, Li D H W, Lam J C, Chun W W H. Prediction of diffuse irradiance using machine learning and multivariable regression. Applied Energy, 2016, 181: 367-374.
[16] Mohammadi K, Shamshirband S, Petkovic D, Khoronsanizadeh H. Determining the most important variables of diffuse solar radiation prediction using adaptive neuro-fuzzy methodology: Case study: City of Kerman, Iran. Renewable and Sustainable Energy Reviews. 2016, 53: 1570-1579.
[17] Shamshirband S, Mohammadi K, Yee P L, Petkovic D, Mostafaeipour A. A. comparative evaluation for identifying the suitability of extreme learning machine to predict horizontal global solar radiation. Renewable and Sustainable Energy Reviews, 2016, 52: 1031-1042.
[18] Boland J, Scott L. Predicting the diffuse fraction of global solar radiation using regression and fuzzy logic. In: Proceedings of the ANZSES Conference, Geelong, Nov, 1999.
[19] Jiang Y. Predicting of monthly mean daily diffuse solar radiation using artificial neural networks and comparison with other empirical models. Energy Policy, 2008, 36: 3833-3837.
[20] Alam S, Kaushik S C, Garg S N. Assessment of diffuse energy under general sky condition using artificial neural network. Applied Energy, 2009, 86: 554-564.
[21] Lazarevska E, Trpovski J. A neuro-fuzzy model of the solar diffuse radiation with relevance vector machine. In: Proceedings of 11th international Conference on

electrical power quality and utilization (EPQU); 2011, p. 1-6. 10.1109/EPQU.2011.6128803.
[22] Yaniktepe B, Genc Y A. Estimating new model for predicting the global solar radiation on horizontal surface. International Journal of Hydrogen, 2015, 40: 15278-15283.
[23] Zhang J, Zhao L, Deng S, Xn W, Zhang Y. A critical review of the models used to estimate solar radiation. Renewable and Sustainable Energy Reviews, 2017, 70: 314-329.
[24] Sperati S, Alessandrini S, Pinson P, Kariniotakis G. The "Weather Intelligence for Renewable Energies" Benchmarking Exercise on Short-Term Forecasting of Wind and Solar Power Generation. Energies, 2015, 8:9594–9619. DOI: 10.3390/en8099594.
[25] Pelland S, Galanis G, Kallos G. Solar and photovoltaic forecasting through post-processing of the Global Environmental Multiscale numerical weather prediction model, Prog. Photovolt. Res. Appl. 2013, 21: 284–296. DOI: 10.1002/pip.1180.
[26] COST|About COST, (n.d.). http://www.cost.eu/about_cost (accessed on June 31, 2017).
[27] Lauret P, Voyant C, Soubdhan T, David M, Poggi P. A benchmarking of machine learning techniques for solar radiation forecasting in an insular context. Solar Energy, 2015, 112: 446–457. DOI: 10.1016/j.solener.2014.12.014.
[28] Besharat F, Dehghan A, Faghih A R. Empirical models for estimating global solar radiation: A review and case study, Renewable and Sustainable Energy Review, 2013, 21: 798-821.
[29] Ertekin C, Yaldiz O. Estimating of monthly average daily global radiation on horizontal surface for Antalya, Turkey. Renewable Energy, 1999; 17: 95-102.
[30] Nwokolo S C, Ogbulezie J C, Toge C K, John-Jaja S A. Photosynthetically active radiation estimation and modeling over different climatic zones in Nigeria. Journal of Agriculture and Ecology Research International 2016b, Article ID: 2016/JAERI/30000, http://sciencedomain.org/journal/37/articles-press (accessed on November 22, 2017).
[31] Etuk S E, Nwokolo S C, Okechukwu E A, John-Jaja S A. Analysis of photosynthetically active radiation over six tropical ecological zones in Nigeria, Journal of Geography, Environment and Earth Science International, 2016a, 7: 1-15.
[32] Etuk S E, Nwokolo S C, Okechukwu E A. Modelling and estimating photosynthetically active radiation from measured global solar radiation at Calabar, Nigeria, Physical Science International Journal, 2016b, 12: 1-12.
[33] Ezekwe C I, Ezeilo C C O. Measured Solar Radiation in a Nigeria Environment compared with predicted data. Solar Energy, 1981, 26: 181-186.
[34] Said R, Ibrahim S M A. Diffuse solar radiation in Cairo, Egypt. Energy Conversion and Management, 1985, 25: 69-72.
[35] Maduekwe A A l, Chendo M A C. Atmospheric turbidity and the diffuse irradiance in Lagos, Nigeria. International Atomic Energy Agency and United National Education Scientific and Cultural Organization; International Centre for Theoretical Physics, 1994, 1-9.
[36] Babatunde F B, Aro TO. Relationship between clearness Index and Cloudiness at a tropical station (Ilorin, Nigeria). Renewable Energy, 1995, 6 (7): 801-805.
[37] Maduekwe A A L, Chendo M A C. Predicting the component of the total hemispherical solar radiation from sunshine duration measurement in Lagos, Nigeria. Renewable Energy, 1995, 6(7): 807-812.

[38] Trabea A A. A multiple linear correlation for diffuse radiation from global solar radiation and sunshine data over Egypt. Renewable Energy, 1999, 17: 411-420.
[39] Maduekwe A A L, Garba B. Characteristics of the monthly average hourly diffuse irradiance at Lagos and Zaira, Nigeria Renewable Energy, 1999, 17: 213-225.
[40] Shaltout M A M, Hassan A H, Fathy A M. Total suspended particles and solar radiation over Cairo and Aswan. Renewable Energy, 2011, 23: 605-619.
[41] El-Sebaii A A, Trabea A A. Estimation of horizontal diffuse solar radiation in Egypt. Energy Conversion and Management, 2003, 44: 2471-2482.
[42] Burari F W. Correlation of global and diffuse solar radiation compoonents with meteorological parameters for Bauchi. Jolova, 2004, 5 (1): 49-55.
[43] Ugwuoke P E, Okeke C E. Statistical assessment of average global and diffuse solar radiation on horizontal surfaces in typical climate. International Journal of Renewable Energy Research, 2012, 2: 269-273.
[44] Khalil S A, Shaffie A M. A comparative study of total, direct and diffuse solar irradiance by using different models on horizontal and inclined surfaces for Cairo, Egypt. Renewable and Sustainable Energy Reviews, 2013, 27: 853-863.
[45] Okundamiya M S, Emagbetere J O, Ogujor E A. Assessment of six daily diffuse solar radiation models for Nigeria. The 4th Interntional Workshop on Computer Science and Engineering-Summer, WCSE 2014; Dubai; UAE; Page 13-21, August 22-23, 2014.
[46] Okundamiya M S, Nzeake A N. Estimation of diffuse solar radiation for selected cities in Nigeria. International Scholarly Research Network, 2011, 12; 1-6.
[47] Sanusi Y K, Abisoye S G. Estimation of diffuse solar radiation in Lagos, Nigeria. 2nd International Conference on Chemical, Environmental and Biological Sciences (ICCEBS, 2013) March 17-18 Dubai (UAE), 2013, pp 6-9.
[48] Olopade M A, Sanusi V K. Solar Radiation Characteristics, and the performance of photovoltaic (PV) Module in a tropical stratum. Journal of Science Research, 2009, 11: 100-109.
[49] Bamiro O A. Empirical radiation for the determination of solar radiation Ibadan, Nigeria. Solar Energy, 1983, 31(1): 85-94.
[50] Erusiafe F, Chendo M A C. Estimating Diffuse Solar radiation from global solar radiation, International Solar Energy Society, Aix-les-Rains, France, 2014, 16-19 September.
[51] Sambo A S, Doyle M D C. The correlation off global and diffuse solar radiation components with meteorological data for Zaira. Jolova 1998, 5 (1): 40-448.
[52] Falayi E O, Rabiu A B, Teliat R O. Correlations to estimate monthly mean of daily diffuse solar radiation in some selected cities in Nigeria. Advances in Applied Science Research, 2011, 2(4): 480-490.
[53] Khorasanizadeh H, Mohammadi G. Diffuse solar radiation on a horizontal surface: Reviewing and categorizing the empirical models. Renewable and Sustaining Energy Reviews, 2016, 53: 338-362.
[54] Badescu V. Correlations to estimate monthly mean daily solar global irradiation: application to Romania. Energy, 1993, 24: 883–893.
[55] Page J K. The estimation of monthly mean values of daily total short-wave radiation on vertical and inclined surfaces from sunshine records for latitude 40ºN and 40ºS. Proceedings UN Conference on New Sources of Energy, Rome, Italy, United Nations, 1961, 4: 378-390.
[56] Iqbal M. Correlation of average diffuse and beam radiation with hours of bright sunshine. Solar Energy, 1979, 23(2): 169–73.

[57] Boukelia T E, Mecibah M S, Meriche I E. General models for estimation of the monthly mean daily diffuse solar radiation (Case Study: Algeria). Energy Conversion and Management, 2014, 81: 211-219.
[58] Lewis G. Diffuse irradiance over Zimbabwe. Solar Energy, 1983, 331, 125-128.
[59] Jain P C. A model for diffuse and global irradiation on horizontal surfaces. Solar Energy, 1990, 45: 301-308.
[60] Bashahu M. Statistical comparison of models for estimating the monthly average daily diffuse radiation at a subtropical African site. Solar Energy, 2003, 75: 43-51.
[61] Hove T, Gottsche I. Mapping global and beam solar radiation over Zimbabwe. Renewable Energy, 1999, 18: 535-556.
[62] Lealea T, Tchinda R. Estimation of monthly mean daily diffuse solar radiation in the north and far north of Cameroon. European Science Journal, 2013a, 9 (18): 34-43.
[63] Lealea T, Tchinda R. Estimation of diffuse solar radiation in Area between 5^{o}N and 10^{o}N of Cameroon. Natural Resources, 2013b, 4: 279-285.
[64] Mohammed O W, Yanling G. Estimation of diffuse solar radiation in the region of Northern Sudan. International Energy Journal, 2016, 16: 163-172.
[65] Butt S R, Mansor M, Abuam T. Estimation of global and diffuse solar radiation at Tripoli. Renewable Energy, 1998, 14: 121-127.
[66] Karakoti I, Das P K, Singh S K. Predicting monthly mean daily diffuse radiation for India. Applied Energy, 2012, 91(1): 412–25.
[67] Muneer T, Munawwar S. Improved accuracy models for hourly diffuse solar radiation. J. Sol. Energy Eng., 2006, 128: 104–117.
[68] Mubiru J, Banda E J K B. Performance of empirical correlations for predicting monthly mean daily diffuse radiation values at Kampala, Uganda. Theoretical and Applied Climatology, 2007, 88: 127-131.
[69] Maduekwe A A L, Chendo M A C. Atmospheric Turbidity and the diffuse in glance in Lagos, Nigeria Solar Energy, 1997, 61(4): 241-249.
[70] Mohammadi K, Shamshirband S. Long C W, Arif M, Petkovic D, Ch S. A New hybrid support vector machines-wavelet transform approach for estimation of horizontal global solar radiation. Energy conversion and management, 2015a, 92: 162-171.
[71] Mohammadi K, Shamshirband S, Anisi M H, Alam K A, Petkovic D. Support Vector regression based prediction of global solar radiation on a horizontal surface. Energy conversion and management 2015b, 91: 133-147.
[72] Chen J L, Li G S, Wu S J. Assessing the potential of support vector machines for estimating daily solar radiation using sunshine duration. Energy conversion and management, 2013,73:311-318.
[73] Ramedani Z, Omid M, Keyhani A, Khoshnevisan B, Saboohi H. A. Comparative Study between fuzzy inear regression and support vector regression for global solar radiation prediction in Iran Solar Energy, 2014, 109: 135-143.
[74] Ramedani Z, Omid M, Keyhani A, Shamshirhand S, Khoshnevisan B. Potential of radial basis function based support with regression for global solar radiation prediction. Renewable and Sustainable Energy Review, 2015, 39: 1003-1011.
[75] Landerous G, Lopez J J, O, Kisi O, Shiri J. Comparison of gene expression programming with neuro-suzzy and neural network computing techniques in estimating daily incoming solar radiation in the Basque Country (Northern Spain). Energy Conversion and Management, 2012, 102: 1-13.

[76] Petkovic D, Cojbasic Z, Lukie S. Adaptive neuro-suzzy selection of heat rate variability parameters affected by autonomic nervous system. Expert Syst. App., 2013, 40: 4490-4493.
[77] Petkovic D, Gocic M, Trajkovic S, Shamshirbrand S, Motamedi S, Aaishim R., *et al.* Determination of the most influential weather parameter on reference evaporatranspiration by adoptive; neuro-fuzzy methodology. Comput Electron Agric, 2015, 114: 277-284.
[78] Bosch J L, Lopz G, Battles F J. Daily Solar irradiation estimation over a mountainous area using artificial neutral networks, Renewable Energy, 2008, 33: 1622-1628.
[79] Oliveira A.P. Escobedo J F, Machado A J, Soares J. Correlation models of diffuse solar-radiation applied to the City of Sao Paulo, Brazil. Applied Energy, 2002, 71: 59-73.
[80] Lawrence J. Data preparation for a neural network. Artif Intell Expert, 1991: 34-41.
[81] Shamshirband S, Mohammadi K, Khoronsanizadeh H, Yee P L, Lee M, Petkovic D, Zalnezhad E. Estimating the diffuse solar radiation using a coupled support vector machine-wavelet transform model. Renewable and Sustainable Energy Reviews, 2015, 56: 428-435.

CALL FOR PAPERS

Trends in Renewable Energy

ISSN Print: 2376-2136 ISSN online: 2376-2144

http://futureenergysp.com/index.php/tre/

Trends in Renewable Energy (TRE) is an open accessed, peer-reviewed semi-annual journal publishing reviews and research papers in the field of renewable energy technology and science. The aim of this journal is to provide a communication platform that is run exclusively by scientists. This journal publishes original papers including but not limited to the following fields:

- ✧ Renewable energy technologies
- ✧ Catalysis for energy generation, Green chemistry, Green energy
- ✧ Bioenergy: Biofuel, Biomass, Biorefinery, Bioprocessing, Feedstock utilization, Biological waste treatment,
- ✧ Energy issues: Energy conservation, Energy delivery, Energy resources, Energy storage, Energy transformation, Smart Grid
- ✧ Environmental issues: Environmental impacts, Pollution
- ✧ Bioproducts
- ✧ Policy, etc.

We publish the following article types: peer-reviewed reviews, mini-reviews, technical notes, short-form research papers, and original research papers.

The article processing charge (APC), also known as a publication fee, is fully waived for the Trends in Renewable Energy.

Call for Editorial Board Members

We are seeking scholars active in a field of renewable energy interested in serving as volunteer Editorial Board Members.

Qualifications

Ph.D. degree in related areas, or Master's degree with a minimum of 5 years of experience. All members must have a strong record of publications or other proofs to show activities in the energy related field.

If you are interested in serving on the editorial board, please email CV to editor@futureenergysp.com.